Functional and anatomical properties of visual cortex in individuals with congenital loss of cone photoreceptor function and normally sighted controls

Barbara Molz

Doctor of Philosophy

University of York
Psychology

August 2019

Abstract

The aim of this thesis was to systemically assess reported cortical reorganisation in achromatopsia, a congenital loss of cone photoreceptor function, to inform the current development of vision restoration approaches. Both, functional and structural magnetic resonance imaging (MRI) were used to answer if and to what extend the brain undergoes changes when visual input is lost from birth.

First, visual cortical representations of rod and cone driven signals were examined in normally sighted participants to detail differences between these two retinal pathways. We showed that spatial summation properties of the rod pathway are expressed at a cortical level and highlighted that low light levels mainly affect primary visual cortex, while extra striate areas, likely related to their increased spatial pooling properties, still show robust responses.

Further, functional MRI showed no differences in cortical responses at central visual field representations between achromats and controls, while achromats that presented with reduced rod function are characterised by a more severe reduction in cortical responses. Notably, traces of remapping in form of an eccentricity shift cannot be ruled out for some participants,

Last, this thesis examined brain integrity in achromatopsia using surface-based morphometry and revealed that surface area is reduced across primary visual cortex. Further, patients showed highly localised thickening of the foveal representation in primary visual cortex, supporting the notion of aberrant pruning processes.

In summary, findings presented in this thesis allowed insights into cortical mechanisms that maximise sensitivity when visual information is sparse and clearly showed that remapping is not a general feature in achromatopsia while the absence of visual input has distinct effects on cortical structure, comparable to other patient groups with congenital loss of vision.

Table of contents

List of figures

List of tables

List of equations

Acknowledgements

First of all, I want to express my sincere gratitude to my supervisors, Antony Morland and Heidi Baseler. Throughout the past four years they not only offered excellent scientific guidance, support and encouraging words but they also shaped my scientific thinking, writing skills and so much more and made me without doubt a better scientist.

Another big thank you goes to Alex Wade, for always having an eye on my progress, motivational words and, same as Miles Whittington, really valuable input during my TAP meetings.

Thanks a lot also to André for fixing each of my always 'extremely easy' requests and Becky, the best summer student you could wish for. The Morland lab for laughs, GoT nights, Rook sessions but also the whole YNiC team for catch-ups, advice and the one or the other shared pint.

Another big thank you goes out to the NextGenVis crew. All our workshops felt like meeting good old friends, which made this PhD journey an absolute enjoyable one. Michael Hoffmann, for his thoughtful insights and enthusiasm about our project, Anne, Khazar, Robert and the rest of the Hoffmann lab for loads of nice memories. Netta, Noa and Peter for an unforgettable time in Jerusalem and to Freja and in this respect also the exceptional canteen at Lundbeck. A major thanks also goes to Koen Haak for all his ideas and always finding the time to teach me something new.

I'm also extremely grateful to so many people I met during my time in York, which made this past 4 years even more special: Mark Himmelberg, for solidifying my English and introductions to (his version of) British culture. Alex and Milena, for food sessions, festival bliss, gym visits and just for being you but also to Lucilla, Sara, Mark,

Martin, Ellie, Niamh, the little Bub, Sarah, Lisette, Alex and so many more. Thanks also to all the friends around the world, Ines, the whole Vienna crew, people from back home… You always opened your doors, made time for a catch up, gave me a place to crash, pep talks along the way and made all holidays so much more fun.

Special thanks also to my uncle and my aunt for always believing in me, motivational emails and care packages full of Bavarian treats. Lukas, for occasionally being proud of his older sister. Thanks for the BBQ treats, shared memes, food highlights and taxi services– about time to plan that Black Forest trip.

Last but not least I want to thank my parents who, despite the fact that they still don't really know what I'm actually doing (something with vision and MRI) could not be more proud. Your encouragement and constant support means the world to me.

Declaration

I declare that the work presented in this thesis is original and my own, and was carried out under the supervision of Prof. Antony Morland and Dr. Heidi Baseler. This work has not been submitted to this or any other University for a degree.

A part of the data collection of Chapter 3 was carried out by a Laidlaw scholarship student, Rebecca Lowndes, whom I supervised during my PhD. Data from Chapter 4 and 5 was part of a multicenter study, thus was collected as a multi team effort either by our collaborators at the Otto-van-Guericke University, Magdeburg, Germany (Prof. Michael Hoffmann, Dr. Anne Herbik) or by myself at the York NeuroImaging Centre or during my secondary work placement at the Hadassah Medical Centre, Jerusalem, Israel with the assistance of Prof. Netta Levin, Dr. Noa Raz, and Peter de Best. Moreover, Dr. John Maguire, Prof. Irene Gottlob and Dr. Rebecca McLean facilitated and assisted with the recruitment of patients with achromatopsia.

Data in **Chapter 3** was presented at as a poster at the European Conference on Visual Perception, Berlin, Germany, as:

Molz, B., Gouws, A., Baseler, H., & Morland, A (2017, August). Effects of different luminance levels on population receptive field estimates in primary visual cortex.

Data in **Chapter 3** was presented as a poster at the Organization for Human Brain Mapping Singapore, as:

Molz, B., Lowndes R., Gouws, A., Baseler, H., & Morland, A. (2018, June). Influence of different luminance levels on population receptive field estimates.

Data in **Chapter 3** was presented as a poster by Prof. Antony Morland at the Vision Science Sociecty Meeting, St Pete's Beach, Flordia, USA, as:

Morland, A., Molz, B., Lowndes R., Gouws, A., & Baseler, H. (2018, May). Population receptive fields in V1 enlarge as luminance is reduced from photopic to scotopic levels.

Data in **Chapter 3** was presented as a poster by Rebecca Lowndes at the Applied Vision Association (AVA) December meeting, London, UK, as:

Lowndes, R., Molz, B., Gouws, A., Baseler, H., & Morland, A. (2017, December). Population Receptive Fields in V1 Enlarge as Luminance Falls From Photopic to Scotopic Levels.

Chapter 1

General Introduction

1.1 Overview

Visual disorders that affect both eyes will deprive the brain of distinct sensory input. While vision and the integration of sensory input is increasingly understood, it is still not clear what consequences vision loss has on the brain. The visual parts of the brain might be plastic enough to adapt to the loss of sensory input, especially early in life when circuits are not yet hardwired. However, if eye diseases occur later in life the costs to rearrange a working system might be too high and loss of input could even lead to degeneration of neurons and atrophy in deafferented structures.

An ongoing goal in ophthalmology is to successfully treat vision loss and currently an abundance of vision restoration therapies are being developed and tested. A common feature of all therapies, such as retinal implants or gene therapy is that they target the eye and neglect the possibility that the brain might have adapted to missing input. However, the success of these treatments relies heavily on the assumption or expectation that the brain is still capable of correctly implementing information once vision is restored. It is therefore crucial to characterise how eye disease affects the brain to inform the field of restorative technologies and help to design the best possible therapeutic approaches.

This thesis will investigate this from different angles:

First, this thesis aims to examine how the visual cortical representation of rod-driven signals differs from the representation of cone-driven signals in normally sighted human participants.

Secondly, this thesis will assess changes in primary visual cortex in rod achromats, who have a congenital retinal disorder rendering cones dysfunctional resulting in partial vision loss, comparing newer and older retinotopic mapping methods (population receptive field mapping and phase encoded retinotopy).

Thirdly, this thesis will characterise anatomical properties of primary visual cortex in this patient population using a surface-based approach.

The focus of this chapter is to introduce key concepts that build the backbone of the thesis. Interpreting changes brought about by vision loss requires first a detailed knowledge about the healthy visual system. The first part will therefore focus on the retinotopic organisation of the visual cortex and the concept of visual field maps. Secondly, this chapter will discuss the concept of reorganisation and cortical plasticity in relation to vision loss and give an overview of structural and functional changes reported previously in primary visual cortex as a consequence of vision loss.

1.2 Visual field maps

Visual processing starts at the eye where sensory information is processed by the photoreceptors within the retina. However, the main computation occurs in the brain within the occipital cortex. At the level of the retina visual information is still maintained – in an upside down manner – and conveyed further along the visual pathway. At the optic chiasm visual information is segregated according to visual hemifield and reaches the primary visual cortex, commonly referred to as V1, via the

lateral geniculate nucleus (LGN). In the occipital cortex visual field information is processed on the contralateral side, thus, the left hemisphere processes information from the right visual field and vice versa. To process detailed visual signals, information is organised in distinct cortical maps, which facilitate the integration of the complex information (Andrews, Halpern, & Purves, 1997; Solomon & Lennie, 2007).

By studying the effects of gunshot lesions Holmes was among the first to identify and describe such visual field maps in humans (Holmes, 1918). His findings and following lesion studies (Horton & Hoyt, 1991; Teuber, Battersby, & Bender, 1960; Wong & Sharpe, 1999) were later validated by invasive electrophysiological recordings in animals, which allowed a greater insight into the organisation and function of these maps on a cellular level (Felleman & Van Essen, 1991; David H. Hubel & Wiesel, 1965; Lima et al., 2005; Tusa, Palmer, & Rosenquist, 1978; Van Essen & Maunsell, 1983; Zeki, 1969).

The architectural advantage of visual field maps is their retinotopic organisation, meaning that the spatial structure of the computed visual information is preserved in these maps (Engel, Glover, & Wandell, 1997; Horton & Hoyt, 1991).

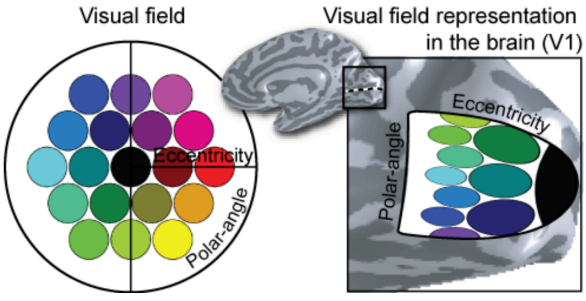

Figure 1.1 Schematic of the visual field representation in primary visual cortex. The left visual field is represented in V1 on the contralateral, right hemisphere. In general, the spatial organisation of the visual field is still maintained within the brain, with an enlarged representation of the central parts of the visual field (Dumoulin, 2015);

However, this mapping procedure does not follow a linear approach. As the central part of the retina contains a higher cell density, it produces a larger number of projections to visual cortex, resulting in cortical magnification of the central retina (Figure 1.1). Thus, in V1, the representation of the central visual field is greater in area than the representation of the peripheral visual field (Morland, 2015; Wandell & Winawer, 2011; Wässle, Grünert, Röhrenbeck, & Boycott, 1990).

Areas adjacent to V1, important for higher visual processing, also follow the same retinotopic representation (Wandell, Brewer, & Dougherty, 2005; Wandell & Winawer, 2011).

Over the past few decades advances in magnetic resonance imaging (MRI), but especially in functional MRI (fMRI) made it possible to effectively characterise human visual field maps and underlying neuronal properties in a non-invasive manner (Engel et al., 1997; Tootell, Dale, Sereno, & Malach, 1996; Wandell, Dumoulin, & Brewer, 2007; Zeki et al., 1991).

FMRI only allows an indirect measure of neural activity. The underlying concept is a difference in blood-oxygenation levels in active and inactive areas of the brain. These changes in the blood-oxygenation-dependent signal (BOLD) affect the local magnetic field, hence allowing an estimation of active regions within the brain. While this method is only indirect, the spatio-temporal resolution is still sufficient to reliably trace activity within an area of a few millimetres but also time wise within a few seconds. The BOLD signal is measured in volumetric pixels, so-called 'voxels', and a standard voxel size used for anatomical scans ($1x1x1mm^3$) will encode the information of around 1 million neurons (Brewer & Barton, 2014; Heeger & Ress, 2002; Logothetis & Wandell, 2004).

An important concept of sensory neurons is the term receptive field (RF), meaning the space or area this cell is responsive to. While first described for somatosensory neurons by Sherrington (1906), Hartline (1938) was the first to apply this term to vision and described the receptive field of optic nerve fibres in the frog retina. Here, the receptive field relates to the location within the visual field the respective cells will respond to. Population receptive fields (pRF), first shown by invasive electrophysiological recordings in animals (Jancke, Erlhagen, Schöner, & Dinse, 2004; Victor, Purpura, Katz, & Mao, 1994), expand the concept of the RF to an aggregation or population of neurons. As a result of the underlying topographic organisation the pRF will share similar features, such as the tuning to a given location in the visual field.

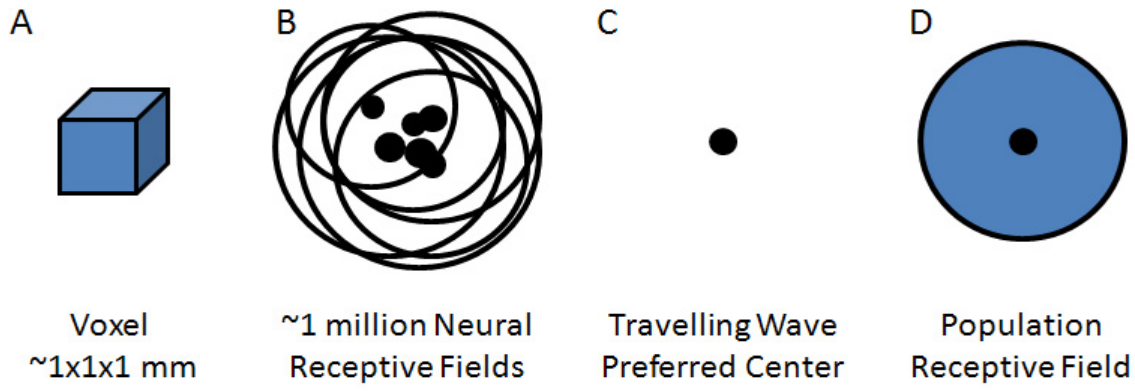

Figure 1.2 Underlying concept of two analysis streams. A standard voxel (A) contains around one million neurons that have approximately the same receptive field characteristics (B). Traveling wave retinotopy (TWR) uses the retinotopic architecture of the visual cortex to estimate the location (preferred centre) within the visual field this voxel is maximally tuned to (C) while population receptive field mapping can estimate additionally receptive field properties, like the pRF size (D) (Barton & Brewer, 2012);

The concept of receptive fields can be translated and applied to fMRI measurements to visualise visual field maps. Accordingly, neurons measured within one voxel should all encompass on average similar receptive fields. Conventional visual field mapping

methods, such as phase-encoded retinotopy (Brewer & Barton, 2012; Engel et al., 1994; Sereno et al., 1995; Wandell et al., 2005), estimate the response to periodic stimuli averaging the receptive fields of the underlying neurons to determine the visual field location which elicits the maximal response for each voxel (Figure 1.2). This information is sufficient to delineate visual field maps, but does not reveal any additional RF properties of neurons within a certain voxels. While further studies have attempted to uncover more RF properties using conventional neuroimaging methods (Larsson & Heeger, 2006; X. Li, Dumoulin, Mansouri, & Hess, 2007; A. T. Smith, 2001; Tootell et al., 1997) the application of a model-based approach, referred to as population receptive field mapping, has allowed estimates of further RF parameters such as pRF size (Figure 1.2D) (Alvarez, de Haas, Clark, Rees, & Schwarzkopf, 2015; Dumoulin & Wandell, 2008) Both visual field mapping methods are described in more detail in the following methods chapter (2.4).

Already at the level of the retina, there is a distinct relationship between eccentricity and the size of the underlying pRF, which are smaller for neurons in the centre of the retina and increase in the periphery (Nickells, 2012). This concept has been observed within the visual cortex in invasive animal studies (Van Essen, Newsome, & Maunsell, 1984) and confirmed using fMRI in humans (Dumoulin & Wandell, 2008; A. T. Smith, 2001). The application of pRF mapping has shown that pRF size scales with eccentricity and visual hierarchy in several independent studies (Figure 1.3) (Kay, Winawer, Mezer, & Wandell, 2013; Wandell & Winawer, 2015).

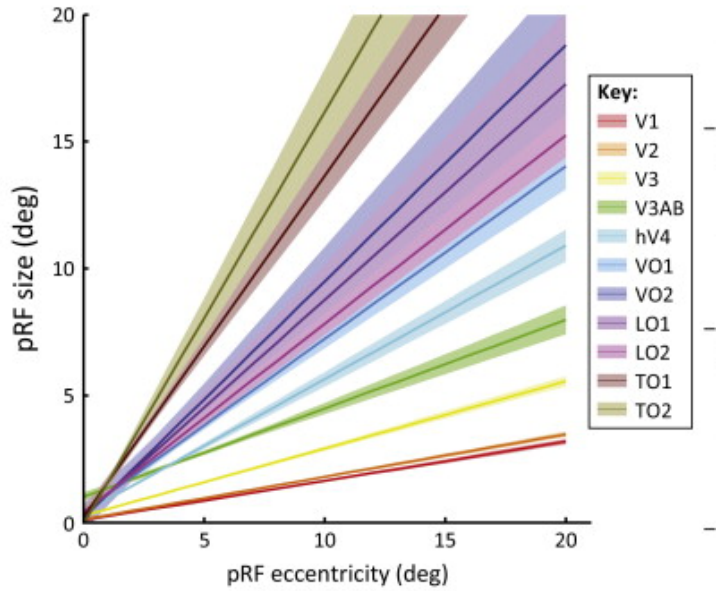

Figure 1.3 Population receptive field (pRF) properties in human visual cortex; pRF size is plotted as a function of eccentricity for different visual areas (Kay et al., 2013; Wandell & Winawer, 2015).

1.3 Consequences of visual loss

The use of MRI to reveal anatomical but also functional properties of the human visual cortex and the underlying RFs has had an immense impact on neuroscience, and has facilitated the understanding of how sensory information is processed within the brain. In addition, these methods have also been used in clinical populations to assess the consequences of visual disorders on the visual cortex (Brown, Woodall, Kitching, Baseler, & Morland, 2016; Hickman & Morland, 2011; Morland, Baseler, Hoffmann, Sharpe, & Wandell, 2001; Wandell & Smirnakis, 2009). Defects that lead to lesions of the retina will cause blind spots at discrete parts of the visual field. If both eyes are affected, information from this part of the visual field will no longer reach the visual cortex, and the corresponding cortical representation will be deprived of any input. The deafferented area is most commonly referred to as the 'lesion projection zone' (LPZ). When components within the visual system are damaged,

neurons may change their response patterns resulting in abnormal visual field maps, or they may degenerate leading to atrophy and subsequent structural changes. To date, there is no clear consensus regarding the consequences that arise from visual deprivation on brain structure and function; possibilities range from reorganisation and compensatory plasticity to degeneration of the unused structures (Boucard et al., 2009; Brown et al., 2016; Morland et al., 2001; Smirnakis et al., 2005; Stone, Barlow, Milam, Juan, & Milam, 1992).

1.3.1 Defining reorganisation

It is a given that we expect abnormal cortical responses in patients with vision loss. However, abnormal responses do not always imply reorganisation and might not lead immediately to remapping of the visual cortex. One of the key factors to interpret findings is to establish a clear definition of features and changes in cortical signalling we expect to see in reorganisation and how the terms remapping or reorganisation are used. Cortical plasticity is an ongoing process throughout life, involving functional and structural changes. Looking at reorganisation from a theoretical standpoint there are distinct mechanistic differences between normal learning and subsequent plastic changes and changes as part of recovery later in life (Morland, 2015; Wandell & Smirnakis, 2009). One form of plasticity refers to changes in the underlying structure and only emerges over a prolonged period of time. Structural plasticity leads to permanent changes of anatomical properties, where new neuronal connections are established, e.g. due to axonal growth (Brewer & Barton, 2014; Wandell & Smirnakis, 2009). This form of plasticity is different from functional reorganisation. Here, rather than establishing new connections, the existing connections are reweighted, e.g. by

changing the strength of synaptic connections or unmasking already present signals. Compared to structural reorganisation, these changes can emerge within days and are not permanent (Brewer & Barton, 2014; Liu et al., 2010; Wandell & Smirnakis, 2009).

1.3.2 Cortical changes as a consequence of vision loss

1.3.2.1 Structural changes

One approach to determine the effect of vision loss on the visual parts of the brain is to look at changes of the underlying structures. Two main analysis streams are currently applied to investigate anatomical alterations in the visual cortex in more detail. Voxel based morphometry (VBM) allows one to compare the grey/white matter volume on a voxel by voxel basis (Ashburner & Friston, 2000; Wright et al., 1995). Surface-based morphometry (SBM) can give more insight into the contributing factors as it can estimate differences in cortical thickness, surface area and gyrification, but is limited to grey matter only (Prins, Plank, et al., 2016). In highly convoluted cortical areas VBM might have less specificity, but seems in general more sensitive to volumetric changes (Park et al., 2009; Plank et al., 2011; Prins, Jansonius, & Cornelissen, 2017). Several studies have started to apply both approaches to characterise observed changes in more detail and add more specificity (Park et al., 2009; Prins, Plank, et al., 2016). There seems to be a general consistency across several studies that visual impairments give rise to changes within the retinotopic cortical structure, e.g. central retinal lesions lead to structural changes in primary visual cortex involved with processing the central parts of the visual field (Boucard et al., 2009; Burge et al., 2016; Plank et al., 2011; Prins, Plank, et al., 2016). In congenital or early blind individuals, studies generally have shown increased cortical thickness

(Bridge, Cowey, Ragge, & Watkins, 2009; J. Jiang et al., 2009; Park et al., 2009; Qin, Liu, Jiang, & Yu, 2013; Voss & Zatorre, 2012) while some have highlighted a reduction in grey matter or surface area in primary visual cortex (Bridge et al., 2009; Park et al., 2009). In late blind individuals, the findings point towards cortical degeneration as grey matter volume and surface area in primary visual cortex are generally reduced compared to controls (Boucard et al., 2009; Hernowo et al., 2014; Plank et al., 2011). For cortical thickness the findings are less clear and show only a tendency towards cortical thinning, but the extent of thinning differed between studies (Burge et al., 2016; J. Jiang et al., 2009; Prins, Plank, et al., 2016). The increase in cortical thickness in congenitally blind individuals could be interpreted as structural plasticity but this finding is in contrast to the general reduction in overall grey matter volume (Hasson, Andric, Atilgan, & Collignon, 2016; J. Jiang et al., 2009). Structural changes in late blind individuals are less likely linked to reorganisation and the thinning of primary visual cortex and general reduction in volume are more likely caused by the absence of visual input (Boucard et al., 2009; Hernowo et al., 2014; Prins, Plank, et al., 2016). Interestingly, one study reported an increase in cortical thickness in the peripheral proportions of V1 in the late blind. This finding was attributed to compensatory plasticity due to the increased use of peripheral areas in central vision loss (Burge et al., 2016). While findings seem broadly consistent, the subtle differences between studies highlight that the interpretation is not always clear. Confounding factors, like the onset age of the disease but also more general factors such as changes expected from normal aging have to be taken into account when interpreting results as reorganisation or atrophy.

1.3.2.2 Functional changes

In acquired vision loss that occurs later in life, several, sometimes controversial, claims have been made and there is no clear answer if and to what extent the cortex is able to change and adapt its function and under which circumstances plasticity occurs (Morland, 2015; Wandell & Smirnakis, 2009). While some studies have suggested that cortical remapping takes place (Baker, Dilks, Peli, & Kanwisher, 2008; Baker et al., 2005; Schumacher et al., 2008), these findings have later been questioned (Baseler et al., 2011; Masuda et al., 2010). A potential argument against cortical remapping in acquired vision loss concerns the so-called 'coding catastrophe'. If, in an already established system, early stages of the visual pathway reorganise in response to input, this would have a distinct and not necessarily positive impact on the encoding properties further downstream and the cost and consequences might outweigh the benefits (Dhruv & Carandini, 2014; Haak, Fast, Bao, Lee, & Engel, 2014; Haak, Morland, & Engel, 2015; Patterson, Wissig, & Kohn, 2014; Schwartz, Hsu, & Dayan, 2007; Seriès, Stocker, & Simoncelli, 2009).

In contrast, a large body of research suggests that sensory systems in the brain are more likely to show evidence of plasticity when sensory deficits are present very early in development (Kupers & Ptito, 2011; Lazzouni & Lepore, 2014; Voss & Zatorre, 2012). This would allow subsequent pathways to accommodate early sensory input changes, avoiding the coding catastrophe.

For example, congenital abnormalities that affect the visual pathway, as in albinism or achiasma lead to the misrouting of visual information from the eye to the brain. As a result, it was found that visual field maps representing both hemifields are superimposed or interdigitated in primary visual cortex. However, as they still share comparable features with normal visual field maps, these findings were interpreted

as a lack of cortical reorganisation. It was suggested, though, that potential reorganisation might have occurred on a synaptic level to accommodate the input of confounding information from opposite hemifields (Ahmadi et al., 2019; Hoffmann & Dumoulin, 2015; Hoffmann et al., 2012; Hoffmann, Tolhurst, Moore, & Morland, 2003; Morland et al., 2001; Morland, Hoffmann, Neveu, & Holder, 2002).

A study by Baseler et al. (2002) used functional MRI to investigate vision in achromats, a rare patient cohort that congenitally lacks cone function or cones in general. In typically developing, control participants a large region representing the central visual field within primary visual cortex responds to signals elicited by the all-cone fovea, and this region is inactive under scotopic, rod-only viewing conditions due absence of rod photoreceptors within the central fovea. Baseler et al. (2002) showed that in achromats this foveal representation is highly responsive to rod-only signals, providing compelling evidence of large-scale cortical remapping (Figure 1.4).

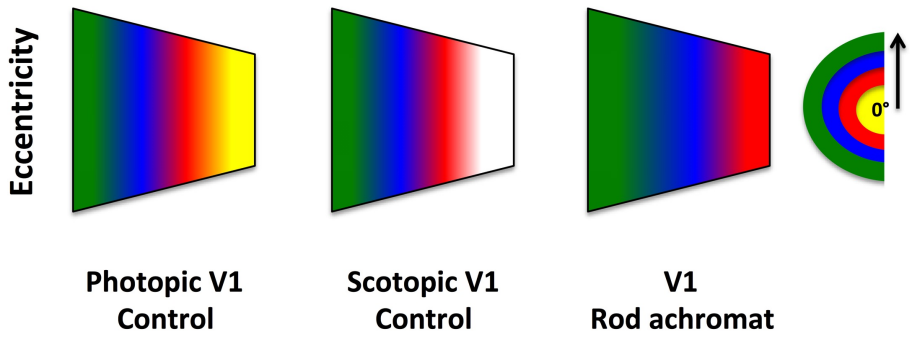

Figure 1.4 Schematic representation of visual field eccentricity maps from a control and achromat. Visual cortical activity elicited by cone photoreceptors, depicted in yellow, is clearly present under photopic conditions at a location that represents the centre of the visual field. This area is inactive under scotopic conditions, caused by the absent cone input. In rod achromats the representation of the central visual field has reorganised and is activated by rod only signals (adapted from Barton & Brewer, 2014).

1.4 Implications for gene therapy

It is well established that the brain is most plastic during the early years of development. Critical periods shape our brain and how it is wired during a state of maximum flexibility in order to incorporate and adjust to our behaviour, which is commonly referred to as 'experience-dependent plasticity'. The visual system also has distinct critical periods where specific features of visual processing are established and later hardwired (Hensch, 2005; David H. Hubel & Wiesel, 1970; David H. Hubel, Wiesel, & LeVay, 1977; Takesian & Hensch, 2013). It naturally follows that timing is a crucial component of reorganisation, and the brain's ability to reorganise is inversely correlated with the age of onset of the visual defect (Kennard & Fulton JF, 1942; Teuber, 2008). Thus, there seems to be a clear distinction between congenital and acquired vision loss as visual function seems to be less affected in children with cortical lesions compared to adults with corresponding defects (Amicuzi et al., 2006; Giaschi et al., 2003; Guzzetta, Cioni, Cowan, & Mercuri, 2001; Guzzetta et al., 2010; Payne & Lomber, 2002; Werth, 2008)

Interestingly, numerous studies have also reported extensive cross modal plasticity in individuals with congenital disorders or visual defects early in life (Liu et al., 2010; Merabet et al., 2009; Sadato, Okada, Honda, & Yonekura, 2002; Sadato et al., 1996). Here, the deafferented areas are recruited by other sensory modalities and will react for example to tactile information, as elicited by Braille reading (Sadato et al., 1996)

When considering current vision restoration approaches, the brain's ability to reorganise following vision loss might diminish the success of interventions. Several case studies in individuals with congenital or early-onset vision loss have already reported poor results following vision restoration treatments (Gregory & Wallace,

1963; Stern, von Senden, & Heath, 2006; Valvo, 2014). A detailed case study by Fine et al. (2003) investigated an individual, MM, who lost vision at an early age due to a chemical accident damaging the corneas, which were repaired, restoring visual input 40 years later. While certain features could be restored, higher order visual functions were impaired even two years after the restorative surgery (Fine et al., 2003; Huber et al., 2015; Levin, Dumoulin, Winawer, Dougherty, & Wandell, 2010), emphasising that disruption of normal experience dependent development counteracts vision restorative approaches.

In contrast, the reduced reorganisation capability of the visual cortex later in life should have a beneficial impact on vision restoration interventions in acquired vision loss (Legge & Chung, 2016). As a consequence, clinicians need to consider the possible effects of cortical plasticity, especially in the treatment of congenital visual disorders. Studies in representative cohorts that systematically estimate the effects of vision loss on both structural and functional properties are necessary to determine the extent of reorganisation in in order to inform current clinical efforts.

Another important step is to develop well-designed control conditions in participants without visual loss to assess whether differences in visual field representations in patients are indeed caused by remapping of cortical structures. This is crucial, as per definition it cannot be considered reorganisation as long as visual cortical maps in the presence of vision loss are still comparable to normal visual field maps. Several studies have attempted to mimic the central lesion in patients using an 'artificial scotoma' by presenting a partially masked stimulus in control participants (Baseler et al., 2011; Binda, Thomas, Boynton, & Fine, 2013; Haak, Cornelissen, & Morland, 2012; Papanikolaou, Keliris, Lee, Logothetis, & Smirnakis, 2015). In two other studies, control participants were tested under low light levels, where only rod

photoreceptors are active, simulating the rod-free central scotoma present in achromatopsia (Barton & Brewer, 2015; Baseler et al., 2002). All these studies indicated changes in pRF properties around or at the border of the simulated LPZ, highlighting that differences in pRF properties are not generally a distinct characteristic of reorganisation (Haak et al., 2012; Morland, 2015; Smirnakis, 2016; Wandell & Smirnakis, 2009). This highlights the importance of considering the effect of partial stimulation on visual cortical estimates in healthy participants in order to determine whether or not reorganisation has occurred in a certain patient population.

1.5 Thesis overview

In summary, several factors seem to influence plasticity and the age of onset of vision loss seems to play a critical role and impact the likelihood of reorganisation. A visual defect that is present at birth is likely to have a different impact on cortical structures than when vision is lost in adulthood. In an adult, the visual processing stream is already hard wired and the cost for any changes, especially at early stages of visual processing, might be too high (Ahissar & Hochstein, 2004; Haak et al., 2015; Morland, 2015; Werniuk, 1997). Baseler et al. (2002) showed convincing evidence of reorganisation in a small patient cohort with congenital cone photoreceptor loss (achromats). Vision restoration in the form of gene therapy was successfully tested in animals with the same congenital disorder (Banin et al., 2015; Hassall, Barnard, & MacLaren, 2017; Komáromy et al., 2010; Michalakis, Schön, Becirovic, & Biel, 2017; Pang et al., 2010) and several human trials are ongoing (NCT03758404, NCT03001310, NCT03278873, NCT02935517, NCT02599922, NCT02610582).

Achromatopsia is a rare congenital condition and findings in Baseler et al (2002) are based on only three, high functioning participants, who may not be representative of the patient population as a whole. As the ability of the brain to reorganise may diminish the success of gene therapy it is crucial to determine if the reorganisation described by Baseler et al. (2002) is indeed generalizable to the achromat population to inform current vision restoration approaches.

Thus, the main aim of this thesis is to characterise the properties of rod-driven signals in a representative, larger cohort of patients and assess both, functional and structural properties of primary visual cortex compared to healthy control individuals. This is done in three empirical chapters, which aim to systematically answer the question if and to what extent the brain undergoes changes when visual input is lost from birth.

An advantage of studying reorganisation in achromats is the ability to compare findings to an innate and reversible appropriate control condition. Thus, **Chapter 3** examines how the visual cortical representation of rod-driven signals differs from the representation of cone-driven signals in normally sighted human participants. Results found here will not only detail the differences in cortical representation of rod compared to cone input but will also establish important baseline measurements for characterising changes in achromats.

The following empirical chapters make use of a data set collected as part of a multi-centre collaboration that enabled us to recruit the largest cohort of achromats to date. In **Chapter 4** we build on Baseler's study and employ population receptive field mapping to derive and characterise visual field maps in both controls and patients under different luminance levels. In **Chapter 5** we examine if this condition also leads to structural changes in primary visual cortex using a surfaced-based approach.

Anatomical brain properties have not been investigated previously in this patient population and will provide another approach to assess whether primary visual cortex indeed reorganises when the brain is deprived of select input from birth. **Chapter 6** discusses the findings of each empirical chapter and functions as a general conclusion, summarising possible implications for vision restoration approaches and providing directions for further studies.

Chapter 2

General methods

Several MRI and fMRI analysis streams are shared across subsequent empirical chapters. This chapter will therefore summarise common analysis streams to provide a more in-depth framework and avoid unnecessary repetition.

This chapter will describe in more detail the data acquisition protocols (scanner settings, stimulus details, experimental procedure) for all data collected at the York Neuroimaging Centre. These parameters are consistent and identical across all chapters. This chapter will further go into data pre-processing routines and outline the two main analysis methods that are commonly used throughout the thesis: phase-encoded retinotopy and population receptive field mapping.

As this thesis also includes data collected at other imaging centres with different data acquisition parameters, these details as well as chapter-specific methods will be described in the methods section of the respective empirical chapters.

2.1 Data acquisition

2.1.1 Imaging parameters

All scans were acquired using a SIEMENS 3T MAGNETOM Prisma scanner. For high-resolution anatomical images, one T1-weighted scan (TR, 2500ms; TE, 2.26ms; TI, 900 ms; voxel size, 1×1×1mm^3; flip angle, 7°; matrix size, 256×256×176) was acquired using a 64-channel head coil. For all functional scan sessions only the posterior part of the coil (32 channels) was used, covering the region of the occipital cortex. The functional runs were made up of four 7-minute pRF stimulus

presentations interleaved with two 5.5-minute phase encoded ring stimulus presentations using a standard EPI sequence (TR, 1500ms; TE, 23ms; voxel size, 2.5×2.5×2.5mm^3; flip angle, 80°; matrix size, 64×64×30). The axial slices were aligned with the calcarine sulcus and placed to cover the whole occipital cortex, with approximately two slices of ventral leverage space.

For each fMRI session a proton density (PD) scan with the same spatial prescription but a better resolution (TR, 2700ms; TE, 42ms; voxel size, 0.4×0.4×2.5mm^3; flip angle, 160°; matrix size, 384×384×30) as the functional data was acquired to facilitate alignment of functional scans to the high-resolution structural scan.

2.1.2 Stimulus parameters

2.1.2.1 Stimulus display

Stimuli were generated using the Psychophysics Toolbox Version 3 (Brainard, 1997; Kleiner et al., 2007; Pelli, 1997) in conjunction with 32-Bit MATLAB (Version 7.6.0; The MathWorks Inc., Natick, MA, 2008). Stimuli were rear-projected onto an acrylic screen situated in the bore of the scanner behind the participant's head using an LCD projector (PROPixx DLP LED Projector (VPixx Technologies)). The stimulus display set up has been calibrated and tested to assure linear operation of the stimulus display. All subjects viewed the screen via a mirror mounted on the head coil at a viewing distance of 57cm.

2.1.2.2 pRF and phase-encoded stimuli

For pRF mapping we presented a modified version of the bar stimuli as generally described previously (Dumoulin & Wandell, 2008). Briefly, a bar shaped (width 2°), unmasked portion of a 100% contrast flickering checkerboard stimuli was swept on a

mean grey background in one of eight different directions within a circular aperture (8° radius) with each sweep lasting a total of 48 seconds. In the contrast condition, the checkerboard carrier of the bar stimuli was changed to either 30% or 10% contrast (Figure 2.1).

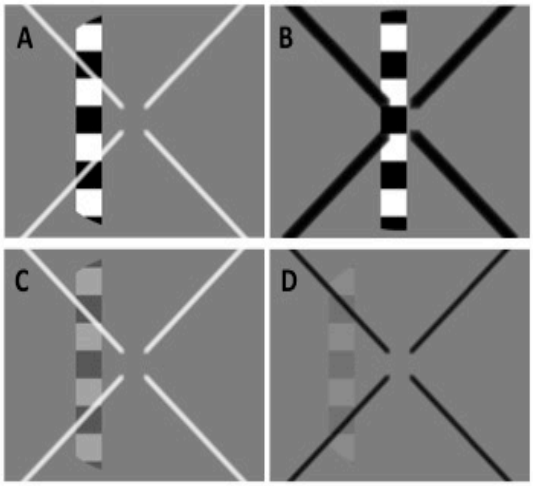

Figure 2.1 Example of the stimuli used for population receptive field mapping. A represents the general stimulus features; the fixation cross is overlaid and includes a central scotoma. In B the fixation cross has the target size for the attention task (doubled width). Stimuli examples seen in B and C were used for the contrast fMRI sessions. In C) the carrier of the stimulus was changed to 30% contrast and in D) to 10%.

Four blank mean luminance periods (12 sec each) were included as baseline conditions at the end of sweeps 1, 3, 5 and 7.

For the phase-encoded retinotopy runs we presented a modified version of the conventional ring stimulus (Engel et al., 1997, 1994; Wandell et al., 2007). The stimulus consisted of one 100% contrast checkerboard (width 2°).

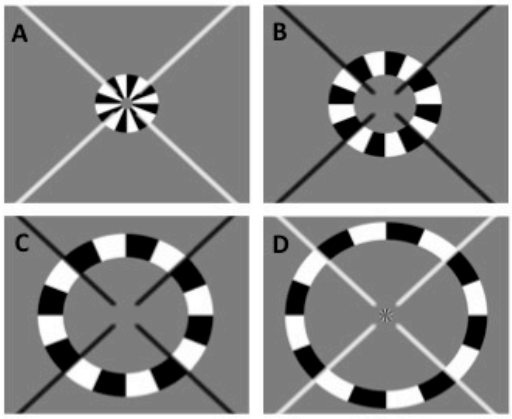

Figure 2.2 Example of the ring stimuli used for the phase encoded fRMI runs. The images A) – D) are some example steps of the one stimulus cycle. Note that in D the stimulus is starting again in the centre of the visual field, while the cycle before is still in its final steps, which is commonly referred to as 'wrap around'.

This ring stimulus increased from the centre of the visual field to a maximum of eight degrees radius and was replaced by a new central annulus, during the last step of each cycle. Each stimulus run lasted 48 seconds and was repeated for 7 full cycles (Figure 2.2).

Spatial (fundamental = 0.25 cycle/deg) and temporal frequency (2Hz square wave contrast reversal) were adjusted for both ring and bar stimuli to maximise responses during scotopic conditions. Subjects maintained central fixation on a large X that extended the diagonal width of the screen and alternated every two seconds between black and white to minimise a potential Troxler effect (Clarke, 1960). To avoid any interference with the central visual field regions, the fixation cross included a central scotoma of 2° diameter. Subjects completed an attention task and were instructed to respond with a button press every time the fixation cross doubled in width. Changes in width occurred randomly no more than once within 12 seconds but at least every 36 seconds. Reaction time and percentage correct of the attention task were recorded for each functional run (Figure 2.1B).

2.1.3 Experimental parameters

2.1.3.1 Viewing conditions

In general, four different viewing conditions were used: High photopic, further referred to as C2 (max. luminance: 600 cd/m^2), represented the standard scanning conditions routinely used at the imaging facility. For low photopic conditions, C1 (max luminance: 20 cd/m^2) a neutral density filter (Formatt Hitech, Firecrest ND 85x85mm, ND1.5) was mounted in front of the projector to reduce the overall luminance. For both scotopic conditions (R2: maximum luminance = 0.01 photopic cd/m^2; R1: max luminance = photopic 0.002 cd/m^2) participants wore customised goggles fitted with layers of neutral density foils (Stage Depot Limited, Neutral Density Rosco E-Colour+ lighting filter sheet) to achieve the specified luminance. All luminance levels were measured and subsequently tested with a Minolta Luminance Meter (LS-100/LS 110) to assure the right luminance levels were reached with the respective equipment. During all scanning conditions all light sources in the scanner room were switched off. For all scotopic scans subjects were dark-adapted for a minimum of 30 minutes before data were acquired. Both additional contrast scan sessions were acquired under bright light, standard scan conditions (C2, max. luminance 600cd/m^2). For all scans participants viewed the presented stimuli monocularly, where a patch covered the non-dominant eye. All control participants were scanned in separate session under all four luminance conditions, while patients were generally scanned under two conditions, C2 and R1 respectively, except where noted otherwise (see Chapter 4, Table 4.2).

2.2 Data Preprocessing

2.2.1 Anatomical data

The high-resolution T1-weighted image was automatically segmented into grey and white matter using the 'autorecon' script implemented in the FreeSurfer 5.3 analysis suite ((Dale, Fischl, & Sereno, 1999; Bruce Fischl, Sereno, & Dale, 1999), http://surfer.nmr.mgh.harvard.edu/). The output was checked for segmentation errors within the occipital lobe and any errors were manually edited using ITK-SNAP ((Yushkevich et al., 2006), www.itksnap.org). Using the 'mrMesh' function of the mrVista tool box, the cortical surface was reconstructed for each subject and rendered in three dimensions to create an inflated cortical surface (Wandell, Chial, & Backus, 2000). Derived visual field maps were overlaid on this surface for visualisation and ROI definition.

For each subject we estimated the bias field of the acquired axial PD scan and corrected any inhomogeneity caused by only using the posterior portion of the surface head coil, by using FMRIB's automated segmentation tool (FAST, (Zhang, Brady, & Smith, 2001). To further assist the final alignment and bring the corrected axial PD scan in the same format as the high resolution T1 scan, we skull stripped the axial PD scan using FMRIBS's brain extraction tool (BET, (S. M. Smith, 2002).

2.2.2 Functional data

Functional data were pre-processed and analysed using modules of the mrVISTA toolbox (VISTASOFT package, VistaLab, Stanford University, http://white.stanford.edu/software) run on the software package Matlab (The MathWorks, Inc., MA, USA; Version 2012a/b) and FSL

(http://www.frmib.ox.ac.uk/fsl). For all functional scans the first eight volumes (12 seconds) were discarded to ensure the scanner reached stable magnetisation. Images were motion corrected between and within scans using a mutual information motion correction algorithm implemented in the mrVista toolbox (Nestares & Heeger, 2000). Scans with large motion artefacts or low participant performance in the attention task were removed (cut off: 75% correct), and the remaining pRF or phase-encoded runs were averaged. The averaged functional scan was subsequently co-registered to the subject specific PD scan using FMRIB's Linear Image Registration TOOL (FLIRT; Jenkinson et al. 2001) which was then aligned to the high-resolution anatomical volume using the rxAlign function implemented in the mrVista toolbox (Nestares & Heeger, 2000).

2.3 Retinotopic mapping

2.3.1 Phase encoded analysis

The retinotopic organisation of visual cortex and the fact that neurons within a voxel will have similar receptive field centres can be used to identify visual areas. Several mapping procedures have been developed that utilise this distinct spatial organisation in the visual cortex.

In traveling wave analysis (also known as 'phase-encoded mapping'), two stimuli are used to identify the two topographical dimensions within the visual cortex: Polar angle is mapped out with a rotating wedge while eccentricity (distance from the fovea/centre of view) is mapped with an expanding / contracting ring stimulus (Figure 2.3). Due to retinotopic organisation, each voxel has a 'preferred centre' and

is tuned to a distinct visual field location (x,y) that will elicit the maximum response when the stimulus transverses the receptive field of these neurons.

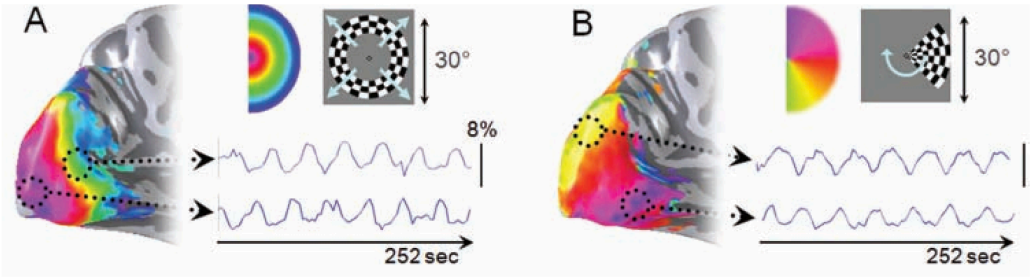

Figure 2.3 Traveling wave analysis. Images show the eccentricity (A) and polar angle map (B) on an inflated and reconstructed surface mesh, estimated using the respective stimuli (expanding ring/rotating wedge). Two regions of interest are highlighted on each representation that depict different eccentricity (A) or polar angle (B) locations. The fMRI time series of each region of interest is denoted. While the frequency of the wave forms is identical and represents the number of stimulus cycles, the phase of the time series differs corresponding to the visual field location the region of interest represents (McKeefry, Gouws, Burton, & Morland, 2009).

When the stimuli expand / rotate periodically across the visual field, different voxels will be activated as they are tuned to different visual field locations. This creates a 'travelling wave' of activation leading to the name 'traveling wave analysis'. A sinusoid can be fitted to this response (using Fourier Transform), where the stimulus cycle rate determines the frequency of the sinusoid. Thus, the polar angle or eccentricity of the respective neurons can be determined by the phase of the sinusoid (Brewer & Barton, 2012; Engel et al., 1994; Sereno et al., 1995; Wandell et al., 2005).

In this thesis, averaged functional data derived from the ring stimuli were analysed using standard phase encoded retinotopy techniques in line with previous publications (Engel et al., 1997, 1994; Wandell et al., 2007). The analysis steps were performed utilising the mrVista toolbox (computeCoranal, VISTASOFT package). The time series of the averaged scans were Fourier transformed to determine the phase and amplitude (% signal change) at the stimulus alternation rate of 1/48Hz. The

phase at which each voxel responded was used to derive the eccentricity value the respective voxel is tuned to.

2.3.2 Population receptive field analysis

A more recent technique developed by Dumoulin & Wandell (2008) expands upon the traveling wave method. While traveling wave analysis just defines the preferred centre of a voxel (x^0,y^0), pRF mapping also estimates the spread (sigma, size) of the receptive field a voxel is tuned to. These three parameters can be estimated using a single, two-dimensional Gaussian. The model uses a two-stage, coarse-to fine approach to minimise the residual sum of squares between the model and the actually measured time series. Specifically, the model multiplies a large database of possible 2D Gaussian pRF parameters with the stimulus aperture to create an activation profile which is subsequently convolved with the haemodynamic response function (HRF), resulting in a set of predicted fMRI time series (Figure 2.4).

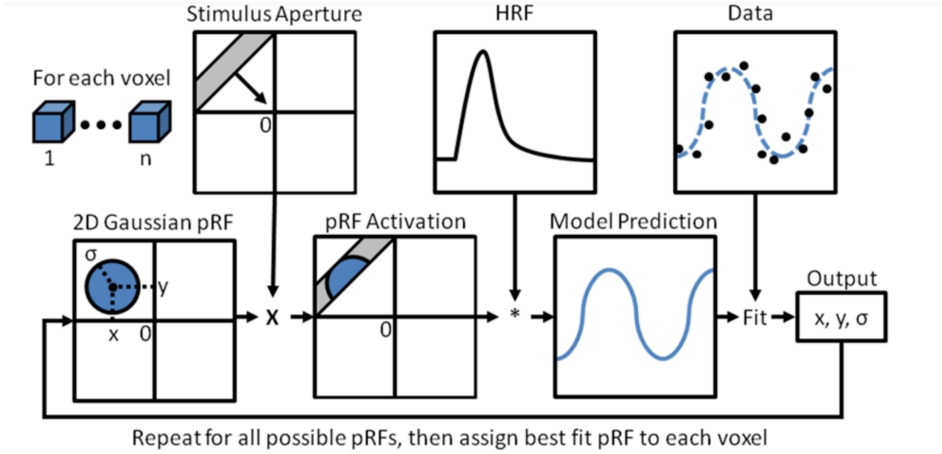

Figure 2.4 Population receptive field modelling. This flow chart describes the steps involved to find the best fitting pRF parameters x, y and sigma that are assigned to each voxel and describe visual field location and spread the underlying neurons are tuned to (Brewer & Barton, 2012; Dumoulin & Wandell, 2008).

After the first, coarse stage, where the data are smoothed, only voxels are retained that explained a certain amount of variance within the time series. These voxels are

then refit to find the 2D Gaussian parameters that best explain the observed fMRI time course. The output of the model are the three parameters defining the 2D Gaussian (x,y and sigma) which are used to define the visual field tuning for each voxel. Although this method would allow the use of any kind of stimulus that traverses through the whole visual field, the most commonly used stimulus for population receptive field mapping is a high contrast flickering bar stimulus that evenly steps across the visual field in all cardinal and intercardinal directions, interleaved with mean luminance blank periods (Figure 2.5, (Brewer & Barton, 2012; Dumoulin & Wandell, 2008).

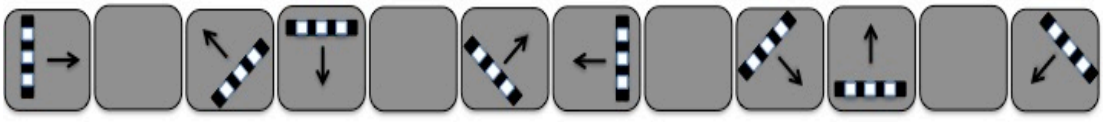

Figure 2.5 Schematic of pRF stimulus movement of a standard pRF scan. Arrows indicate the stepping direction but are not included in the actual stimulus presentation. Grey backgrounds without an overlaid bar stimulus represent the mean luminance baseline blocks.

The estimates derived from pRF mapping are in line with phase-encoded retinotopic mapping, and derived human pRF size estimates are in line with electrophysiological findings in primates (Brewer & Barton, 2012, 2014; Dumoulin & Wandell, 2008).

In this thesis, we used the embedded pRF analysis in the mrVista toolbox to extract eccentricity, polar angle and pRF size estimates. The pRF model was fit to the average of the all bar stimulus scans at each luminance level, for each participant. Stimulus details (aperture, timing) were fed into the pRF model, which consisted of a circular 2D Gaussian and was run with a two-gamma HRF to account for both positive and negative BOLD in the time series. The pRF analysis stream uses a coarse-to-fine approach, resulting in pRF estimates for voxels in which the model explains at least 10% of the variance.

Chapter 3

The impact of different luminance levels on responses in early visual cortex

3.1 Abstract

The visual system is able to process information over a large range of light intensities. Under photopic conditions, visual information is processed at the retinal level by cone photoreceptors, while under scotopic conditions visual signals are solely conveyed by rod photoreceptors. There is a markedly different distribution of rods and cones across the retina, most notably in the central fovea, where only cones are found. Thus, under scotopic conditions there is an absolute central scotoma. At the level of the cortex, there is also a lack of input to the zone representing the fovea – often referred to as the foveal confluence. In addition, spatial resolution is lower under scotopic compared to photopic conditions, which largely reflects the greater spatial summation properties of the rod system. We used functional magnetic resonance imaging (fMRI) and derived population receptive field (pRF) estimates under four different luminance levels to characterise how the cortical representation of rod driven signals differs from the representation of cone driven signals.

With decreasing light levels, proportions of V1 that represent the centre of the visual field showed a clear reduction in overall signal, while signals in V1's more peripheral representations seemed largely unaffected. We confirmed that cortical response levels in extrastriate areas are generally less affected by low light levels and detailed that the area of V2 representing the centre of the visual field was affected less than

equivalent representations in V1. Connective field modelling indicated a peripheral shift in V1 – V2 connectivity patterns under low luminance levels. This result could be modelled using only connective field estimates derived under bright luminance conditions, indicating that connectivity is not dynamically changing, but rather that V2 is able to integrate and normalise V1 signals over a larger area of the visual field. Finally, we aimed to gain more insight if also on a cortical level the brain signals reflect mechanisms that maximise sensitivity under low light levels. Here, we show that summation properties of the rod pathway are represented on a cortical level as pRF size increased significantly under low luminance levels in peripheral proportion of V1 that is driven by both, rod and cone input.

3.2 Introduction

This empirical chapter aims to examine how the visual cortical representation of rod driven signals differs from the representation of cone driven signals in normally sighted human participants. As these two classes of photoreceptors differ fundamentally in function, spatial distribution patterns and signal propagation, this is an interesting question in itself and will help to understand mechanisms how visual information is processed and integrated. Furthermore, characterising these two pathways in more detail will establish an important baseline for studying photoreceptor abnormalities. This chapter will first review the properties of rods and cones, their distinct spatial distribution and signal propagation mechanism before detailing the limited work to date on how the visual cortex represents signals from these photoreceptors.

The visual system is able to operate and integrate sensory information over a large range of light intensities (Hood & Finkelstein, 1986). Two different classes of photoreceptors achieve this: Rod and cones. While these photoreceptors partially operate at overlapping light intensities the end ranges selectively activate just one class.

Under bright, daylight conditions, vision is generally characterised by the ability to see colour and fine spatial details and is underpinned by the cone photoreceptors. In contrast night vision or vision under low light levels is mediated by rod photoreceptors and tends to be more be blurry, without fine spatial detail and is achromatic (Aguilar & Stiles, 1971; Hadjikhani & Tootell, 2000; Sharpe & Stockman, 1999). The distinct difference in visual experience depending on light level is related to the specific characteristics and spatial distribution of the two photoreceptor classes (Purves, Augustine, & Fitzpatrick, 2001).

Cone photoreceptors can be divided in three subclasses that are all tuned to different wavelength: long (L; red) middle (M; green) and short wavelength (S; blue) sensitive cones. The selective activation and interaction of these subclasses forms the basis of colour vision as signals from these three cell types are combined antagonistically by subsequent retinal cell types, which in turn define the three colour opponent pathways (Solomon & Lennie, 2007). Rod photoreceptors do not show any subdivision, thus selective activation of rods under scotopic, dim light conditions results in only achromatic perception. While this explains the differences in colour perception more factors contribute to the specificity for different light levels and the ability to perceive fine spatial detail.

These two photoreceptors show quite a distinct spatial arrangement in the retina (Figure 3.1). Cones only accounting for 5% of photoreceptors but are most highly

concentrated at a small, central location of around 1°20' (horizontal diameter), referred to as the fovea. This local cone maximum decreases with retinal eccentricity and stabilises at a minimal density at around 15 degrees. In the foveola, an even smaller central region extending to 0.3-0.5 degree, there are only L and M cones, while S cones, generally sparser in number (15%), are distributed outside the foveola. In contrast, rod photoreceptors make up 95% of the photoreceptors and are mainly found in the peripheral parts of the retina with a peak density at around 20 degrees. The more central the less rod photoreceptors occur, resulting in a small but completely rod free zone of around 1°20' in the foveal region (Curcio et al., 1991; Curcio, Sloan, Kalina, & Hendrickson, 1990; Masland, 2001; Roorda & Williams, 1999).

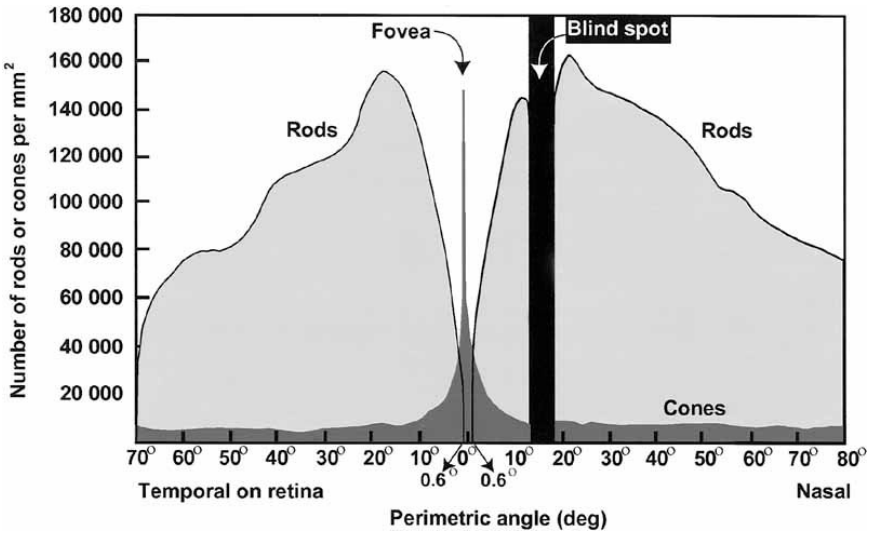

Figure 3.1 Schematic of rod and cone distribution across the retina. Rods (light grey) are more densely located in the periphery while the highest cone density (dark grey) is observed at the foveola. The blindspot marks the entrance point of the optic nerve (Hadjikhani & Tootell, 2000).

Photoreceptor spacing was thought to be the basis of spatial acuity as acuity in the foveola is closely correlated with the cone density and decreases with decreasing photoreceptor density. But outside the foveola, the actually observed spatial acuity is worse than what would be predicted from the photoreceptor mosaic alone, indicating

the influence of post receptor elements on visual acuity (Battista, Kalloniatis, & Metha, 2005; Green, 1970; Hirsch & Curcio, 1989). An important feature and a crucial underlying factor for light sensitivity and resolution is the difference in convergence ratio of photoreceptors on bipolar and ultimately retinal ganglion cells (RGC).

Indeed, the limiting factor for spatial acuity in the foveola is the density of L and M cones as each cone has a direct input onto RGCs via distinct cone bipolar cells (Curcio & Allen, 1990; Kolb & Dekorver, 1991; Wässle et al., 1990; D. R. Williams, 1986). The more peripheral, the convergence in the cone pathway increases but is still 10x less compared to the rod system, leading to a distinct difference in convergence ratio between the two pathways at the same peripheral location (Figure 3.2). Rod bipolar cells only indirectly link to RGCs and synapse to specific amacrine cells first, before integrating in the existing cone system via gap junctions or chemical synapse (Curcio et al., 1990; Goodchild, Ghosh, & Martin, 1996; Masland, 2001; Reeves, 2003; Sharpe & Stockman, 1999; Wässle et al., 1990)

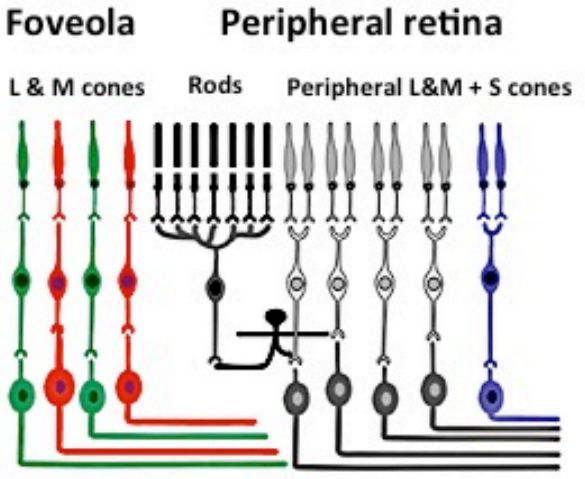

Figure 3.2 Simplified wiring diagram of different bipolar channels. While foveal L and M cones synapse in a 1:1 manner onto subsequent retinal ganglion cells, the input to bipolar cells in the peripheral retina is summed and input from more than one photoreceptor converge onto a single bipolar cell. The convergence is highest in the rod pathway (Figure adapted from (Masland, 2001)

While the rod photoreceptors are on the whole more light sensitive and the their photopigment, rhodopsin can be activated by a single photon energy quanta, the increased post synaptic convergence in the rod pathway works on top as an innate signal integrator allowing us to see even under extreme low light conditions (Barlow, 1956; Okawa & Sampath, 2007; Rieke & Baylor, 1998).

The convergence difference between these two parallel pathways should be reflected in the spatial summation properties of the respective pathway. Spatial summation can simply bee seen as the ability to sum up light quanta and Ricco' law (Ricco, 1877) describes the underlying basis of spatial summation:

$$\mathbf{L.\ A^n = k}$$

Equation 3.1 Ricco's law, were L represents the luminance of the presented stimulus, A the critical area of the stimulus, k is a constant while n refers to the spatial summation properties (1 = spatial summation, 0 = no spatial summation)

Due to spatial summation the threshold needed to perceive a certain stimulus is lower, as quanta reaching the photoreceptors in this critical area are summed up to one coherent output. Indeed, at a certain peripheral location Ricco's law holds and while it applies to the cone system as well, the critical area over which spatial summation happens is larger in the rod pathway, highlighting the increased convergence (Barlow, 1958; Hallett, 2003; Scholtes & Bouman, 1977; Sharpe, Stockman, Fach, & Markstahler, 1993; Westheimer, 1965).

Taken together, these mechanisms seem to optimise the visual system to detect high spatial resolution information, when light levels are high. In contrast, under scotopic conditions, when visual information is low, the visual system has the capability to pool the sparse information and increase light sensitivity at the cost of resolving fine spatial detail (Barlow, Fitzhugh, & Kuffler, 1957; Haegerstrom-Portnoy, Schneck, Verdon, & Hewlett, 1996).

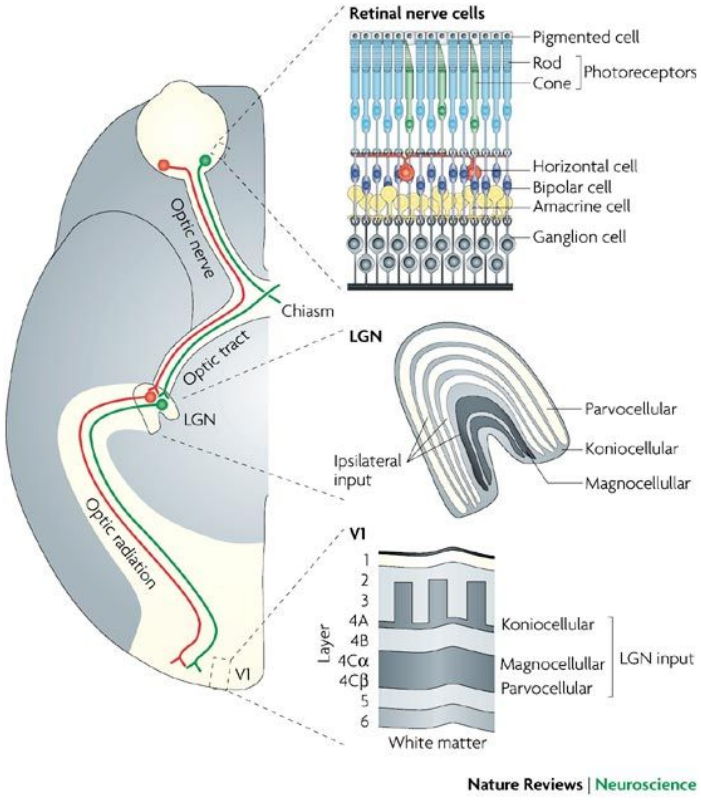

Figure 3.3 Illustration of the visual pathway from the retinal layers to primary visual cortex. Details about involved cell types and the layered structure of the LGN and primary visual cortex are depicted on the right. Red and green lines represent the nasal and temporal retinal projections respectively (Box 1, Solomon & Lennie (2007)).

Similar to bipolar cells there are also different types of RGCs with midget and parasol RGCs being the most prominent ones. Midget cells make up the majority, with the highest density at the centre of the retina and receive colour opponent input from L and M cones. Midget cells project to the parvocellular layer of the lateral geniculate nucleus (LGN), process colour information and due to their small dendritic fields allow for high visual acuity. In contrast, parasol cells are less frequent and receive the summed input from L and M cones in peripheral retinal area and project to the magnocellular layer in the LGN. As parasol cells have larger dendritic fields, spatial acuity is compromised while absolute contrast sensitivity seems to increase (Callaway, 2005; Dacey & Petersen, 1992; Merigan, Byrne, & Maunsell, 1991; Merigan,

Katz, & Maunsell, 2018; Rodieck, Binmoeller, & Dineen, 1985; Schiller, Logothetis, & Charles, 1990).

As mentioned before, rod photoreceptors integrate via amacrine cells in the existing cone circuit, but there is no clear consensus into which of these pathways. Generally, it is believed that rods selectively input into parasol ganglion cells and subsequently the magnocellular pathway. Input to the parvocellular layer via midget cells was shown to be weak and less distinct (Buck, 2014; Grünert, 1997; B. B. Lee, Smith, Pokorny, & Kremers, 1997; Purpura, Kaplan, & Shapley, 1988; Wiesel & Hubel, 1966). But some behavioural and psychophysical experiments question this and evidence has emerged that rod photoreceptors also impact the parvocellular pathway (Arden & Frumkes, 1986; Grünert, 1997; Lennie & Fairchild, 1994; Rudvin, Valberg, & Kilavik, 2000)

At the level of the LGN the impact of rod input and how scotopic vision is integrated into an existing network is not clear but even less is known about the impact of scotopic or rod vision on cortical estimates. So far only three studies in humans investigated or utilised rod vision. Hadjikhani & Tootell (2000) were the first to address how rod input affects the visual cortex in humans using fMRI. Analysing the differences in response to a simple stimulus shown at scotopic and photopic light levels, they tried to decipher if cone and rod input is indeed segregated at cortical stages. They found distinct activation of rod initiated input in most retinotopic organised visual areas but a selective absence of activation in colour related areas (V4) or the foveal representation of early visual cortex (V1) which corresponds with the actual perceptual difference between photopic and scotopic vision.

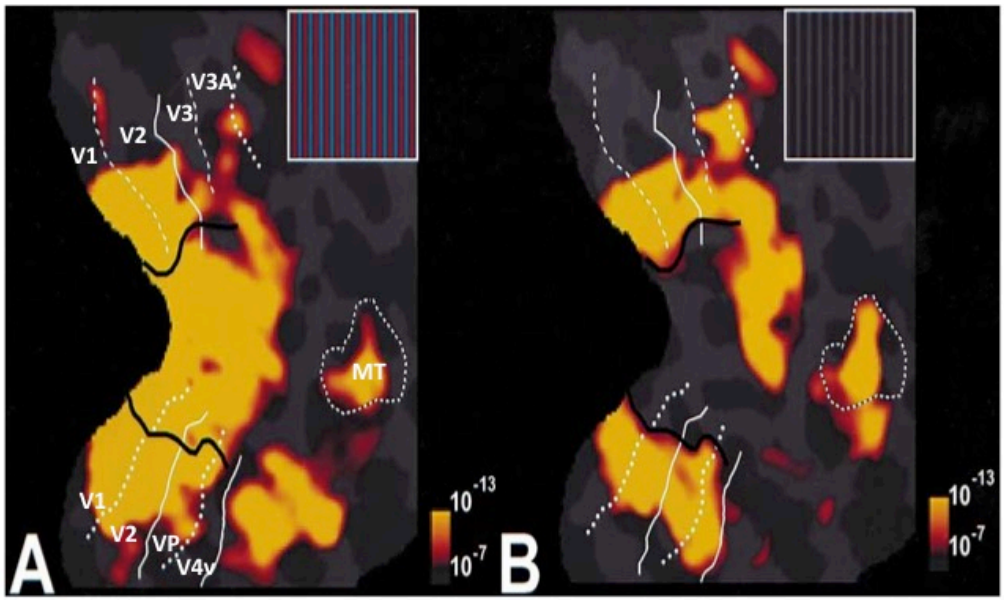

Figure 3.4 Unfolded representations of visual cortex (right hemisphere). Colour overlay represents cortical activation to the respective grating. Regions of interest are overlaid in white. A) Represents visual cortical responses derived during photopic conditions, while B) represents visual cortical responses when participants viewed the same stimulus during scotopic conditions (adapted from (Hadjikhani & Tootell, 2000).

They also showed that cortical areas that mainly receive input from the magnocellular layer, like the middle temporal visual area (MT) are highly driven by rod initiated input, supporting the notion that rod input predominantly feeds into the magnocellular pathway.

In a study by Baseler et al. (2002), scotopic vision in healthy human participants served as a natural control condition for studying reorganisation in achromats, a patient population that congenitally lacks any cone function.

Baseler et al. (2002) used phase-encoded retinotopy and measured the response to an expanding ring stimulus in both photopic and scotopic conditions. As expected, under scotopic conditions they found a large unresponsive zone in the foveal representations, which were nonetheless active under photopic conditions. This showed again that there is a cortical correlate of the rod scotoma. Subsequently,

Barton and Brewer (2015) tried to characterise the effect of scotopic vision on early visual cortex in more detail.

Using population receptive field (pRF) mapping they focused on the cortical effects emerging at the boundary of cortical rod scotoma. Similar to the other studies, they identified a large silenced cortical representation of the rod scotoma but also observed an ectopic pRF shift and variable changes in pRF size. These findings were interpreted as short-term adaptational changes due to the missing cone input but otherwise Barton & Brewer (2015) concluded no general difference in cortical response properties between cone and rod driven signals.

As mentioned before the convergence onto ganglion cells implies greater spatial summation of visual information for rod compared to the cone pathway. Thus, an increase in pRF size under scotopic compared to photopic conditions, especially in primary visual cortex, would seem plausible. The fact that Barton and Brewer (2015) found no such difference, could relate to the fact that they focused their efforts and analysis stream on the borders of the LPZ. Such a difference in summation properties might first of all be subtle and should be most prominent at more peripheral eccentricities that are driven by both, cones and rods (Curcio & Allen, 1990; Curcio et al., 1990; Mustafi, Engel, & Palczewski, 2009).

3.3 Aims and Hypothesis

The aim of the study described in this thesis chapter is therefore to identify how different luminance levels affect properties of visual cortical representations. To investigate this we used fMRI to derive pRF estimates at four different luminance levels.

1. We first determined the level of significant cortical responses in primary visual cortex at the respective luminance levels to see whether a reduction in luminance also leads to a steady decrease in cortical responses in V1. Further, we superimposed the pRF centres on a visual field grid to highlight the visual field locations that elicited these significant response at each luminance level. In line with previous studies we would predict that cortical representation of the fovea in primary visual cortex will exhibit a much reduced or even absent signal caused by the absence of central vision under rod only conditions (Barton & Brewer, 2015; Baseler et al., 2002; Hadjikhani & Tootell, 2000).

2. While previous studies report a clear decrease in central V1 signalling it was already noted that a similar loss could not be observed in extrastriate or even adjacent areas like V2 (Barton & Brewer, 2015). It is possible that alternative mechanisms might be able to influence extrastriate cortical responses to improve vision under dim light levels. Interestingly, several studies reported extrastriate activation despite complete or partial V1 lesions, which may emerge from V1-bypassing circuits (Barbur, Watson, Frackowiak, & Zeki, 1993; Schmid, Panagiotaropoulos, Augath, Logothetis, & Smirnakis, 2009; Schoenfeld et al., 2002; Shigihara & Zeki, 2014). Additionally, it has been postulated that stimulus-induced filling in processes, elicited by top down feedback, might explain cortical responses in central visual field representations (Barton & Brewer, 2011; Barton & Brewer, 2015; M. A. Williams et al., 2008). We subsequently tested the level of cortical signalling in V2 to see if there was indeed a difference in cortical responses under scotopic conditions compared to V1. We asked if a response difference is linked to increased input of central visual field locations that elicited these responses in V2. We applied

connective field modelling to test if responses in the representation of the central visual field in V2 can be explained by altered feed forward connections between V1 and V2.

3. Further, we determined the effect of different luminance levels on population receptive field size. We first applied the conventional approach and plotted pRF size as a function of eccentricity. Next we implemented the same analysis stream but focused the approach on single, anatomically-defined, peripheral visual field representation within V1. If spatial summation is reflected at a cortical level, this should be represented in an increase in pRF size, especially at a cortical location that receives both cone and rod input.

3.4 Methods

3.4.1 Participants

Eight participants (mean ± SD age, 26.23 ± 4.4; 4 males) with normal or corrected-to-normal vision were recruited from the York NeuroImaging Centre participant pool. Each participant underwent four separate one hour luminance fMRI sessions and one short high-resolution structural scan session (included in one of the functional session). In each fMRI session, four functional pRF and two phase encoded runs were obtained. Six participants (mean ± SD age, 28 ± 4.56; 4 males) underwent an additional two, contrast fMRI sessions, comprising only four functional pRF runs per session. All participants gave informed consent to take part in the study. Experimental protocols received approval from the York Neuroimaging Centre's Research Governance Committee and were in accordance with the Declaration of Helsinki.

3.4.2 Data acquisition

3.4.2.1 Imaging parameters

All scans were acquired using a SIEMENS MAGNETOME Prisma 3T scanner. In brief, for high resolution, anatomical images one T1 weighted scan (TR, 2500ms; TE, 2.26ms; TI, 900 ms; voxel size, 1×1×1mm^3; flip angle, 7°; matrix size, 256×256×176), was acquired. All functional scan were acquired using a standard EPI sequence (TR, 1500ms; TE, 23ms; voxel size, 2.5×2.5×2.5mm^3; flip angle, 80°; matrix size, 64×64×30). Additionally, for each fMRI session a proton density (PD) scan with the same spatial prescription was acquired to facilitate alignment to the high-resolution

structural scan. More relevant information about the imaging parameters are described in 2.1.1 in more detail.

3.4.2.2 Stimulus parameters

All visual stimuli were generated with the Psychophysics Toolbox Version 3 (Brainard, 1997; Kleiner et al., 2007; Pelli, 1997) run on Matlab Version 2012a/b. Created stimuli were rear projected onto an acrylic screen situated behind the participants' head at a distance of 57cm. More stimulus display settings are described in more detail in 2.1.2.1.

For pRF mapping, a modified version of the previously described bar stimulus was used (Dumoulin & Wandell, 2008). Briefly, a bar shaped 100% contrast flickering checkerboard stimuli was swept on a mean grey background within a circular aperture (8 ° radius). For the contrast fMRI sessions only the carrier contrast of the bar stimuli was changed from 100% contrast to either 30% or 10%, respectively.

For all phase-encoded retinotopy runs, a modified version of the previously described expanding ring stimulus was presented (Engel et al., 1997, 1994; Wandell et al., 2007). Spatial (fundamental = 0.25 cycle/deg) and temporal frequency (2Hz square wave flicker) were adjusted for both stimuli to maximise responses under low luminance levels. During each stimulus run subjects had to completed an attention task where they were instructed to respond with a button press every time the included fixation cross changed width. More details about the stimuli design and the implemented task are described in 2.1.2.2.

3.4.3 Experimental parameters

3.4.3.1 Viewing conditions

In general, four different luminance settings were used: Two bright light conditions, referred to as C2 and C1 (max. luminance: 600 cd/m^2; max luminance: 20 cd/m^2) and two scotopic conditions, referred to as R2 and R1 (max. luminance = 0.01 photopic cd/m^2; max. luminance = 0.002 cd/m^2). While C2 represented the standard scan condition regularly used at the imaging facility, all other luminance levels were achieved with either a filter mounted in front of the projector wave guide (C1) or customised goggles fitted with neutral density filter foils (R2 and R1). For both scotopic conditions subjects were dark adapted for 30 minutes prior scanning.

A subset of participants (n = 6) underwent two further functional scan sessions where only the contrast of the carrier was changed. The luminance for both contrast scans was kept at the level of the C2 scan, as this represented the standard scanning conditions. More details about the light levels used and general viewing conditions are described in 2.2.3.1.

3.4.4 Data preprocessing

High resolution T1-weighted scans were automatically segmented into grey and white matter using the Freesurfer analysis suite 5.3 ((Dale et al., 1999; Bruce Fischl, Sereno, & Dale, 1999), http://surfer.nmr.mgh.harvard.edu/). The output was manually corrected for potential segmentation errors (using ITK_Snap (Yushkevich et al., 2006), www.itksnap.org) and the cortical surface reconstructed to create an inflated 3D mesh. This mesh was used for visualisation of derived retinotopic maps and region of interest (ROI) definition. Proton density scans were FAST corrected

(FSL, Zhang, Brady, & Smith, 2001) and skull stripped (BET) to facilitate alignment with the high-resolution structural scan.

Functional data was pre-processed and analysed mainly with the mrVista toolbox (VISTASOFT software package) run on Matlab 8.0 (2012b). In brief, data were corrected for spatial inhomogeneity and motion corrected, runs with high motion artefacts or low task performance were excluded. Remaining pRF or phase-encoded runs were averaged within each participant and aligned to their high resolution T1-weighted volume using both FSL (FLIRT) and mrVista tools (rxAlign). More details about both, structural and functional pre-processing steps are described in 2.3.1 and 2.3.2, respectively. Reliability of single runs compared to an averaged pRF session was tested in one participant, where variance explained, pRF eccentricity and pRF size estimates derived from a single run were correlated to estimates derived from the averaged mrVista session. As expected the overall variance explained was slightly better for the averaged runs, while pRF estimates were broadly comparable (Appendix A1).

3.4.5 Analysis streams

3.4.5.1 Phase-encoded retinotopy and population receptive field mapping

To determine the phase and therefore the eccentricity each voxel is tuned to the averaged phase encoded ring runs were analysed with the mrVista toolbox (computeCorAnal).

The averaged pRF runs were used to determine both, the eccentricity and polar angle information as well as pRF size. To determine the pRF centre position (x0, y0) and pRF size of each voxel we used the previously descried pRF modelling approach implemented in the mrVista toolbox (Dumoulin & Wandell, 2008).

More details about the analysis specific settings and underlying computations are described in 2.4.1 and 2.4.2, respectively.

Graphs (line graphs, box and whisker plots) were created using Prism version 8.00 for Mac (GraphPad Software, La Jolla California USA, www.graphpad.com) while all other graphs were created using Matlab (2017a).

3.4.5.2 Delineation of visual field maps

Both regions of interest (V1, V2) were defined by hand on the subject specific, partially inflated 3D mesh. Thus, all ROIs were restricted to grey matter voxels only. To identify the visual area boundaries, the estimated pRF eccentricity and polar angle maps were loaded on the mesh surface and boundaries were drawn following previously described conventions (Engel et al., 1997, 1994; Sereno et al., 1995; Wandell et al., 2007)

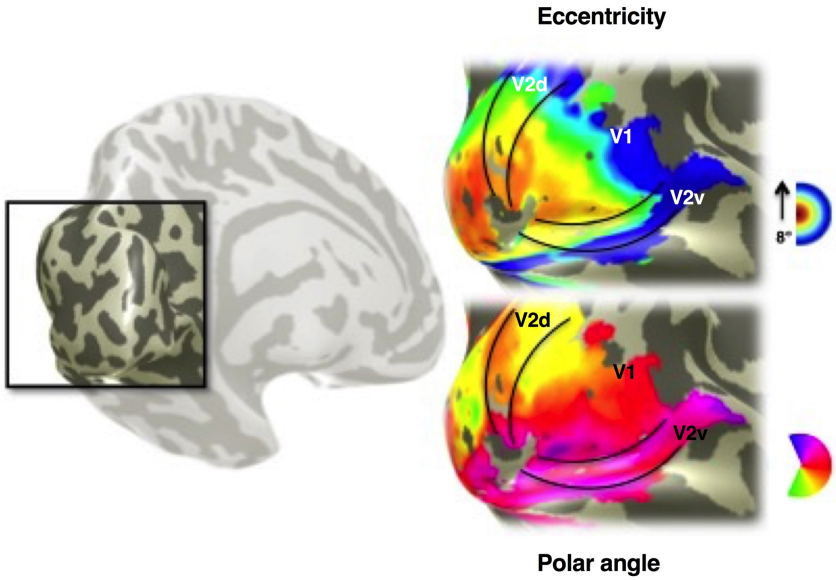

Figure 3.5 Delineation of visual areas. Left: Representation of the left hemisphere of one participant, shown as inflated cortical surface. Highlighted is the occipital cortex, shown in a zoomed in version on the right hand side. Eccentricity map (top) and polar angle map (bottom) are overlaid as surface on the 3D mesh. Reversals in the polar angle map were used to define the boarders of adjacent visual areas.

In more detail, the eccentricity map allowed a precise definition of the foveal confluence and the anterior extent of visual activation while the polar angle map revealed phase reversals that delimit the ROI boundaries (Figure 3.5). The discontinuous quarter field representations of V2 (dorsal and ventral) were combined to full hemifield ROIs and subsequently, for both V1 and V2 left and right hemispheres were pooled together for further analysis. The manual definition of the ROIs lead to potentially overlapping ROI boundaries. As a consequence, voxels could

be common to both adjacent ROIs. To avoid this, a customised script was applied that identified potential shared voxels and removed the intersection (Vernon, Gouws, Lawrence, Wade, & Morland, 2016). In our case, the distance of these shared voxels to the centre of the ROI pairs (either V2v/V1 or V1/V2d) was calculated using Z scores (to account for ROI size) and the voxel subsequently reassigned to the ROI with the closest centroid.

Peripheral V1 ROI

In addition, an anatomical, V1 ROI, representing eccentricities where both rods and cones input to cortex, was defined utilising data collected in response to the expanding ring stimulus. Phase maps were derived applying the phase-encoded analysis stream (see Methods, 2.4.1). The V1 ROI defined via the pRF data set was used as general guidance (same underlying rendered 3D mesh) to draw a peripheral, anatomical V1 band, placed between the phase bands representing 3.5 and 6.5 degrees of eccentricity. Again, left and right hemispheres were pooled together for further analysis (Figure 3.6).

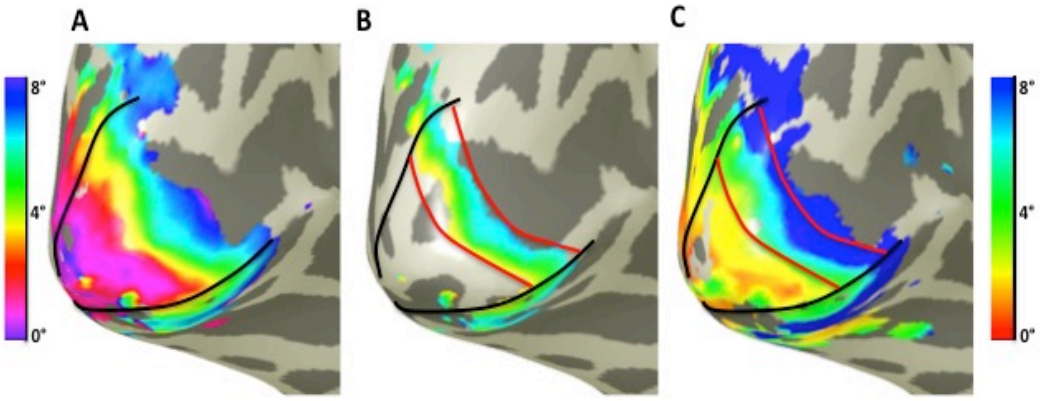

Figure 3.6 Example of the peripheral V1 ROI definition. (A) V1 overlaid in black on a phase map derived from the ring stimulus runs. (B) Restricted phase map to represent broadly the eccentricity bands between 3.5 and 6.5 degrees of eccentricity. This was used as a guidance to manually draw the peripheral V1 ROI, overlaid in red. (C) V1, overlaid in black and the peripheral V1 ROI, overlaid in red on the eccentricity map, derived via pRF mapping.

3.4.5.3 Connective field modelling

Connective field maps were estimated using the previously described connective field modelling algorithm (Haak, Morland, Rubin, & Cornelissen, 2016; Haak et al., 2013).

In brief, the connective field of a voxel describes the cortical area in a source location the respective voxel is connected to. Similar to the pRF analysis, a predicted time series for each voxel in a target ROI (V2) is predicted. To estimate connective field properties, a circular 2D symmetrical Gaussian is folded over the source ROI surface (V1), where V_0 determines the connective field centre the target is connected to and sigma the spread of the connective field. Similar to pRF modelling the optimal parameters for connective field centre and sigma are determined by minimising the residual sums of squares between the actual time series in V2 and the modelled time series from the Gaussian profile applied to the surface of V1. The underlying code for the connective field modelling approach was implemented as add-on to the mrVista toolbox. To run the model the source ROI (V1) was restricted and resaved to represent only one layer of grey matter voxels (the layer located at the grey/white matter boundary) and V2 was determined as the target ROI.

Only models were kept that explained at 15% of the variance in the observed time series (Haak et al., 2013). Conventionally, the cortical coordinates of the connective field are transformed into visual field co-ordinates on the basis of reading out the pRF co-ordinates that have been obtained from functional imaging. Connective field modelling can be applied to resting state data or stimulus driven activity. We were interested in applying the technique here because the rod scotoma effectively removes input from a distinct region visual cortex, while preserving signals in other regions allowing us to probe that effect's influence on connectivity.

3.5 Results

3.5.1 Effect of different luminance levels on the active proportion of primary visual cortex

To characterise the effects of luminance on visual field properties, fMRI data were collected for each subject under four different luminance conditions: C2 (max. 600 cd/m^2), C1 (max. 20cd/m^2), R2 (max. 0.01cd/m^2) and R1 (max. 0.002cd/m^2).

We first characterised the effects of different light levels on the cortical representation in primary visual cortex (V1). Figure 3.7 represents the population receptive field eccentricity estimates that are measured as a response to the bar stimuli presented under the four different viewing conditions.

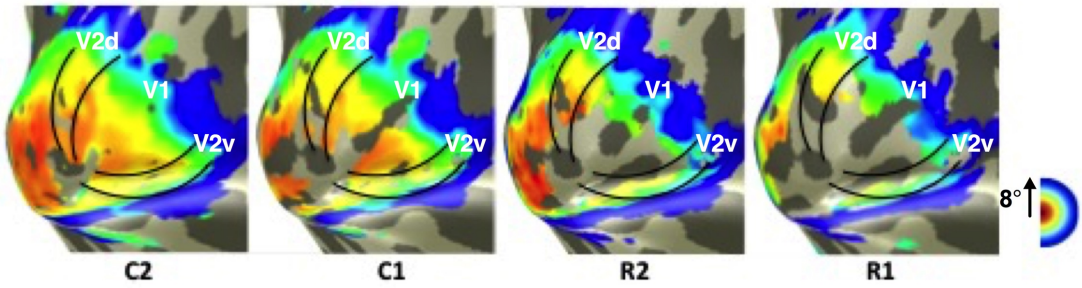

Figure 3.7 Effect of different luminance levels on pRF eccentricity representation in visual cortex. For each luminance condition the eccentricity maps derived form the luminance specific pRF model are shown for one participant. All maps are projected onto the left hemisphere of a rendered 3D mesh; visual boundaries are overlaid and shown in black.

These qualitative maps show a decrease in visual cortical responses with decreasing light levels. To quantitatively analyse this reduction in visual cortical response we identified the proportion of primary visual cortex that exhibits significant responses at each luminance level. Therefore, the number of voxels that exceeded 15% variance explained, which is seen as a robust signal (Haak, Langers, et al., 2014), was

determined per participant and divided by the total voxel count per V1 ROI to derive the percentage of active voxels (Figure 3.8).

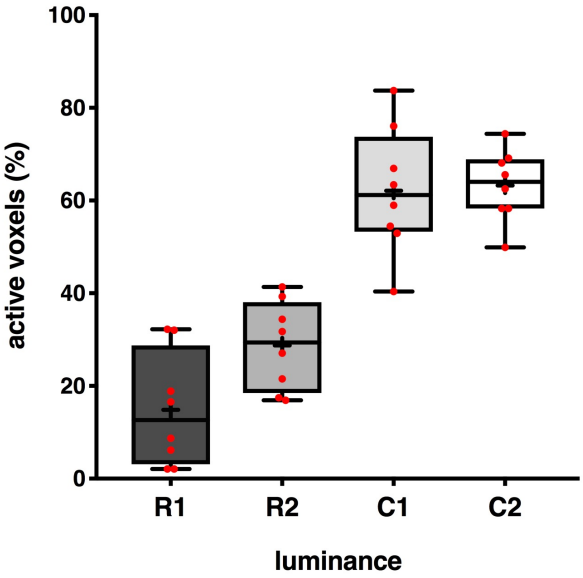

Figure 3.8 Percentage of active voxels in primary visual cortex plotted for each luminance condition. Active proportions of V1 are determined by the number of voxels that show at least 15% variance explained in relation to the total number of voxels within V1. Whiskers represent min. and max. values, with mean activation level per luminance condition denoted as '+'; individual data points are shown in red.

A repeated-measures ANOVA was performed to test for an effect of luminance on the dependent variable of 'percentage active voxels'. Mauchly's test of Sphericity was violated for the factor of luminance ($\chi^2(5)=13.375$, p=.022). Therefore, a Greenhouse-Geisser correction was applied. Luminance had a significant effect on 'percentage active voxels' ($F(1.336, 9.351) = 60.38$, $p < .0001$). Combined with the qualitative mesh images it seems that mainly the cortical area in V1, that represents the cone free foveal zone lacks BOLD signal under rod only conditions (R1, R2), whereby the non-responsive area increases with decreasing luminance (R1). More peripheral, parafoveal visual field representations of V1 seem largely unaffected under scotopic conditions.

Next, we wanted to estimate how the visual field is represented within primary visual cortex across different luminance conditions. This was done by visualising the

distribution of pRF centres (determined by x0,y0 of the pRF model output) of voxels that exceeded 15% variance explained on a visual field grid, where each bin spans approximately 0.5 x 0.5 degree each. For each ROI the number of pRF centres within each visual field bin was used to create luminance specific pRF centre 3D histograms (Figure 3.9). Each plot represents the full visual field stimulated (+/-8 deg) and constitutes a summary of pRF centres across all subjects. As voxel counts differed across conditions the colour overlay depicts the normalised (by the mean) voxel count per condition

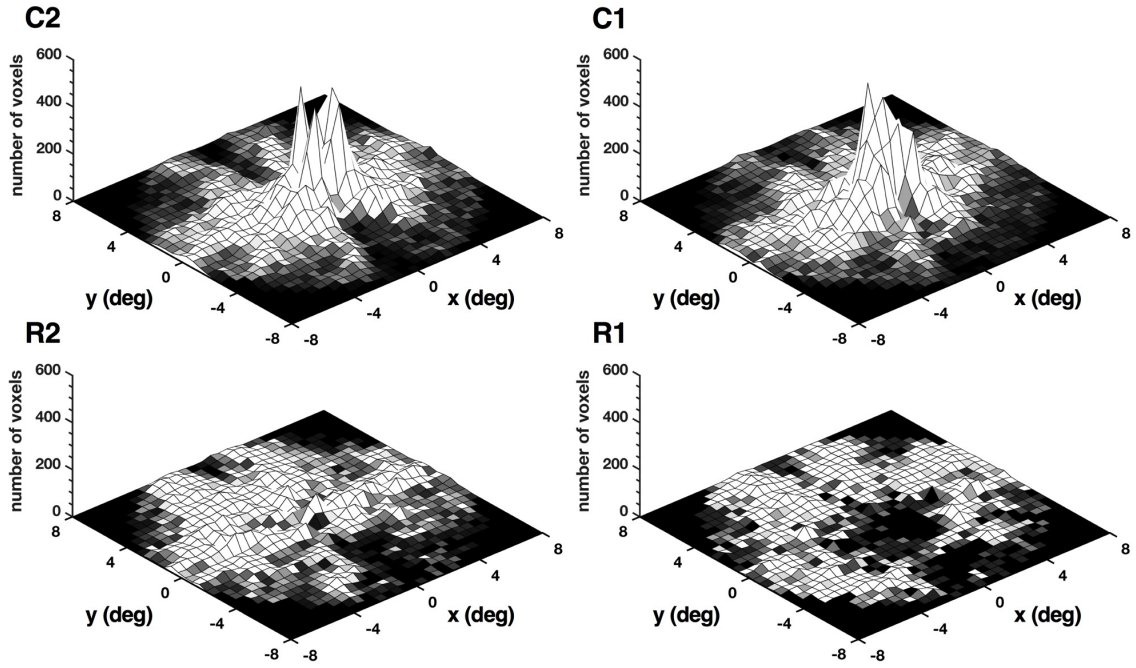

Figure 3.9 Difference in the pRF centre distribution at each luminance level in primary visual cortex. Plotted are number of voxels in each visual field bin per luminance condition. The centre distribution in V1 largely reflects the sensitivity distribution of the photoreceptors that operate the different luminance levels. Colour overlay is the normalised (by mean) voxel count.

These 3D histograms represent the location of the visual field that elicit significant responses within V1. This allowed us to recreate the visual responses seen in the cortex in visual field coordinates to emphasise the visual field location that elicits the main visual input. The pRF centres largely reflect the sensitivity distribution of the

photoreceptors that operate at the different luminance level (Osterberg, 1937), with a central 'cone peak' under bright light conditions (Figure 3.9, C2 and C1) and drop of central visual field representation under rod conditions (Figure 3.9, R1, R2).

3.5.2 Effect of different luminance levels on the active proportion of extra striate area V2

The reduction of central visual field representation in primary visual cortex under low light levels is generally consistent with previous studies, despite differences in the stimuli and analysis streams employed across studies (Barton & Brewer, 2011; Baseler et al., 2002; Hadjikhani & Tootell, 2000). Next, we assessed if low light levels affected extrastriate cortex in a similar way.

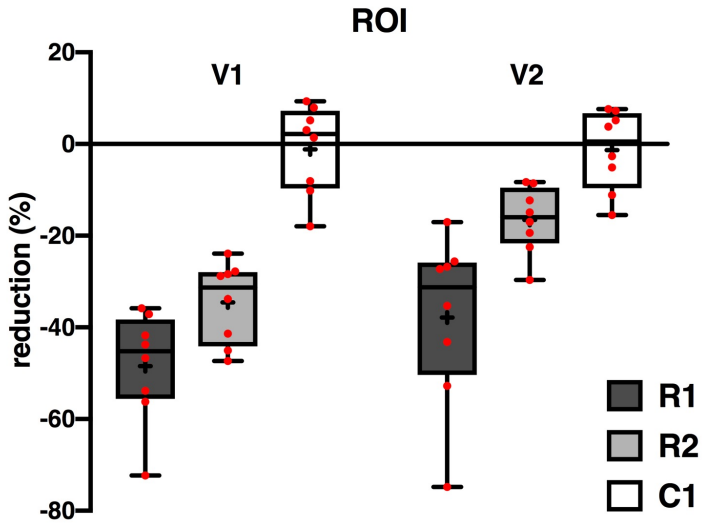

Figure 3.10 Mean reduction in proportion of visual cortex in which responses were detected plotted as a function of luminance in two ROIs. Reduction is calculated by subtracting the percentage of active voxels under photopic condition from the percentage of active voxels under the other luminance levels. Whiskers represent min. and max. values, with mean reduction level per luminance condition denoted as '+'; individual data points are shown in red.

To estimate potential differences, we calculated the percentage of reduction in cortical responses for both, V1 and V2 in relation to the significant response levels reached under photopic conditions (C2) (Figure 3.10).

A two-way repeated-measures ANOVA was performed with ROI and luminance condition as factors to determine any effect on percentage reduction of responsive cortex. Mauchly's test of Sphericity was not violated for the interaction factor ROI * luminance ($\chi^2(2)=1.516$, p=.469) and as the ROI factor has only two levels, sphericity can be assumed in this case for both factors. The luminance factor violated Mauchly's test of Sphericity ($\chi^2(2)= 6.632$, p=.036), therefore, a Greenhouse-Geisser correction was just applied to the main effect of luminance. A significant main effect of both luminance factor (F (1.198, 8.389) = 29.679, p< .0001) and ROI factor (F (1, 7) = 131.3, p< .001) were found, highlighting the general reduction in over all response level in both ROIs under low luminance levels. The analysis also found a significant interaction effect between ROI and luminance condition (F (2, 14) = 12.14, p= .001), indicating that visual cortical responses in V2 is less affected by low luminance levels compared to V1.

To determine if these differences in activation level were mainly due to an responses in cortical areas that represent the central visual field, the pRF centres of all voxels within V2 that reached at least 15% variance explained were superimposed on a visual field grid in the same way as previously for V1. The number of voxels within each visual field bin was used to create luminance specific pRF centre 3D histograms (Figure 3.11).

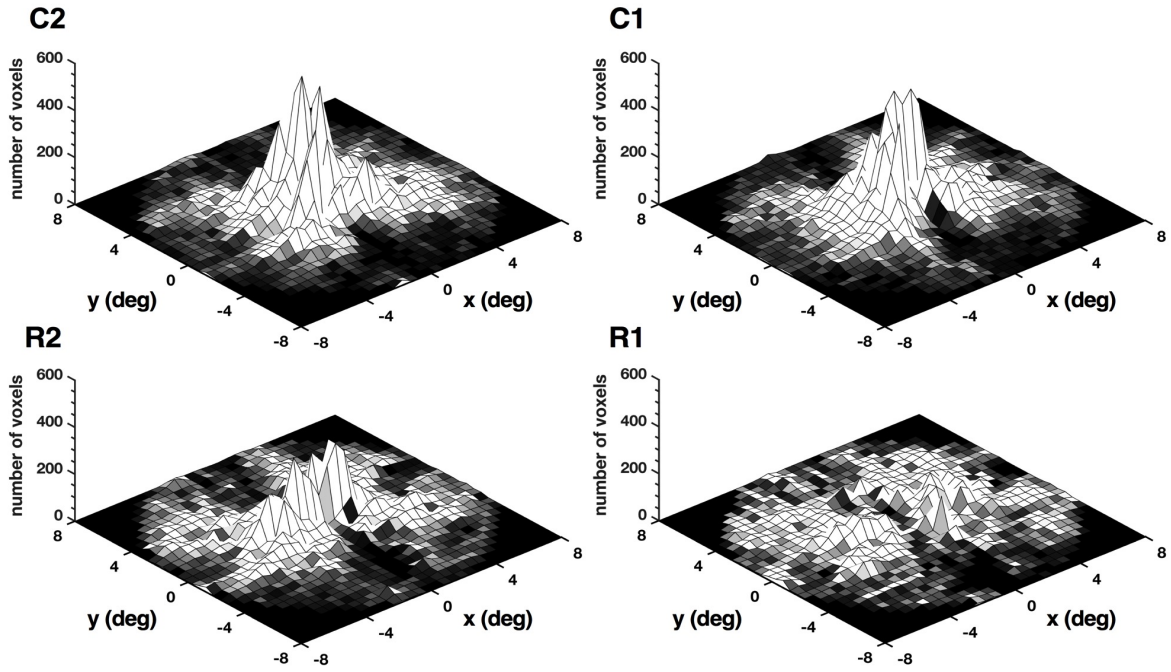

Figure 3.11 Difference in the pRF centre distribution at each luminance level in extra striate area V2. Plotted are number of voxels in each visual field bin per luminance condition. The pRF centre distribution in V2 highlights central activation under low luminance conditions.

Under bright light, cone conditions the 3D histograms are similar to what we observed in V1 (Figure 3,9; C2, C1). In both C2 and C1 a clear central, 'cone peak' is visible, highlighting again the centre of the visual field as the area that elicits the highest cortical responses under light conditions. Under low light, rod conditions, V2 shows a clear increase in central visual field voxel count compared to V1 (3.9). Under R2 a peak in central visual field locations is still evident while the complete drop out of central pRF centres is absent under the lowest light condition, R1.

3.5.3 Effect of different luminance levels on feed forward connections between V1 and V2

While pRF mapping estimates the population receptive field related to stimulus position for each voxel, connective field modelling uses the responses in a specific, source brain region to predict cortical responses else where in the brain (the target region). Using the connective field modelling approach to estimate if and how the functional connectivity between V1 and V2 changes in relation to light level might offer an explanation how extrastriate responses emerge in areas that represent central visual field locations under low light levels.

To determine the connective relationship between V1 and V2 we first established connective field properties from the averaged fMRI time series. This allowed us to obtain for each V2 voxels the associated centre coordinates that refer to specific voxels within V1. Eccentricity values for both V2 and connected V1 voxels were then 'read out' using the pRF models obtained at each luminance level and mean eccentricity values per eccentricity bin plotted against each other (Figure 3.12, left hand side). These plots were derived for all luminance levels, and importantly, for each plot the pRF model to read out eccentricity was matched to the luminance condition that was used to compute the connective field model.

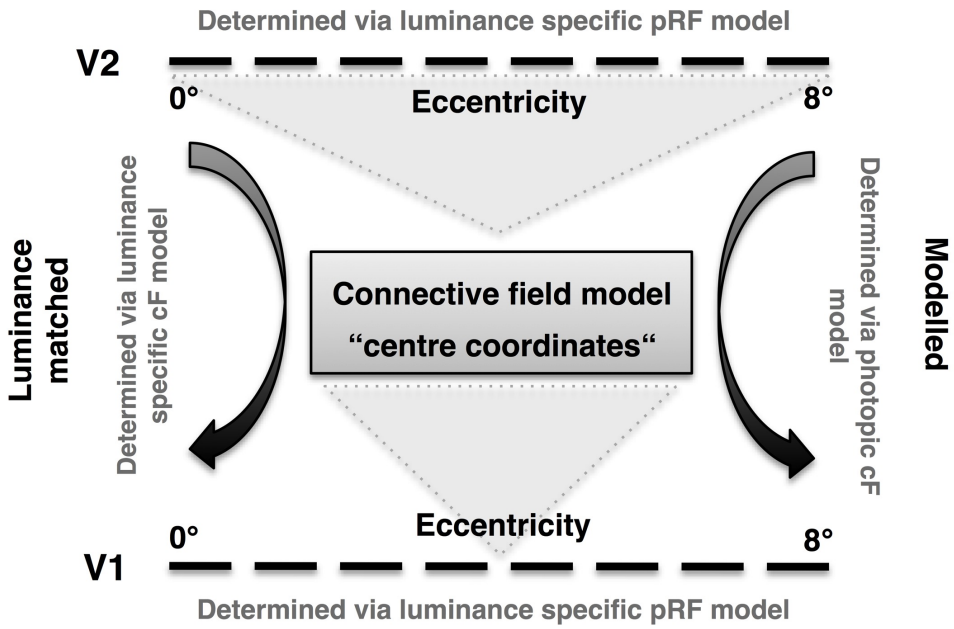

Figure 3.12 Schematic of connective field model analysis stream. To determine the V1 eccentricity a certain V2 voxel is pooling from two analysis streams are used for each luminance condition. In one stream both the pRF model and the connective field (cF) model used per light condition are luminance matched. In the modelled approach the connective field model derived under photopic condition is used for all luminance conditions while the pRF model is kept luminance specific.

For luminance conditions C2 and C1 the estimated eccentricity of the source (V1) and the target (V2) ROIs are highly correlated (Figure 3.13A). Small differences are expected as eccentricity boundaries and thresholding will induce a certain amount of noise. For rod conditions, R2 and R1, the central parts of V2 seem to pool visual information from more peripheral representations within V1, compared to cone conditions. Next, we applied the same analysis approach as before but asked whether the observed result can be modelled by using a single connective field model for all luminance conditions.

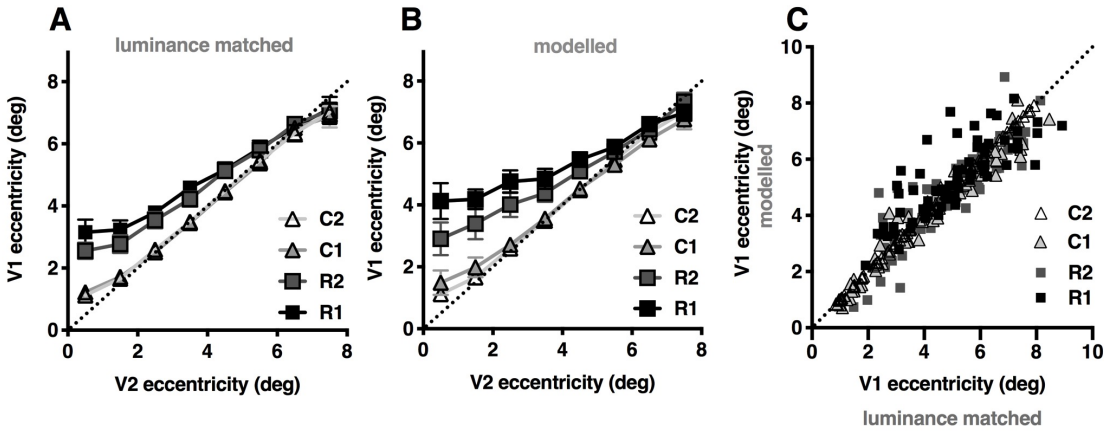

Figure 3.13 Effects of different luminance levels on feed forward connections between V1 and V2. To visualise the eccentricity location within the source ROI (V1) the target ROI (V2) is pooling from, V2 eccentricity is plotted against the estimated pooling eccentricity within V1 for each luminance condition. A) The connective field model and pRF model used are luminance matched for each light condition. B) In the modelled approach the connective field model derived from the photopic data set is used for all conditions. While the luminance specific approach indicates a more peripheral pooling location under low luminance levels the modelled approach confirms that the peripheral shift can be predicted with connective field estimates established under photopic luminance conditions. In both graphs the mean connected eccentricity values for V1 per eccentricity bin are plotted with standard error bars. C) Scatter plot correlating the actual pooling eccentricity as depicted in A against modelled pooling eccentricity as depicted in B. For all luminance conditions data points are centred around the unity line but variability increases with decreasing luminance. Plotted are single subject values per eccentricity bin.

We used the C2 connective field model as it reflects the well-understood stimulus-related responses across the entirety of both V1 and V2 ROIs (Figure 3.12; right hand side).

Subsequently, the V2 eccentricity was again plotted against the connected V1 eccentricity but this time the connections are solely established by the connective field estimate derived under photopic conditions (C2) while the luminance specific pRF model is used to read out eccentricity values (Figure 3.13B). The relationship between the eccentricity in the target area V2 and the source area V1 are very similar to results of the luminance-matched approach. It appears therefore that the connectivity between V2 and V1 is not dynamically changing between conditions,

rather that V2 signals that represent central locations sample stimulus driven V1 signals, even though they correspond to more eccentric visual field locations.

The relationship is explored further in Figure 3.13C where the connected V1 eccentricity of luminance-matched approach is plotted against V1 eccentricity of the modelled approach. The clear correlation between the connected V1 eccentricities of both analysis approaches underlines the idea that the connections established under photopic conditions are sufficient to explain the apparent peripheral shift seen under low luminance conditions. Further, under scotopic conditions more data points are located above the unity line, which indicates that the modelled approach slightly overestimates pooling eccentricities (Table 3.1).

Light level	Upper field	Lower field
C1	48.44 %	51.56 %
R2	56.25 %	43.75 %
R1	62.50 %	37.50 %

Table 3.1 Overview of data distribution in Figure 3.12C. Denote are the percentage of data points that fall above or below the unity line.

To charaterise the increase in responses of central visual field locations in V2 in more detail we determined the actual signal in the central visual field represenations in V1. We used the centre coordinates associated with foveal V2 voxels (0-2° of eccentricity) and converted them to a 'centre coordinate' ROI for each participant. The pRF model used to determine V2 eccentricity estimates and the connective field model used to read out the centre coordinates are luminance matched for each participant. Similar to the previous analysis step we used the photopic, C2 models as they reflect the well understood stimulus related activity.

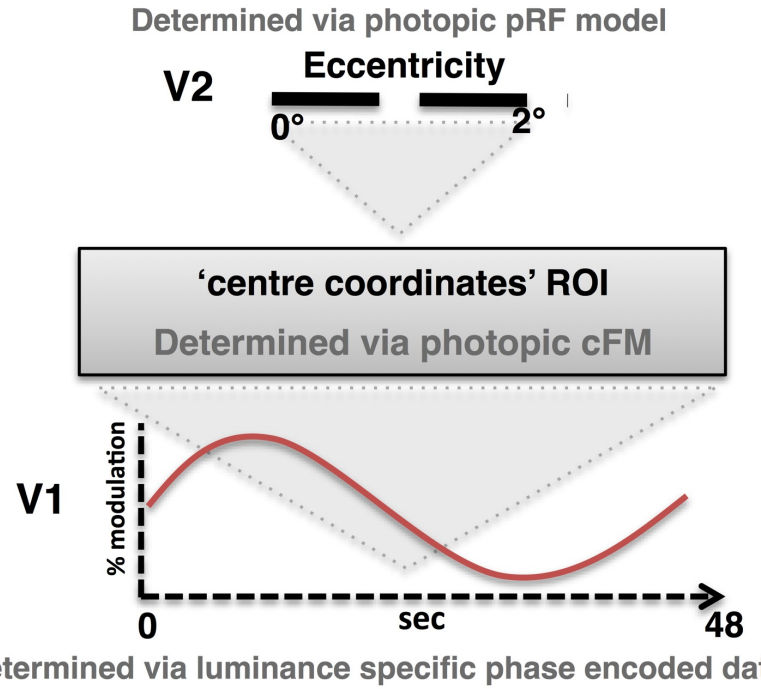

Figure 3.14 Schematic of single cycle analysis stream. For the central proportions of V2 (0-2 degree, determined using the photopic pRF model) the associated centre coordinates (determined via the photopic CFM) were saved as ROI for each participant. These ROIs were subsequently used on data set collected in response to the ring stimulus (phase-encoded) to extract the averaged modulation of the fMRI signal within V1 per participant for each luminance condition.

Theses ROIs were subsequently applied to an independent data set, where fMRI responses were measured in relation to an expanding ring stimuli. We then extracted the averaged fMRI time series modulation of a single stimulus cycle. A schematic of this analysis stream can be seen in Figure 3.14. In Figure 3.15 the percentage modulation is plotted for each participant under each luminance condition and the averaged modulation per luminance condition is overlaid in red.

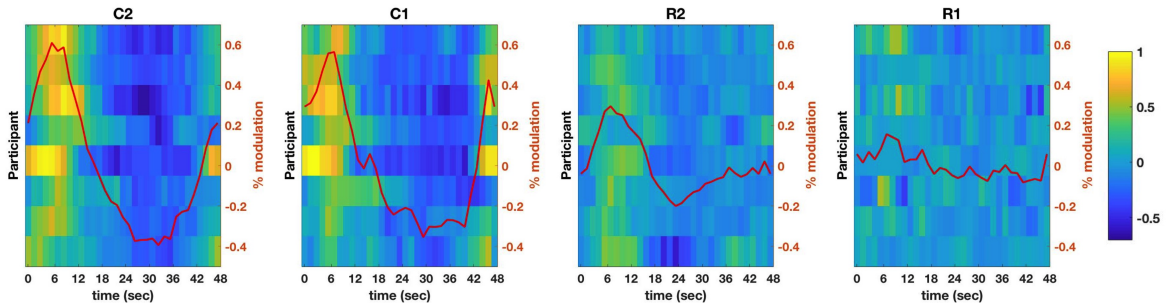

Figure 3.15 Averaged modulation of fMRI signal within a V1 ROI. Plotted is V1 percentage signal change of a single stimulus cycle (48 seconds) per participant and luminance condition derived from an independent data set collected in response to an expanding ring stimulus. The V1 ROI used for all conditions represents the centre coordinates associated with the central two degrees of the target ROI (V2) derived from the photopic connective field model. Under low light levels the modulation is shifted and less prominent or completely absent in primary visual cortex. Each line represents the averaged modulation in percentage signal change of a participant; overlaid in red is the averaged modulation per luminance condition.

For bright light conditions (C2, C1), the signal change of the averaged single cycle reveals a peak in modulation at the start of the stimulus cycle. Thus, the phase of the centre coordinate ROI is consistent with a central visual field representation. This highlights that under photopic conditions foveal proportions of V2 are indeed connected to central visual field representations in V1.

For the low luminance conditions however, the signal change in the same ROI is decreased (R2) or nearly absent in the lowest light condition (R1). While R2 still exhibits a stimulus evoked response, the phase seems slightly shifted to more paravofeal visual field locations while under R1 such a shift can only be assumed due to the nearly absent signal change.

3.5.4 Effect of different luminance levels on the pRF size estimates in primary visual cortex.

Next, we characterised the effects of different light levels on pRF size estimates in

primary visual cortex (V1). The 3D histograms of the pRF centre distribution in primary visual cortex (see Figure 3.9) demonstrated a clear overall decrease of voxels that reach a meaningful variance explained threshold with a decrease in luminance. Especially under the darkest condition, R1, consistent significant responses were absent in some subjects. This affected our analysis as only voxels that reached a fixed statistical threshold across all conditions can be entered into a repeated-measures ANOVA. In order to allow for a representative analysis only pRF size estimates of three luminance conditions (C2, C1, R2) under which a large numbers of voxels survived thresholding across all conditions were used, enabling us to compare luminance conditions on a voxel by voxel basis. Figure 3.16 shows the population receptive field size estimates obtained under the three different viewing conditions, C2, C1 and R2**.**

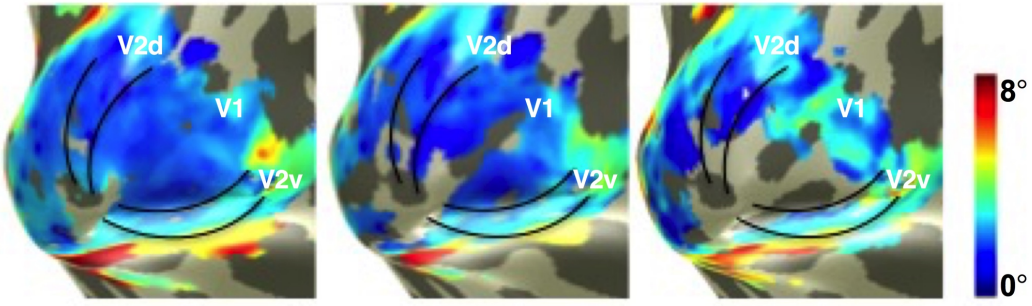

Figure 3.16 Effect of different luminance levels on pRF size representations in visual cortex. For each luminance condition the pRF size maps derived form the luminance specific pRF model are shown for one participant. All maps are projected onto the left hemisphere of a rendered 3D mesh; visual boundaries are overlaid and shown in black.

These qualitative maps indicate a slight pRF size increase under scotopic, rod only condition compared to cone conditions. To test this also quantitatively, we first plotted mean pRF size as a function of eccentricity to get a general idea about the impact of varying luminance levels (Figure 3.17) on pRF size estimates. Here, only

voxels were taken into account that exceeded 10% variance explained within the respective eccentricity bin across all luminance condition.

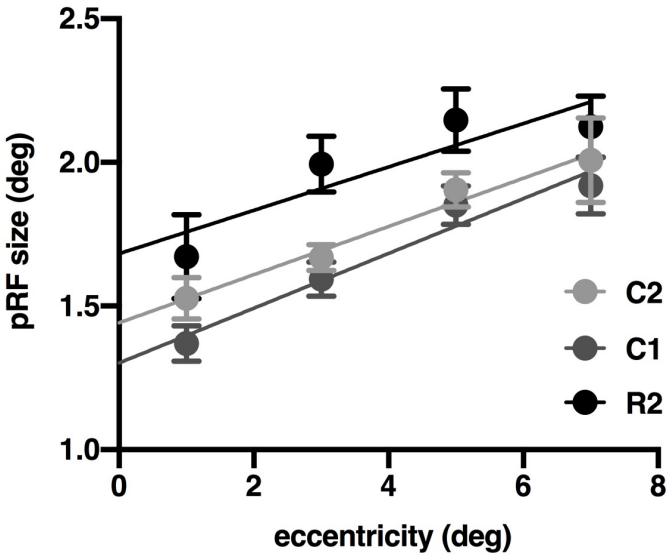

Figure 3.17 Mean pRF size plotted as a function of eccentricity for each luminance condition in primary visual cortex (V1). An increase in mean pRF size is visible across all eccentricities under low luminance condition (R2). Error bars denote the standard error of the mean.

In line with previous literature, pRF size scales with increasing eccentricity across all conditions (Dumoulin & Wandell, 2008). While light luminance conditions (C2, C1) show similar pRF size estimates across V1, increased pRF size values can be observed at each eccentricity bin under rod only conditions (R2). A repeated-measure ANOVA with luminance condition and eccentricity as factors on the dependent variable of pRF size was performed. Mauchly's test of Sphericity was violated for the factor of eccentricity ($\chi^2(5)=14.226$, p=.016) while for luminance ($\chi^2(2)=3.505$, p=.173) and the interaction factor eccentricity * luminance ($\chi^2(20)=29.469$, p=.135) sphericity can be assumed. Thus, only the main effect of eccentricity was Greenhouse-Geisser corrected. The test revealed a significant main effect of luminance (F (2, 14) =9.574, p= .002) as well as eccentricity (F (1.345, 9.412) = 9.385, p= .009), with no significant interaction between these factors (F (6, 42) = .721, p= .635).

As low luminance levels could have affected the pRF model fit, pRF size was subsequently plotted against variance explained to examine if increased pRF size estimates show overall lower variance explained (Figure 3.18). A repeated-measure ANOVA with luminance condition and eccentricity as factors on the dependent variable of pRF size was performed.

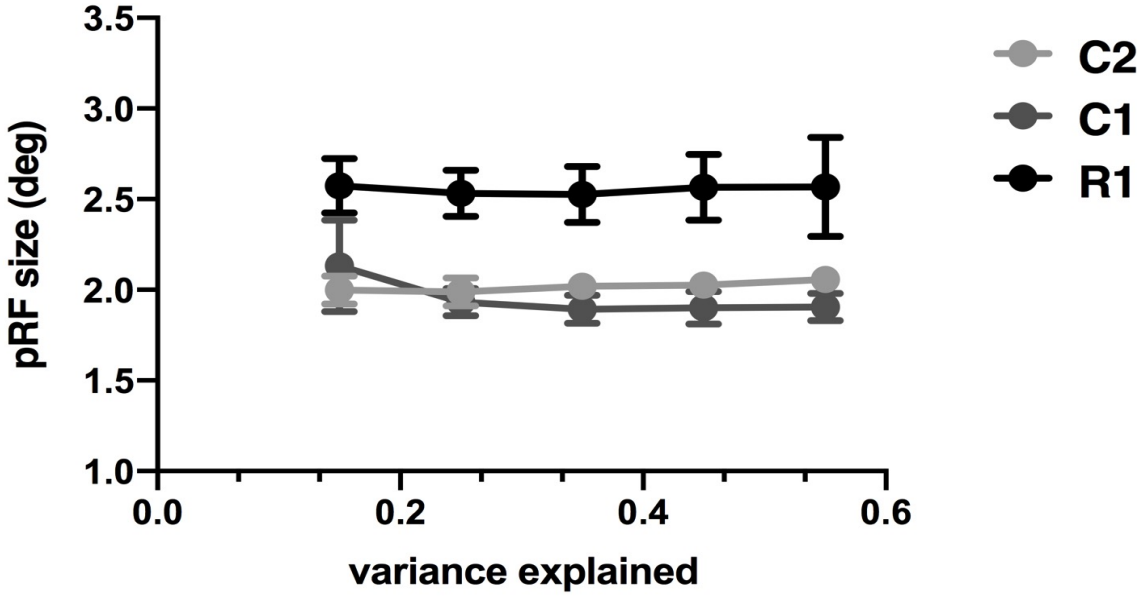

Figure 3.18 Mean pRF size plotted as a function of variance explained for each luminance condition in primary visual cortex (V1). An increase in mean pRF size is visible across all variance explained thresholds under low luminance condition (R2). Error bars denote the standard error of the mean.

Mauchly's test of Sphericity was violated for the factor of variance ($\chi^2(9)=27.958$, p=.001) while for luminance ($\chi^2(2)=2.162$, p=.339) sphericity can be assumed. The test revealed a significant main effect of luminance (F (2, 14) =11.451, p= .001) with no main effect of variance (F (1.345, 9.271) = 9.385, p= .924, Greenhouse-Geisser corrected) and no significant interaction between these factors (F (2.255, 15.787) = .508, p= .632, Greenhouse-Geisser corrected).

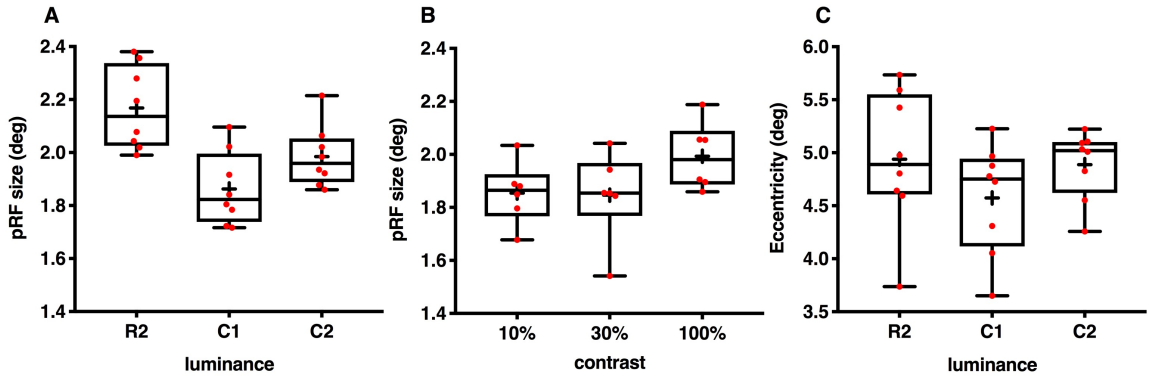

Figure 3.19 pRF size increases at lower light levels in an anatomical defined, peripheral V1 ROI. An anatomical V1 ROI was defined per subject utilising data collected in response to an expanding ring stimulus, spanning the peripheral eccentricity bands between 3.5 – 6.5 degrees. These peripheral V1 ROIs were applied to analyse the pRF data set. pRF size is plotted against luminance level (A) and stimuli contrast (B). For each luminance level also eccentricity was plotted against luminance level(C). Whiskers represent min. and max. values, with mean pRF size/eccentricity values denoted as '+'; individual data points are shown in red

While the analysis presented above conforms to the approach used by other authors, this has the downside that differences between conditions are compared irrespective of the actual cortical location in V1 of the voxels that yielded the pRF parameters. Thus, we implemented an additional approach, were we defined a specific eccentricity representation, which has the advantage that the analysis is carefully restricted to a cortical location and establishes whether a single measure derived from the pRF model differs between conditions. The anatomical ROI was defined on an external data set, collected in response to an expanding ring stimulus, as the eccentricity representation between 3.5 and 6.5 deg that receives input from both rod and cone photoreceptors (see 3.4.6.2).

As this ROI was defined on an independent data set, noise might be introduced to our pRF size estimates as sub threshold voxels or voxels at the edge of the stimulus boundary might be included in the analysis. Therefore, only voxels within the peripheral ROI were used that were actually within the stimulus boundary (assigned

eccentricity value below eight degrees) and exceeded 10% variance explained across all luminance conditions to be able to compare the effect of luminance level on pRF size on a voxel by voxel basis.

Subsequently, the mean pRF size for this ROI was determined per participant and plotted for each luminance level (Figure 3.19A). A repeated-measures ANOVA was performed to test the effect of luminance on the dependent variable of pRF size. Mauchly's test of Sphericity was not violated for the factor luminance on the dependant variable pRF size ($\chi^2(2)=.881$, $p=.644$), thus sphericity can be assumed. The test revealed a significant effect of luminance level on pRF size ($F(2, 14) = 9.464$, $p = .003$). To rule out the possibility that pRF size changes could simply be evoked by differences in stimuli contrast, the same ROI and analysis steps were applied on the contrast data set to derive pRF size estimates for each stimulus contrast level (10%, 30%, 100%).

Again, the mean pRF size was determined for the peripheral ROI and plotted for each stimulus contrast level (Figure 3.19B). A repeated-measures ANOVA was performed to test the effect of stimulus contrast on the dependent variable of pRF size. Mauchly's test of Sphericity was not violated for the contrast factor, ($\chi^2(2)=2.566$, $p=.277$), thus sphericity can be assumed. No significant effect of contrast level on pRF size ($F(1.357, 6.786) = 2.016$, $p=.204$) was found.

As pRF size was assessed within an ROI spanning a larger, peripheral area of ~3 degrees of visual angle the mean eccentricity value within the ROI might differ per luminance level and subsequently cofound pRF size estimates. Therefore, the mean eccentricity within the ROI was extracted per participant, applying the same thresholding criteria as before and plotted per luminance level (Figure 3.19C). A repeated-measures ANOVA was performed to test the effect of luminance condition

on the dependent variable of eccentricity. Mauchly's test of Sphericity was not violated for the luminance factor ($\chi^2(2)=3.303$, p=.192), thus sphericity can be assumed. The analysis showed no significant effect of luminance level on mean eccentricity (F (2, 14) = 1.179, p=.336).

In summary, therefore, a significant effect of luminance on pRF size while variations in potentially confounding factors, contrast and eccentricity, had no effect on pRF size.

3.6 Discussion

3.6.1 Summary of key findings

The experiments described in this thesis chapter aimed to characterise the effects of luminance on pRF parameters derived from V1 and V2 in healthy participants. We first estimated the proportion of significant visual responses in V1 under different luminance levels and showed that these significant responses systematically decrease with decreasing luminance level. Our analysis highlighted that low light levels affect mainly the central visual field representations in V1, while parafoveal areas still exhibit robust responses. In contrast to V1, V2 is significantly less affected by low light levels and shows distinct above threshold responses at central visual field representations. We examined these representations and found that short-term adaptation of feed forward connection under low luminance levels is not able to explain these responses. Our results also confirmed that an increase in convergence, a feature of the rod pathway, is still represented on a cortical level as luminance had a significant effect on pRF size and lead to increased pRF size estimates under low light levels.

3.6.2 Decreased response levels in central visual field representations

Our findings of decreased visual cortical responses under low luminance levels corresponds well with previous literature (Barton & Brewer, 2015; Baseler et al., 2002; Hadjikhani & Tootell, 2000). The implementation of different light levels extends their findings and shows that response levels decrease systematically under low luminance levels. While previous studies already emphasised that mainly central visual field representations are affected by scotopic vision (Barton & Brewer, 2015;

Baseler et al., 2002; Hadjikhani & Tootell, 2000), the distribution of the pRF centres, which resemble the sensitivity distribution of the photoreceptors that operate at respective luminance levels (Curcio et al., 1990; Osterberg, 1937), provides additional quantitative evidence. Notably, even though the overall number of central visual field representations under R2 is greatly reduced, the pRF centre histogram still shows pRF centres at central visual field representations. This is likely related to the size of each visual field bin, which spans approximately 0.5 x 0.5 degrees^2 of visual angle. The all-cone fovea has on average a diameter of ~1°20' but this estimation shows some individual variability (Curcio et al., 1991, 1990). Thus, some pRF centre estimates might fall at the border of the most central visual field bins, explaining the occurrence of central visual field representation even under scotopic condition. These central visual field representations are completely absence at R1, extending to around 2 degrees of eccentricity. Markedly, the absence of pRF centres seems mainly localised in the nasal visual field, which seems sensible, as it is know to have a higher cone coverage compared to the temporal visual field (Ahnelt, 1998; Curcio et al., 1990).

The extreme drop of in pRF centre representations at R1 is also likely related to lower signal-to-noise-ratio (SNR) and subsequent less significant responses. Indeed, the overall responses under this light level varied across participants and could reflect subject specific differences of effective scotopic vision (Fisher & Carr, 1970; Zuidema, Verschuure, Bouman, & Koenderink, 1981)

3.6.3 Extrastriate visual areas are less affected by low light levels

While a decrease in cortical responses under low luminance levels in primary visual cortex is well documented (Barton & Brewer, 2015; Baseler et al., 2002; Hadjikhani & Tootell, 2000) the effect of low luminance levels on response levels in extrastriate

areas has not been described in more detail. Barton and Brewer (2015) indicated that extrastriate areas seemed less affected but did not further quantify this observation. Indeed also the unfolded representations of visual cortex in Baseler et al. (2002) showed distinct responses outside V1. The results presented in the present study showed for the first time quantitative evidence that V2 is significantly less affected by low light levels. The pRF centre histograms also highlight that this is closely related to an increase of significant cortical responses representing the central visual field. This finding raises the question how the responses in central visual field representations in V2 emerge in the absence significant responses in primary visual cortex.

3.6.4 No differences in feed forward connectivity between V1 and V2

As V2 receives the main visual input from V1 (Girard & Bullier, 2017; Schiller & Malpeli, 1977) the simplest explanation might either be a form of short-term adaptation where the feed-forward connectivity between V1 and V2 could have been altered under low luminance condition or a general different feed-forward connectivity for rod only input.

The connective field modelling approach we applied showed a close relation of connected eccentricities between V1 and V2 under bright light conditions which is expected from their retinotopic organisation (Haak et al., 2013; Wandell et al., 2007). Under low light conditions an apparent peripheral shift of connected V1 eccentricities is evident for the central visual field representations in V2. This finding would support the hypothesis of changes in local feed-forward connectivity but has to be taken with precautions. From studies applying artificial scotomas in healthy human participants it is known that pRF estimates at the border of a LPZ tend to be biased to more peripheral visual field locations (Barton & Brewer, 2015; Baseler et al., 2011;

Haak et al., 2012) and seem to be caused by the pRF fitting procedure itself rather than actual changes to the underlying circuitry (Binda et al., 2013). As the connective field modelling algorithm relies on the same concept (Haak et al., 2013) a similar bias is possible where the cortical estimates of the rod scotoma under low luminance conditions results in a supposedly peripheral shift in feed-forward connections. The modelled approach we applied tested this possibility and utilised only connectivity estimates established under the photopic condition, which should be free of the aforementioned bias. Modelling the low luminance conditions correlated well with the initial result in the luminance-matched approach. Importantly, the modelled approach overestimated the peripheral shift. If changes in feed forward connectivity would have been real, the modelled approach should have underestimated the pooling eccentricity. Thus, it is quite likely that the connective field model approach is affected by a similar bias as the pRF analysis in the presence of a scotoma (Haak et al., 2012).

3.6.5. Foveal responses in extrastriate areas might underlie the increased spatial pooling properties of these visual areas

Another possible explanation for the occurrence of responses in central visual field representations of V2 could simply be related to the increased spatial pooling capacities of V2 (Shushruth, Ichida, Levitt, & Angelucci, 2009). While the pRF model we applied is not capable of capturing subthreshold stimulus related BOLD signals within the cortical representation of the rod scotoma in V1, the neural pooling properties of V2 might be able to sum and therefore de-noise the neural signals from V1 to the extent that a BOLD signal is registered. Such a mechanism would normalise

the response, which subsequently could to be identified as stimulus related signals by the pRF method.

Thus, the response profiles of the connective field related to the central two degrees of V2 were examined. As expected, under low luminance levels the percentage of modulation decreased systematically but traces of the stimulus related response profile could still be observed, even under the lowest luminance condition. Thus, this finding serves to support the possibility that the increased spatial pooling properties of extra striate alone might be able to explain the occurrence of stimulus related signals in absence of responses in primary visual cortex.

3.6.6 pRF size increases with deceasing luminance levels

pRF size was first examined in the traditional way as size estimates plotted against eccentricity for all luminance conditions. In line with the literature, pRF size scaled with increasing eccentricity across all conditions (Alvarez et al., 2015; Dumoulin & Wandell, 2008; Wandell & Winawer, 2015). Notably, the averaged pRF size estimates under the two photopic conditions were slightly larger at foveal eccentricities when compared with previous studies. This is probably caused by changes we implemented to the bar stimulus to maximise visibility under scotopic conditions where low spatial frequencies may preferably activate neuronal populations with slightly large receptive fields.

Overall, luminance had a significant effect on pRF size with increases observed across all eccentricities for scotopic conditions which was not related to changes in model fit caused by the lower luminance conditions. In the subsequent refined analysis stream the location for the region of interest was chosen, so that, depending on the luminance conditions, neurons within the respective voxels should either be driven

by cone or rod photoreceptors. Again, luminance had a significant effect on pRF size and estimates were increased under scotopic conditions, indicating that the pRF method we applied is capable of distinguishing between neuronal subpopulations (Alvarez et al., 2015; Yildirim, Carvalho, & Cornelissen, 2018).

While this increase in pRF size supports the initial hypothesis and would reflect the increased spatial summation properties of the rod pathway, this finding is in apparent discrepancy to Barton and Brewer (2015). They reported no size difference at peripheral eccentricities and related this to surround suppression, a mechanism, where activation of the surround of a receptive field has an inhibitory effect (M. A. Smith, 2006; Spillmann, 2014). Once stimulated, this reduces the response of the respective neuron, thus could diminish any potential convergence differences between rod and cone pathways (Barton & Brewer, 2015). While surround suppression could theoretically explain the absent size increase it has to be noted that there is no clear consensus if surround suppression is even a relevant feature under scotopic condition (Barlow et al., 1957; Enroth‐Cugell & Lennie, 1975; Kaplan, Marcus, & So, 1979; Maffei & Fiorentini, 2017; Muller & Dacheux, 1997; Peichl & Wässle, 1983; Wiesel & Hubel, 1966).

But to be certain, external factors that could have influenced pRF size estimates in this study and lead to the apparent increase under low luminance levels have to be considered and ruled out first before any claims can be made.

As outlined previously, pRF estimates at the border of an LPZ result in larger pRF size estimates (Baseler et al., 2011; Haak et al., 2012). While this might have affected the first, standardised analysis stream, where pRF size is plotted across the full eccentricity range, the ROI for the second analysis stream was deliberately chosen at

an anatomical defined eccentricity beyond the LPZ, which should result in unbiased size estimates.

Another potential bias could relate to the stimulus itself as the interference with luminance level might have altered the stimulus contrast. Thus, size changes might not be related to difference in rod and cone input per se but are a simply a side effect of lower stimulus contrast. This possibility was tested and, similar to other reports (Yildirim et al., 2018), differences in stimulus contrast had no influence on pRF size and lower contrasts even resulted in marginally smaller pRF estimates rather than larger ones, which we found under low luminance conditions.

As pRF size scales with eccentricity (Dumoulin & Wandell, 2008; Wandell & Winawer, 2015), a difference in mean eccentricity across conditions within the peripheral ROI might also be able to explain the seen pRF size increase. As luminance had no significant effect on pRF eccentricity and differences in mean eccentricity across conditions were only subtle, this possibility is also unlikely to fully explain the increased pRF size estimates under low luminance conditions.

On the other hand, it might offer an explanation as to why Barton and Brewer (2005) did not report any size differences. For their analysis, pRF size estimates have been pooled over a large range of eccentricities (7 degrees) hence, their analysis stream might not have been sensitive enough to detect subtle changes in pooling properties. Studies on spatial summation further support this possible sensitivity loss as they highlight that that spatial summation was linked to distinct peripheral locations but absent or just marginal at others (Reeves, 2003; Scholtes & Bouman, 1977)

All factors considered, the results presented here support the notion that pRF size estimates increase under low luminance levels and most likely reflect the existing

differences in convergence ratio between the rod and the cone pathway on a cortical level.

3.6.7 Conclusion

Experiments described in this study examined the effects of different luminance levels on pRF estimates obtained from visual cortex. Previously, only partial information was available how cortical estimates are affected and most details focused on direct effects of the rod scotoma and less on the cortical differences between cone and rod initiated input. The increased convergence of the rod pathway and the spatial summation properties of extra striate areas are important novel findings and suggest two distinct cortical mechanisms which enhance perception of the surrounding world when visual information is sparse.

More globally, the detailed characterisation of rod-initiated input in healthy participants will inform future clinical studies in rod achromats. As outlined before, only with a clear model of cortical changes that are expected from the loss of visual input can we interpret patient-related data appropriately and make an informed decision about whether reorganisation occurred in this patient population or not.

Chapter 4

The effect of congenital photoreceptor abnormalities on population receptive field estimates in primary visual cortex

4.1 Abstract

Under bright light conditions a large region within primary visual cortex responds exclusively to signals originating from the cones in the fovea. Under scotopic, rod only conditions this region is inactive due to the spatial distribution of rod photoreceptors, which are absent in the fovea. Baseler et al. (2002) showed that in achromats, a patient population that congenitally lacks cone function, the cortical area that normally responds only to cone signals is responsive to rod signals, providing evidence of relatively large-scale cortical remapping.

In this chapter a multi centre project is described; it used both phase-encoded retinotopy and population receptive field (pRF) modelling to systematically assess cortical organisation in achromats in a larger cohort with contemporary methods. We recruited a cohort of 18 achromats, with varying clinical signs. We showed that achromats with atypical rod function had less robust and less extensive cortical activity than controls under scotopic viewing conditions and did not exhibit indications of remapping in either their phase encoded retinotopy or pRF scans. In patients whose rod vision was clinically normal we found that cortical representations were largely comparable with those found in controls under scotopic

conditions, again not indicating a large-scale remapping of the visual representations in primary visual cortex. While this result held at a group level, there were hints of remapping in a small number of individuals and this points to there being potential individual differences in organisation of the visual cortex that may need to be accounted for in restoration treatments in this patient group.

4.2 Introduction

The aim of this empirical chapter is to systematically assess differences in pRF estimates obtained from primary visual cortex, V1, in a large cohort of achromats compared to healthy control participants. In an initial study by Baseler et al. (2002) it was shown that in these patients the cortical region that normally represents cone input in V1 is responsive to rod driven signals, indicating cortical remapping.

Currently, novel therapeutic approaches are being developed and tested that aim to restore the absent cone function (Fine, Cepko, & Landy, 2015). While gene therapy is able to restore the cone signal transduction on a retinal level, cortical remapping might negatively influence or even diminish this success. To guide the identification of efficient clinical concepts for rehabilitation in this patient population this empirical chapter tries to systematically analyse the organisation of V1 in a larger patient cohort using a combined approach of phase-encoded retinotopy, which largely replicates the study by Baseler et al (2002), and pRF mapping under different luminance levels.

This chapter will first outline the disease geno- and phenotype in this patient population. Further focus on the current state of treatment options in form of gene therapy accompanied by some limiting factors is given before focusing on the cortical

organisation described in achromats and the importance for a systematic assessment in a lager patient cohort with contemporary techniques.

Inherited retinopathies are relatively common visual diseases, with a prevalence of approximately one in 2000 people worldwide and are characterised by the loss or dysfunction of photoreceptors (rods/cones) within the retina. While these visual disorders were previously not treatable, several recent clinical advances highlighted their suitability for gene therapy: Most inherited retinopathies are caused by a single monogenetic mutation, many of which are already identified (Berger, Kloeckener-Gruissem, & Neidhardt, 2010; Colella & Auricchio, 2012); Additionally, several animal models of disease exist that advanced the applicability and worked as proofs of concept of treatment efficacy, which built the baseline for human trials (Chader, 2002; Colella & Auricchio, 2012; Lansing, 2002). The clinical success and importance of gene therapy for inherited retinopathies can be seen in the recent approval of *Luxturna*, the first known gene-therapeutic drug for RPE65-related Leber congenital amaurosis (Patel, Boucher, de Léséleuc, & Visintini, 2016). Another inherited retinopathy that is currently a major target of gene therapeutic interventions is achromatopsia (ACHM).

This rare autosomal recessive disorder affects around one in 30 000 people worldwide and the typical, complete form leads to congenital dysfunction of all three types of cone photoreceptors. Affected individuals are commonly diagnosed at birth or primary infancy by characteristic disease traits. These include poor visual acuity, pendular nystagmus, marked photophobia and complete lack of colour vision, while the severity of each symptom is variable across individuals (Hirji, Aboshiha, Georgiou, Bainbridge, & Michaelides, 2018; Pang et al., 2010; Remmer, Rastogi, Ranka, & Ceisler, 2015). To date, six genes have been associated with AHCM. While most identified

genes (*CNGA3*, *CNGB2*, *GNAT2*, *PDE6H*, *PDE6C*) are implicated in the cone photo-transduction cascade (Chang et al., 2009; Kohl et al., 2000, 2012, 1998), the latest identified gene, *ATF6*, plays a crucial role in foveal development (Kohl et al., 2015). Around 80% of all ACHM cases are related to mutations in two genes, encoding for subunits of cGMP-gated cation channels*, CNGA3* and *CNGB3*, while *CNGB3* mutations have a higher prevalence in Europe and the United States whereas *CNGA3* is more common in the Middle East and China (Aboshiha, Dubis, Carroll, Hardcastle, & Michaelides, 2016; Ahuja, Kohl, & Traboulsi, 2008; Hirji, Aboshiha, et al., 2018; Kohl et al., 2005; Thiadens et al., 2009).

For these main implicated genes, animal models of disease are available and provided important insights for gene replacement therapies in ACHM. Several studies in both small (Alexander et al., 2007; Carvalho et al., 2011; Michalakis et al., 2010; Mühlfriedel et al., 2017; Pang et al., 2012) and larger animals (Banin et al., 2015; Gootwine et al., 2017; Komáromy et al., 2010, 2013) indicated the efficacy of this treatment route. Additionally, the general safety of subretinal gene delivery has already been shown in other inherited retinopathies and resulted in improvement of the disease phenotype (Bainbridge et al., 2008; Cideciyan et al., 2008, 2013; A. M. Maguire et al., 2008), which has motivated several on-going human trials in the most common forms of ACHM (NCT03758404, NCT03001310, NCT03278873, NCT02935517, NCT02599922, NCT02610582).

The success of gene-therapeutic interventions in ACHM depends first of all on the presence of cones in which function can be restored. Current state of the art retinal imaging techniques like adaptive optics scanning light ophthalmoscopy (AOSLO) allowed for a detailed in-vivo visualisation of the photoreceptor mosaic. Studies utilising this technique were able to confirm the presence of cones in achromats,

although indicating a reduction in number and a generally disrupted mosaic, which is highly variable across participants (Carroll, Choi, & Williams, 2008; Dubis et al., 2014; Dubra et al., 2011; Hirji, Aboshiha, et al., 2018; Langlo et al., 2016). Reduced rod function is another variability within the ACHM population that could affect efficacy of gene therapy. While a non-detectable cone response in electroretinogramm measurements is a standard clinical result used in the diagnoses process, lately more and more evidence emerged that highlighted an ACHM subpopulation with moderate to severely reduced rod function, often accompanied by macular atrophy (Khan, Wissinger, Kohl, & Sieving, 2007; J. Maguire et al., 2018; Moskowitz, Hansen, Akula, Eklund, & Fulton, 2009; Wang et al., 2012). The most severe reduction in rod function to date was linked to individuals with a mutation in *CNGB3* (J. Maguire et al., 2018) but in general atypical rod function does not seem to be a feature of just one specific mutation and can be observed across all underlying genetic backgrounds (Wang et al., 2012; Zelinger et al., 2015). An advantage for any form of therapeutic intervention is that ACHM is usually described as stationary (Genead et al., 2011; Hirji, Aboshiha, et al., 2018; Sundaram et al., 2014) but some studies also indicated progressive changes with constant loss of cone photoreceptors over time (H. Lee et al., 2015; Thiadens et al., 2010; M. G. Thomas, Kumar, Kohl, Proudlock, & Gottlob, 2011; M. G. Thomas, McLean, Kohl, Sheth, & Gottlob, 2012). This would shorten the time window for any therapeutic interventions, however all aforementioned studies were crosssectional studies and conducted with a small sample size. A current large-scale longitudinal study supported again the notion that ACHM is mostly stationary and if retinal changes occur they are rather minimal, opening up the time window for any intervention to the adult age (Hirji, Georgiou, et al., 2018).

Genetic testing and modern retinal imaging are more broadly integrated in clinical practice to carefully assess individuals and enhance the efficacy of therapeutically interventions, while effects of retinopathies like ACHM on visual cortical estimates are currently not frequently assessed and integrated in clinical practice.

From initial functional magnetic resonance imaging (fMRI) studies it is known that visual input from foveal cones is integrated in a large area of primary visual cortex. This cortical area, frequently referred to as the foveal confluence, responds in healthy individuals under photopic, cone driven, conditions but not under scotopic, rod only, viewing conditions as a result of the spatial distribution of cone and rod photoreceptors within the retina (Hadjikhani & Tootell, 2000; Horton & Hoyt, 1991). ACHM and the resulting absence of cone input leaves this cortical area deafferent and effects on cortical estimates were examined in a pioneering fMRI study by Baseler et al. (2002). They recruited three high–functioning, mainly clinical diagnosed achromats and applied retinotopic mapping methods to derive visual field maps. Controls were tested under two mean luminance conditions, 70cd/m^2 for cone and 0.07cd/m^2 for rod conditions, using silent substitution methods to selectively target the different photoreceptors. This distinction was not necessary for patients, and a simple black and white stimulus was used to test them at one luminance level (mean luminance, 7cd/m^2). Results of this study revealed significant cortical activity in the foveal confluence of achromats, which now seemed to encode more parafoveal input (Figure 4.1).

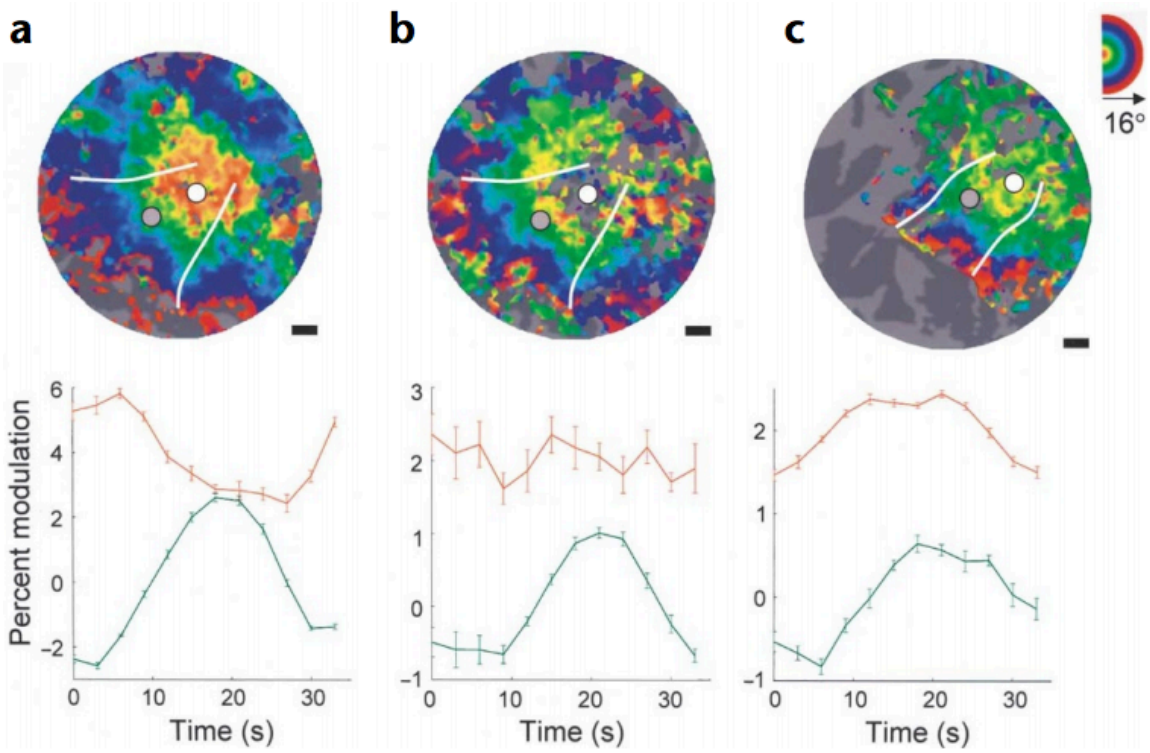

Figure 4.1 Evidence for cortical remapping in achromatopsia. Upper row: Unfolded representations of visual cortex. Colour overlay represents the eccentricity estimates form (a) a representative control subject under photopic luminance conditions where the foveal representation is highly active (red/orange), while (b) the same cortical area lacks activity under scotopic conditions due to the missing cone input. Measurements from a achromat (c) show distinct activity in the foveal confluence, indicating cortical remapping; Visual boundaries between V1 and V2 are overlaid in white; foveal (white) and paravoveal (grey) regions of interest are denoted as circles. Lower row: Plots represent the percentage modulation of a single stimulus cycle within the respective region of interest. While under photopic (a) both the foveal (red) and the parafoveal region of interest (ROI) (green) show distinct stimulus related response, the foveal response is absent (b) under scotopic conditions. Single cycle modulation of a rod achromat (c) shows still distinct modulation within the foveal ROI, while a shift in response phase is notable (Baseler et al., 2002).

This was taken as evidence for substantial remapping of the foveal representations in primary visual cortex and could, even after successful restoration of cone function, diminish the outcome, as the newly established cone signals might not be properly interpreted anymore.

4.3. Aims and hypothesis

Given the implications of this study and several recent reports of visual cortical changes in congenital disorders (Ahmadi et al., 2019; Hoffmann & Dumoulin, 2015; Hoffmann et al., 2012, 2003; Kaule et al., 2014; Muckli, Naumer, & Singer, 2009), there is a necessity to systemically assess the impact of ACHM on cortical representations in a large cohort of rod achromats to inform on current vision restoration approaches. Thus, the aim of this chapter is to recruit participants in a multi centre study at three different scanner (University of York, UK; Otto-van-Guericke University, Magdeburg, DE; Hadassah medical Centre, Jerusalem, IL) to achieve a representative patient cohort that incorporates not only individuals with both most common genes mutations (*CNGA/CNGB3*) but also represents achromats with typical (Rod^+) and reduced rod function (Rod^-). Functional MRI was used to assess cortical responses in this cohort and to compare the results to those obtained from healthy control participants under comparable viewing conditions. Focus was on two regions of interest in primary visual cortex, one representing the central regions of the visual field and one the more paracentral regions. Measures were taken under two different luminance levels: a bright light, photopic luminance condition and dim light, scotopic luminance condition.

We first applied phase-encoded retinotopy and analysed the data in line with Baseler et al. (2002). Therefore, we extracted time series information of a single stimulus cycle for each participant to visualise an initial overview of the data set. The response was then quantified as the signal amplitude at the stimulus frequency for regions of interest that represented 0 - 4 and >4 - 8 degree eccentricity in primary visual cortex. We also estimated the response phase for each region of interest (ROI), as measure

that assesses the eccentricity that is represented in the respective ROIs. These measures were, when possible, derived under two luminance levels, which captured rod and cone driven signals. Our main prediction is that under scotopic conditions patients will show greater responses at the ROI that represents that centre of the visual field and that these responses are tuned to more peripheral visual field locations.

The main aim of the study was to use contemporary population receptive field (pRF) methods to assess the cortical representation in patients with a view to determine whether remapping had occurred. We therefore chose to use multiple runs of moving bars to enhance statistical power. We opted for two measures of the cortical representation. The first was to assess the proportion of each ROI that responded above a statistical threshold. The second was to derive the eccentricity represented at each ROI. For both analysis streams, we generally expect a greater response in controls under photopic luminance levels at central visual field representations indicative of the prominent cone input in control participants in this condition. In comparison, under scotopic conditions retinal signalling in both participant groups is largely equivalent. Thus, signs of reorganisation should be most prominent here and result in greater responses in patients at central visual field representations. Similarly, remapping should lead to greater eccentricity estimates in patients in this central proportions. In more paracentral locations effects should overall be less pronounced as this area receives retinal input in both participant groups irrespective of the luminance condition.

4.4 Methods

4.4.1 Participants

York

Eight participants (mean ± SD age, 26.23 ± 4.4; 4 males) with normal or corrected-to-normal vision were recruited from the York NeuroImaging Centre participant pool. Additionally, 6 achromats (mean ± SD age, 40.17 ± 10.23; 3 males) were referred for scanning by collaborative sites. Each participant underwent up to two independent 1h luminance fMRI sessions and one short high-resolution structural scan session (included in one of the functional session). In each fMRI session, up to four functional pRF and two phase-encoded runs were obtained. All participants gave informed consent to take part in the study. Experimental protocols received approval from the York Neuroimaging Centre Science and Research Governance Committee and were in accordance with the Declaration of Helsinki.

Jerusalem

Three participants (mean ± SD age, 25.67 ± 7.02; 2 males) with normal or corrected-to-normal vision were recruited. Additionally, 6 achromats (mean ± SD age, 38.17 ± 5.64; 4 males) were referred for scanning by the Ophthalmology Department at Hadassah Medial Centre. Each participant underwent up to two independent 1h luminance fMRI sessions and one short high-resolution structural scan session (included in one of the functional session). In each fMRI session, up to four functional pRF and two phase encoded runs were obtained. All participants gave informed consent to take part in the study. Experimental protocols received approval from the Hadassah Hebrew University Medical Centre Ethics Committee and were in accordance with the Declaration of Helsinki.

Magdeburg

Eight participants (mean ± SD age, 36.75 ± 11.99; 4 males) with normal or corrected-to-normal vision and 6 achromats (mean ± SD age, 25.00 ± 13.46; 3 males) were recruited. Each participant underwent up to two 1h luminance fMRI sessions and one short high-resolution structural scan session (included in one of the functional session). In each fMRI session, up to four functional pRF and two phase encoded runs were obtained. All participants gave informed consent to take part in the study.

For all patients, standard clinical values like affected gene and rod function were known, either through clinical tests carried out at the respective site or the tests were already conducted by collaborators.

4.4.2 Data acquisition

4.4.2.1 Imaging parameters

York

All scans were acquired using a SIEMENS MAGNETOME Prisma 3T scanner. In brief, for high resolution, anatomical images one T1 weighted scan (TR, 2500ms; TE, 2.26ms; TI, 900 ms; voxel size, 1×1×1mm^3; flip angle, 7°; matrix size, 256×256×176), was acquired. All functional scan were acquired using a standard EPI sequence (TR, 1500ms; TE, 23ms; voxel size, 2.5×2.5×2.5mm^3; flip angle, 80°; matrix size, 64×64×30). Additionally, for each fMRI session a proton density (PD) scan with the same spatial prescription was acquired to facilitate alignment to the high-resolution structural scan. More relevant information about the imaging parameters is described in 2.1.1 in more detail.

Jerusalem

All scans were acquired using a SIEMENS MAGNETOM Skyra scanner at the Edmond & Lily Safra Center for Brain Sciences, Hebrew University of Jerusalem.

For high resolution, anatomical images one T1 weighted scan (TR, 2300ms; TE, 1.5ms; TI, 900 ms; voxel size, 1×1×1mm^3; flip angle, 9°; matrix size, 256×256×160), using a 32-channel surface head coil, was acquired. For all functional scan sessions only the posterior part of the coil was used, covering the region of the occipital cortex. The functional runs were made up of four 7-minute pRF stimulus presentations interleaved with two 5.5-minute phase encoded ring stimulus presentations using a standard EPI sequence (TR, 1500ms; TE, 27ms; voxel size, 2.5×2.5×2.5mm^3; flip angle, 70°; matrix size, 72×20×72). The coronal slices were aligned perpendicular to the calcarine sulcus and placed to cover the whole occipital cortex.

For each fMRI session a T1-FLASH inplane scan was acquired to facilitate alignment of functional scans to the high-resolution structural scan.

Magdeburg

All scans were acquired using a SIEMENS MAGNETOM Prisma scanner at the University Hospital, Magdeburg.

For high resolution, anatomical images one T1 weighted scan (TR, 2600ms; TE, 4.46ms; TI, 1100 ms; voxel size, 0.9×0.9×0.9mm^3; flip angle, 7°; matrix size, 256×256×256), using the posterior 32-channels of a 64-channel surface head coil, was acquired. Similar, for all functional scan sessions only the posterior part of the coil was used, covering the region of the occipital cortex. The functional runs were made up of four 7-minute pRF stimulus presentations interleaved with two 5.5-minute phase-encoded ring stimulus presentations using a multiband-accelerated

(factor 2) EPI sequence (TR, 1500ms; TE, 27ms; voxel size, 2.5×2.5×2.5mm^3; flip angle, 70°; matrix size, 72×20×72). The axial slices were aligned with the calcarine sulcus and placed to cover the whole occipital cortex.

4.4.2.2 Stimulus parameters

All stimuli were generated using the Psychophysics Toolbox Version 3 (Brainard, 1997; Kleiner et al., 2007; Pelli, 1997) in conjunction with 32-Bit MATLAB (Version 7.6.0; The MathWorks Inc., Natick, MA, 2008).

For pRF mapping, a modified version of the previously described bar stimulus was used (Dumoulin & Wandell, 2008). Briefly, a bar shaped 100% contrast flickering checkerboard stimuli was swept on a mean grey background within a circular aperture (8 ° radius).

For all phase-encoded retinotopy runs, a modified version of the previously described expanding ring stimulus was presented (Engel et al., 1997, 1994; Wandell et al., 2007). Spatial (fundamental = 0.25 cycle/deg) and temporal frequency (2Hz square wave flicker) were adjusted for both stimuli to maximise responses under low luminance levels. During each stimulus run subjects had to completed an attention task where they were instructed to respond with a button press every time the included fixation cross changed width. More details about the stimuli design and the implemented task are described in 2.1.2.2.

Stimuli set up was shared across sites to ensure that stimulus presentation was as similar as possible. Differences in the underlying stimulus script were site-specific trigger codes for each scanner to ensure stimulus presentation and scanners were synchronised. Further, screen settings were updated depending on research site, to ensure that the stimulus had the same appearance, was presented across the full

screen and size was adjusted to differences in screen-to-participant distance More details about the stimuli design and the implemented task are described in 2.1.2.2.

York

Stimuli were rear projected onto an acrylic screen situated behind the participants' head at a distance of 57cm. More stimulus display settings are described in more detail in 2.1.2.1.

Jerusalem

Stimuli were presented on 32 inch MR-compatible LCD Monitor (NordicNeuroLab,Bergen, Norway) situated at the end of the scanner bore behind the participants' head. All subjects viewed the screen via a mirror mounted on the head coil at a viewing distance of 131 cm.

Magdeburg

Stimuli were rear projected onto an acrylic screen situated in the bore of the scanner behind the participants' head using a 4K-resolution D-ILA Projector (JVC; DLA-RS49). All subjects viewed the screen via a mirror mounted on the head coil at a viewing distance of 35cm.

4.4.3 Experimental parameters

4.4.3.1 Viewing conditions

In general, two different luminance settings were used: A bright light condition, referred to as photopic and a low luminance condition, referred to as scotopic. Depending on the scanner site, a second photopic condition with reduced light was implemented for scanning patients. Table 4.1 summarises the used luminance levels across all sites.

	Photopic		Scotopic
Site	**Control**	**Patient**	**All participants**
York	600 cd/m^2	20 cd/m^2	0.1 cd/m^2
Magdeburg	100cd/m2	20 cd/m^2	0.1 cd/m^2
Jerusalem	400 cd/m^2		0.1 cd/m^2

Table 4.1 Overview of used luminance settings at the participating scanner sites. York and Magdeburg used two different photopic settings depending on the participant while the set up in Jerusalem only allowed for one photopic setting. Scotopic luminance levels were identical across sites.

For low photopic conditions in York and Magdeburg (max luminance: 20 cd/m^2) a neutral density filter (Formatt Hitech, Firecrest ND 85x85mm, ND1.5) was mounted in front of the projector to reduce the overall luminance. For the scotopic condition all participants wore customised goggles fitted with layers of neutral density foils to achieve the specified luminance. During all scanning conditions all light sources in the scanner rooms were switched off. For all scotopic scans subjects were dark-adapted for a minimum of 30 minutes before data were acquired. For all scans participants viewed the presented stimuli monocularly, where a patch covered the non-dominant eye. Viewing the stimuli with only the dominant eye was implemented to counteract strabismus seen in some of the patients and should in general minimise nystagmus, thus this should increase the fixation stability in our patient population.

4.4.4 Data preprocessing

York

High-resolution T1-weighted scans were automatically segmented into grey and white matter using the Freesurfer analysis suite 5.3 ((Dale et al., 1999; Bruce Fischl,

Sereno, & Dale, 1999), http://surfer.nmr.mgh.harvard.edu/). The output was manually corrected for potential segmentation errors (ITK_Snap (Yushkevich et al., 2006), www.itksnap.org) and the cortical surface reconstructed to create an inflated 3D mesh, used for visualisation of derived retinotopic maps and ROI definition. Proton density scans were FAST corrected (FSL, Zhang, Brady, & Smith, 2001) and skull stripped (BET) to facilitate alignment with the high-resolution structural scan.

Functional data were pre-processed and analysed mainly with the mrVista toolbox (VISTASOFT software package) run on Matlab 8.0 (2012b). In brief, data were motion corrected, runs with high motion artefacts or low task performance were excluded. Remaining pRF or phase encoded runs were averaged and aligned to the high resolution T1- weighted using both FSL (FLIRT) and mrVista tools (rxAlign). More details about both, structural and functional pre-processing steps are described in 2.3.1 and 2.3.2, respectively.

Jerusalem

Pre-processing of anatomical data was identical to the York workbench and is outlined in the section above. The functional analysis stream was adapted and initial steps were carried out in FSL. This was necessary due to the coronal slice prescription used at the imaging facility, changes in FOV between inplane and functional scan and an increased susceptibility to motion artefacts. In brief, orientation information was deleted for all functional and inplane scans using FSL (FMRIB Software Library; fslorient). The acquired inplane scan was padded, aligned to the first used functional volume and then aligned to the respective high-resolution structural scan using FLIRT (FMRIB's Linear Image Registration Tool). In case no inplane scan was acquired, the first used functional volume was used. After all alignments were quality controlled, dummy volumes (8) of all functional scans were

removed. Within scan motion correction was carried out with FSL's MC FLIRT (final (internal) sinc interpolation, (Jenkinson, Bannister, Brady, & Smith, 2002)). After this stage, all functional scans were aligned to the first used volume, similar to the mrVista approach, using FSL's FLIRT. Output was checked for persisting motion artefacts and affected runs were discarded. Left over functional scans were averaged and imported to the mrVista analysis stream and aligned to the high-resolution T1- weighted using mrVista tools (rxAlign).

Magdeburg

Similar to the York workbench the T1-weighted anatomical scans were automatically segmented using FreeSurfer ((Dale et al., 1999; Bruce Fischl, Sereno, & Dale, 1999), http://surfer.nmr.mgh.harvard.edu/) and the cortical surface reconstructed to create an inflated 3D mesh, used for visualisation of derived retinotopic maps and ROI definition. Functional preprocessing was first carried out using the FSL toolbox (https://www.fmrib.ox.ac.uk/fsl) for motion correction. Corrected runs with high motion artefacts or low task performance were excluded. Remaining pRF or phase-encoded runs were averaged and further analysed with the mrVista toolbox (VISTASOFT software package). Here, the functional data were aligned to the high resolution structural scan with innate mista Vista tool assisted by Kendrick Kays's alignment toolbox (github.com/kendrickkay/alignvolumedata).

4.4.5 Analysis streams

4.4.5.1 Phase encoded retinotopy and population receptive field mapping

To determine the phase and therefore the eccentricity each voxel is tuned to the averaged phase encoded ring runs were analysed with the mrVista toolbox (computeCorAnal).

The averaged pRF runs were used to determine both, the eccentricity and polar angle information as well as pRF size. To determine the pRF centre position (x0, y0) and pRF size of each voxel we used the previously descried pRF modelling approach implemented in the mrVista toolbox (Dumoulin & Wandell, 2008).
More details about the analysis specific settings and underlying computations are described in 2.4.1 and 2.4.2, respectively.

To estimate if the scanner signal across sites is comparable, coherence values for both utilised regions of interest (Details in 4.4.5.2) were extracted from the phase-encoded data set and plotted per scanner site (after sine arc transformation). A 2-way repeated-measures ANOVA (mixed design) revealed no main effect of scanner site ($F(1,57)=1.559$, $p=.2191$) and no interaction ROI*scanner site ($F(2,57) = .06981$, $p=.5017$), thus derived phase-encoded and pRF estimates were pooled across scanner sites for all reported analysis streams (Appendix A.2).

4.4.5.2 Delineation of visual field maps

The derived visual field maps in the patient cohort were not always sufficient to apply the standard approach for delineating regions of interest (ROI), as described previously in 3.6.4.2. Thus, we made use of an online available anatomically defined retinotopy atlas (Benson, Butt, Brainard, & Aguirre, 2014) implemented in the python analysis tool box 'neurophythy' (Benson & Winawer, 2018). The output of this atlas was used to create two ROI masks for each participant using the FSL toolbox (flsmaths), representing the central (0-4°) and paracentral proportions (4-8°) of V1. For each participant, these two ROIs were imported to mrVista (using nifti2ROI) and visualised on the subject specific rendered 3D mesh. As for some subjects the

segmentation files were manually corrected, the 'Benson' ROIs didn't always result in neat outlines on the mesh, thus all imported 'Benson' ROIs were manually traced on the subject specific mesh and saved (Figure 4.2).

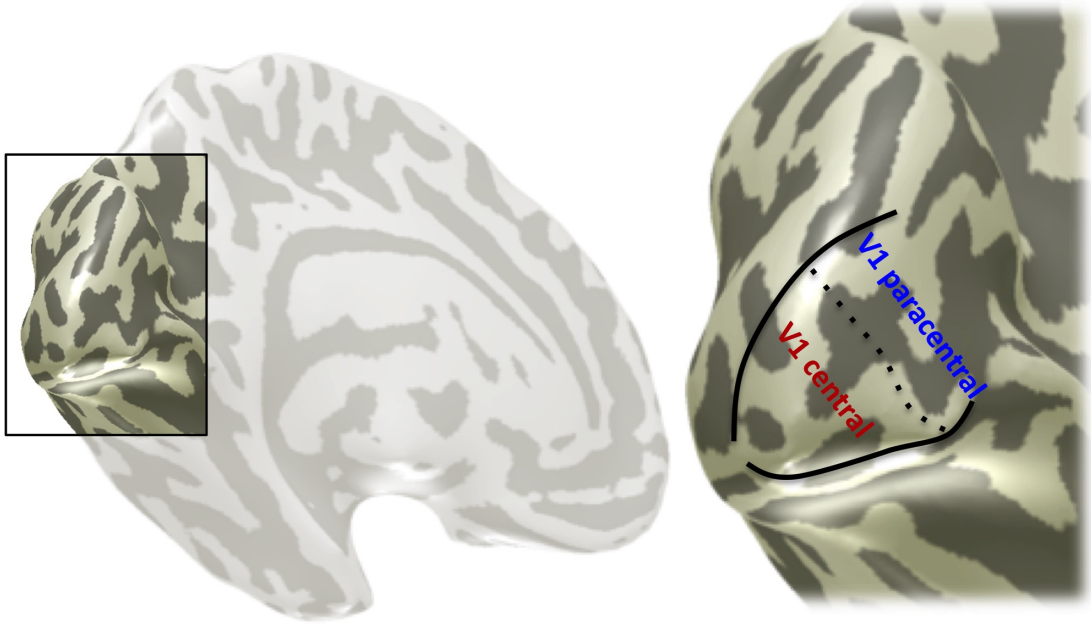

Figure 4.2 Delineation of visual areas. Left: Representation of the left hemisphere of one participant, shown as inflated cortical surface. Highlighted is the occipital cortex, shown in a zoomed in version on the right hand side. ROIs derived from the retinotopy freesurfer template (Benson et al., 2014) overlaid as surface on the 3D mesh. The V1 central ROI refers to cortical areas representing the central 4 degrees of the visual field while V1 paracentral refers to cortical areas representing paracentral areas (4-8 deg) of the visual field.

Again, a customised script was applied that identified potential shared voxels and removed the intersection. The distance potentially shared voxels to the centre of the ROI pair (V1 centre and V1 paracentral) was calculated using Z scores (to account for ROI size) and the voxel subsequently reassigned to the ROI with the closest centroid. Both, left and right hemispheres for the central and paracentral V1 ROI were pooled together for further analysis.

4.4.6 Statistical analysis

Two different analysis streams were applied to the data collected across all recruitment sites. The first analysis stream utilised the phase-encoded data set derived from the ring stimulus scan sessions. Here, all main approaches were kept similar to Baseler et al. (2002) where single cycle modulation, Fast Fourier Transform (FFT) and polar plots highlighting the phase and amplitude of each subject were compared between the control and patient data set.

The second analysis stream applied state of the art pRF mapping to the data set derived from the bar stimulus runs. Here, we detailed the percentage of significant visual responses in both ROIs within the patient and control cohort and looked at the mean eccentricity and pRF size of these significant responses within each ROI.

For all three described pRF analysis approaches a 2-way ANOVA was applied on the dependent variables 'percentage active voxels', 'mean eccentricity' and 'mean pRF size' to determine the effect of ROI and participant group for each luminance level. As both factors have only two levels sphericity can be assumed for all factors and a Greenhouse-Geisser correction was not applied. For multiple comparisons an independent samples T-test was applied for each ROI to test for an effect of participant group on either 'percentage active voxels', 'mean eccentricity' and 'mean pRF size'.

Graphs (line graphs, box and whisker plots) were created using Prism version 8.00 for Mac (GraphPad Software, La Jolla California USA, www.graphpad.com) while all other graphs were created using Matlab (2017a).

4.5 Results

To characterise the effects of ACHM on the cortical representation of the visual field we collected fMRI data for each subject during visual stimulation under different luminance levels. Two main analysis streams were applied, where the first stream was closely related to Baseler et al. (2002) and used conventional phase-encoded retinotopy, while the second stream applied state of the art pRF mapping. For both analysis streams all measures were extracted from two regions of interest in the primary visual cortex, were one represented the central proportion of the visual field (0-4 degrees, $ROI^{central}$) and the other more peripheral, pravavofeal proportions of the visual field (4-8 degree, $ROI^{paracentral}$). Table 4.2 presents an overview of all participants and highlights general demographics like scanner site, age and sex but also the different luminance levels each participant was tested at and the number of functional runs acquired at each luminance level. Additionally, for all patients, the affected gene and the level of rod function are noted.

Participant	Site	pRF	Luminance	TWA	Luminance	Age	Gender	
C	Y	4	P/S	2	P/S	25	f	
C	Y	4	P/S	2	P/S	25	f	
C	Y	4	P/S	2	P/S	34	m	
C	Y	4	P/S	2	P/S	28	m	
C	Y	4	P/S	2	P/S	24	m	
C	Y	4	P/S	2	P/S	20	f	
C	Y	4	P/S	2	P/S	30	f	
C	Y	4	P/S	2	P/S	23	m	
C	J	2/3	P/S	2	P/S	25	m	
C	J	4	P/S	2	P/S	33	f	
C	J	4	P/S	2	P/S	19	m	
C	M	4	P/S	2	P/S	27	m	
C	M	4	P/S	/	/	33	m	
C	M	4	P/S	2	P/S	58	f	
C	M	4	P/S	2	P/S	29	m	
C	M	4	P/S	2	P/S	53	f	
C	M	4	P	2	P	27	m	
C	M	4	P	2	P	35	f	
C	M	4	P	2	P	32	f	**Genotype**
R -	Y	4	P/S	2	P/S	40	f	CNGB3
R -	Y	4	P	2	P	28	m	CNGB3
R -	Y	2/4	P/S	1/2	P/S	34	m	CNGB3
R -	M	4/2	P/S	2	P	45	m	CNGB3
R -	M	4/2	P/S	2	P	16	m	CNGB3
R -	M	4/2	P/S	2/1	P/S	27	f	CNGB3
R +	Y	4	P/S	2	P/S	34	m	CNGA3
R +	Y	2	S	1	S	54	f	CNGA3
R +	Y	4	S	2	S	51	f	CNGA3
R +	J	3	S	2	S	42	m	CNGA3
R +	J	4	P/S	2	P/S	41	m	CNGA3
R +	J	3/4	P/S	2	P/S	35	m	CNGA3
R +	J	4	P/S	1/2	P/S	41	f	CNGA3
R +	J	4/2	P/S	2	P/S	42	f	CNGA3
R +	J	2	P/S	2	P/S	28	m	CNGA3
R +	M	4/2	P/S	2	P	16	f	CNGB3
R +	M	4	P	2	P	18	f	CNGA3
R +	M	4/2	P/S	2	P	22	m	CNGA3

Table 4.2 Participant demographics. Overview table summarising participant type, scanner site, age and gender and highlights acquired number of pRF or traveling wave (TW) stimulus runs for each luminance condition. If just one number is denoted for either pRF or phase encoded runs, this number is representative for all indicated luminance levels; (C = control, R- = atypical rod function, R+ = typical rod function, Y = York, M = Magdeburg, J = Jerusalem. P = photpic, S = scotopic, m = male, f = female);

The first analysis steps were kept similar to Baseler et al. (2002) and utilised fMRI response to the expanding ring stimulus analysed with the conventional phase-encoded approach. We first characterised the effects of photopic and scotopic luminance levels on the cortical representation in V1 of both patients and controls.

Figure 4.3 represents the eccentricity/phase estimates that are measured as a response to the presented expanding ring stimuli under two different viewing conditions.

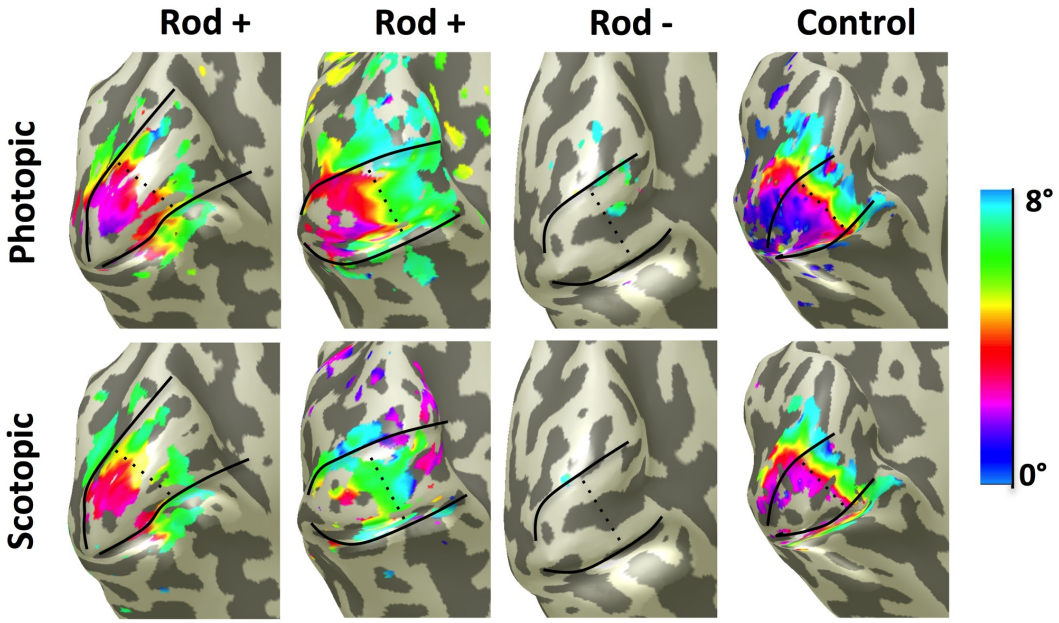

Figure 4.3 Eccentricity representations in primary visual cortex under different luminance levels derived via phase-encoded retinotopy. All maps are projected onto the left hemisphere of a rendered 3D mesh; Rod^{+} refers to patients with standard rod function while Rod^{-} refers to patients with below threshold rod function; visual boundaries of V1 (central and paracentral representation) are overlaid and shown in black.

These qualitative maps of representative subjects in each cohort highlight a decrease in visual cortical activation under low light levels (Figure 4.3). Noticeable, in both control and Rod^{+} patients, the cortical area in V1 that represents the cone free foveal zone lacks BOLD signal under scotopic conditions, but more peripheral, parafoveal visual field representations of V1 seem largely unaffected under scotopic conditions. Similar to the control participant presented here, the Rod^{+} patients showed a quite neatly organised topography. Interestingly, the patient with abnormal rod function (Rod^{-}) barley showed any visual cortical activation irrespective of the luminance condition. In general, although there was some variation in the representations

within each group, the patterns shown in Figure 4.3 are largely representative of the group data.

4.5.1 Signal modulation in a single stimulus cycle

As these maps only represent a qualitative measure for representative subjects in each group we extracted the averaged time series of a single stimulus cycle from all participant for an initial systematic and quantitative overview. The two ROIs (V1 central and paracentral) were used on the phase-encoded ring data set and the averaged time series of one stimulus cycle were extracted for each luminance level and participant. To ensure that artefacts, especially in the patient data with generally low % signal change were not interfering with the single cycle representation, the mean time series of all participants was inspected for potential artefacts. If spikes occurred at the same time in both ROIs, an artefact was assumed and the affected cycle deleted.

Per participant cohort, all individual modulations (% signal change) were plotted as a heatmap for each luminance level and ROI (Figure 4.4). Individual modulations were averaged to generate a group mean, which was overlaid in red on each subplot to show the overall luminance specific time series change within each ROI.

As outlined before, the phase of the time series represent the location in the visual field that elicits the highest response. As expected, the time series of controls under normal, photopic conditions for $ROI^{central}$ had the highest response at beginning of the stimulus cycle, indicating its central field representation, while the $ROI^{paracentral}$ showed a phase delay, as voxels within this ROI had more paracentral visual field representations. For control subjects under scotopic viewing conditions the overall signal modulation was reduced in both ROIs but it remains possible to see the

associated phase relationships of the ROIs. For patients under the photopic condition signal modulation for $ROI^{central}$ is nearly absent and no clear phase peak can be observed while the response in the $ROI^{paracentral}$ was still comparable to controls and indicated a parafoveal visual field representation. When tested under scotopic conditions patients exhibited a reduction in the amplitude of the mean response, as controls did, to the extent that the phase of the response is difficult to determine.

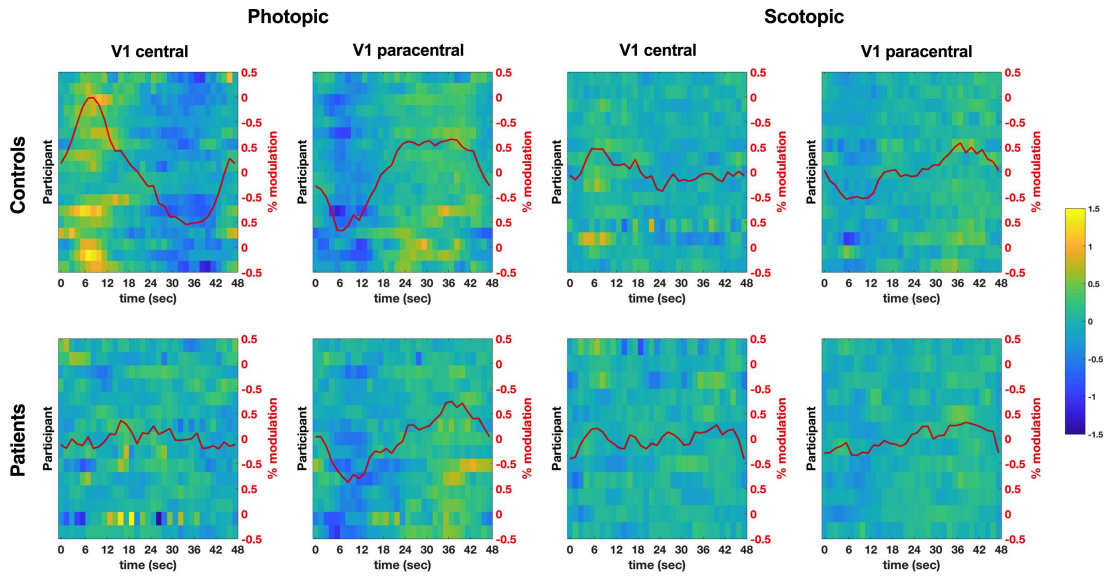

Figure 4.4 Averaged modulation of fMRI signal in primary visual cortex. Plotted are V1 percent signal changes of a single stimulus cycle (48 seconds). Top row: Single cycle modulation of control participants in the central and paracentral proportion of V1 under two luminance levels; Bottom row: Single cycle modulation of all achromats for each ROI per luminance level. Each heat map line represents the averaged modulation in percent signal change of one participant; overlaid in red is the averaged modulation per ROI; $n(photopic/scotopic)^{Control}$ = 18/15; $n(photopic/scotopic)^{Patient}$ = 15/12;

4.5.2 Fast Fourier transform of the mean time series

We further looked at the percentage signal change of the averaged time series, this time as a function of temporal frequencies close to the stimulus frequency (7 cycles/scan).

Here, the mean time series of the averaged ring runs was derived for each participant in each condition for both ROIs. When cycles had been deleted in the previous step due to artefacts, the missing cycle was interpolated (linear) to ensure each time series had the correct number of stimulus cycles (7). For each participant type (control / patient) an averaged mean time series was calculated per ROI in each luminance condition. These averaged time series were fast Fourier transformed into the amplitude spectrum (% signal change) and plotted as a function of temporal frequency.

Again, for controls the ROI covering the foveal region of V1 ($ROI^{central}$) showed a clear signal under photopic conditions, which was much reduced under scotopic conditions, reflecting the missing cone input. In comparison, a reliable signal could be observed in both luminance conditions for the $ROI^{paracentral}$ with a less pronounced difference in amplitude between luminance conditions compared to the $ROI^{central}$ (Figure 4.5, upper row).

In contrast, as already indicated by the single cycle raster plots (Figure 4.4), for patients $ROI^{central}$ showed very weak responses under the photopic condition and no response was evident in this ROI under scotopic conditions. However, both luminance conditions yielded responses from $ROI^{paracentral}$ that were comparable to those obtained from controls. As the quantitative mesh images highlighted a distinct difference in cortical activation between achromats with typical and reduced rod function, we superimposed the Fourier transforms of achromats with normal rod function (Rod^{+}) on all patient graphs. Under scotopic conditions, Rod^{+} achromats did not exhibit distinct signal differences from the whole group, while under photopic condition an increase, relative to the whole group, could be observed at the stimulus frequency in $ROI^{central}$ (Figure 4.5, lower row,).

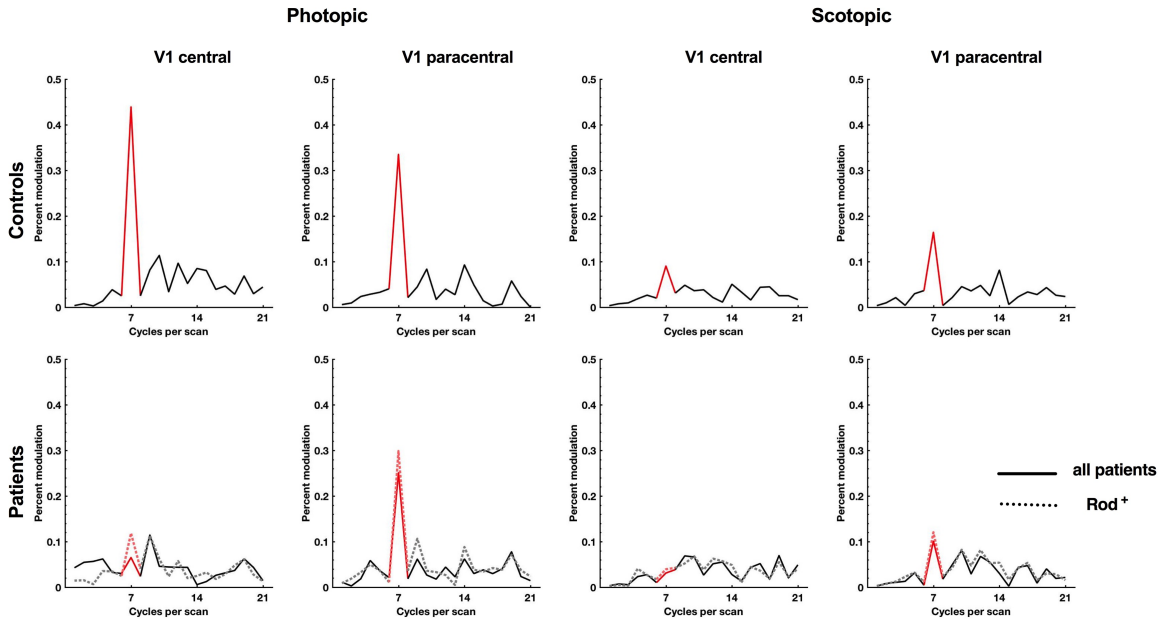

Figure 4.5 Response amplitudes for the foveal and paracentral proportion of primary visual cortex under two luminance levels. Plotted are response amplitudes (% signal change) as a function of temporal frequencies, centred around the stimulus frequency (7 cycles/scan, depicted in red). Top row: Response amplitude of control participants in foveal and paracentral proportion of V1 under two luminance levels; Bottom row: Single cycle modulation of all achromats for each ROI per luminance level. Overlaid (dotted line) on each graph is the response amplitude for rod monochormats with normal rod function; n(photopic/scotopic)^{Control} = 18/15; n(photopic/scotopic)^{Patient} = 15/12;

4.5.3 Phase estimates at the stimulus frequency

Baseler at al. (2002) showed that regions of cortex that represented central locations in controls responded to more peripheral visual field locations in patients. This should result in a phase shift for patients compared to controls, most likely in ROI^{central}. Figure 4.6 depicts the individual level, where subject specific phase and amplitude values at the stimulus frequency are overlaid on a polar grid for each ROI and condition. The mean time series was derived for each participant under each condition from the respective ROI to calculate the phase and amplitude at the stimulus frequency (7 cycles/scan) using a FFT. The derived values were plotted on a polar grid, were theta represents the phase and rho represents the amplitude of voxels within the respective ROI for a participant. For each subplot we superimposed

the mean vector in green. In all patient related polar plots achromats with atypical rod function (Rod^{-}) are denoted in red.

Controls exhibit responses that are, as predicted, almost perfectly out of phase in the two ROIs under both luminance conditions (Figure 4.6, upper row). For patients responses within $ROI^{paracentral}$ were clustered on the left hand side of the plot, similar to the responses of the controls, and the mean phase was again similar to that found in controls. The patients responses within $ROI^{central}$ were more mixed (Figure 4.6, lower row): First, the overall reduction in the amplitude of patient responses; second, the distribution of phases looks close to random under both luminance conditions;

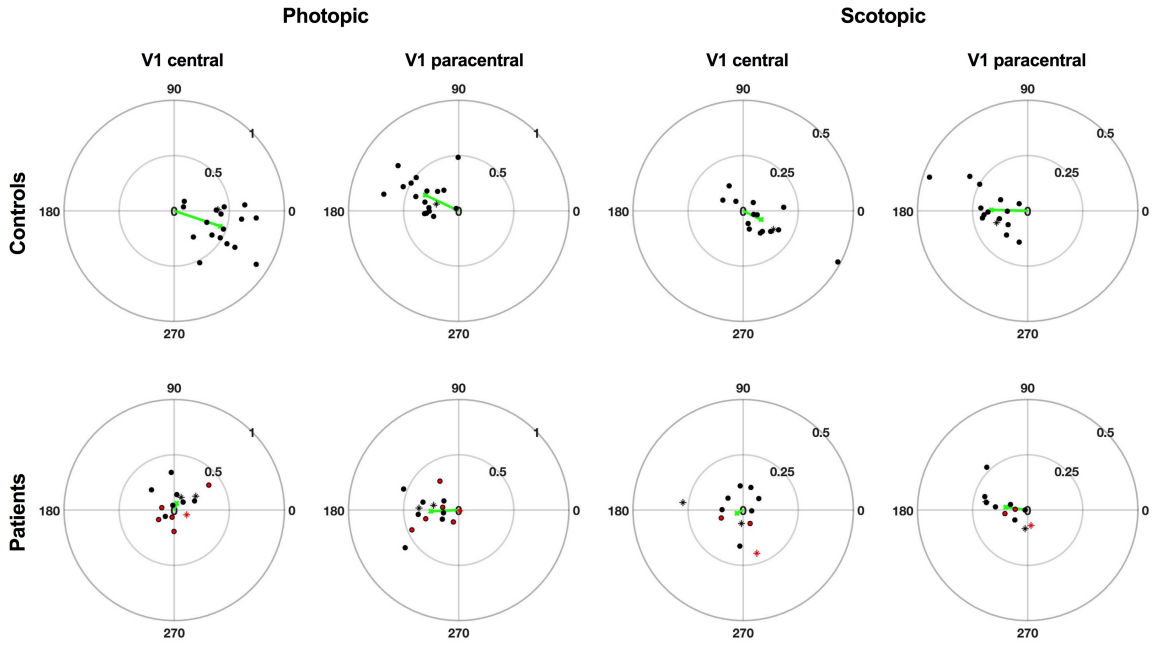

Figure 4.6 Polar plot for foveal and paracentral proportion of primary visual cortex under two luminance levels. Plotted are response amplitudes (% signal change, rho) and phase (theta) for each participant at the stimulus frequency. For each graph the averaged phase/ amplitude is represented as green vector. Top row: Response amplitude and phase of each control participants in foveal and paracentral proportion of V1 under two luminance levels; Bottom row: Response amplitude and phase for each ROI per luminance level. Black asterisk represents patient with typical while the red asterisk represent patient with atypical rod function. Asterisk represent participants depicted in the respective mesh images; $n(photopic/scotopic)^{Control} = 18/15$; $n(photopic/scotopic)^{Patient} = 15/12$;

third and notwithstanding this largely random distribution, some individual points indicate moderately large amplitude responses in the central representation with atypical phases, which could represent remapping; finally, the mean vector of the group responses is very small.

The analysis approach presented so far links to Baseler et al. (2002) and offered an initial overview of the data set. Our results indicate that remapping does not seem to be a general feature in this patient population as contrary to Baseler et al. (2002) all analysis streams indicate a lower responses in patients compared to controls in the region of interest that normally represents central visual field locations.

The main focus of this multicentre approach was to apply state of the art pRF mapping to further assess remapping in achromats and add new details to Baseler's study.

As indicated, two main measurements were extracted to assess remapping. First we examined the proportion of cortex of each ROI that exhibited significant responses in both cohorts. If remapping is a feature in patients, this should result in an increase in significant responses, especially noticeable under socotpic conditions in representations of the centre of the visual field. We then looked at the mean eccentricity of these significant responses. In line with Baseler et al (2002), if remapping were a feature in this patient population we would expect greater eccentricities in the foveal ROI. Figure 4.7 represents the pRF eccentricity estimates that are measured as a response to the presented bar stimuli for patients and controls under photopic and scotopic viewing conditions.

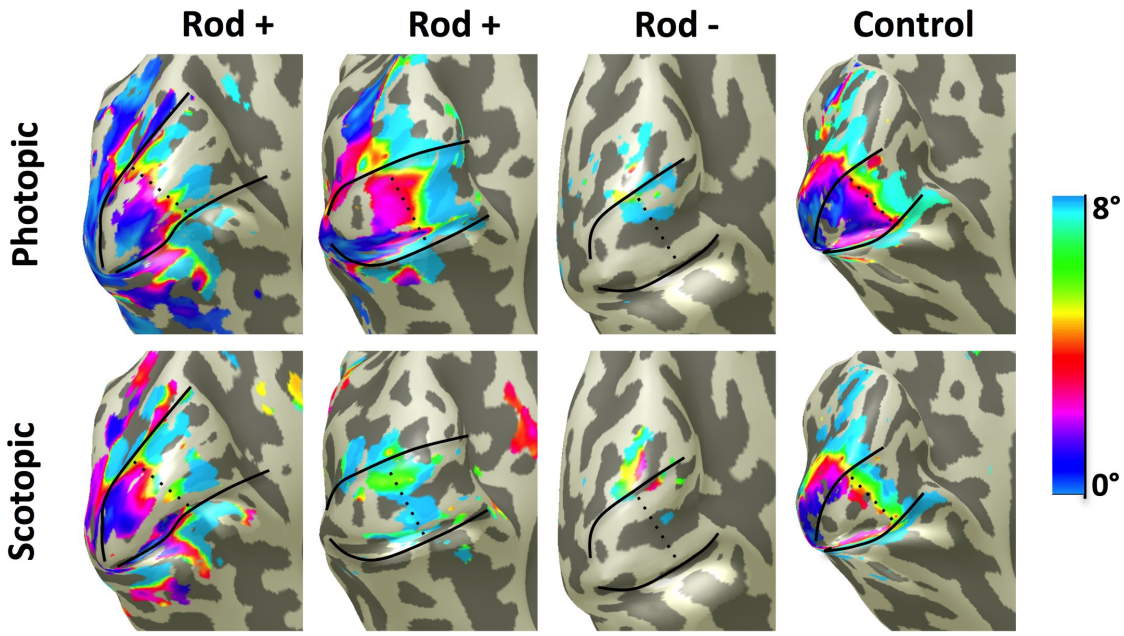

Figure 4.7 Eccentricity representation in primary visual cortex under different luminance levels derived via pRF mapping. All maps are projected onto the left hemisphere of a rendered 3D mesh; Rod$^+$ refers to patients with standard rod function while Rod$^-$ refers to patients with below threshold rod function; visual boundaries of V1 (central and paracentral representation) are overlaid and shown in black.

Similar to the phase encoded data estimates derived from the control exhibit a loss of response in very central representations when the light level shifts from photopic to scotopic. However, the more eccentric visual field representations of V1 exhibit reliable responses under both photopic and scotopic conditions. In the Rod$^+$ patient there is also a change in the map when luminance decreases from photopic to scotopic; there is a less complete map under the lower light level. Moreover, there appears to be less of V1 responding to visual stimuli in this patient than in the representative control. The patients with abnormal rod function (Rod$^-$) differ greatly from Rod$^+$ and control with significant activity in primary visual cortex being largely absent.

4.5.4 Proportion of cortex responding to visual stimulation

As these qualitative maps only depict exemplar participants for each group we further characterised the proportion of significant visual cortical responses in both participant groups in a quantitative manner.

To calculate the percentage of 'active' voxels per ROI and luminance condition the number of voxels that exceeded 10% variance in each pRF model fit was determined per participant for each ROI and divided by the total ROI voxel count.

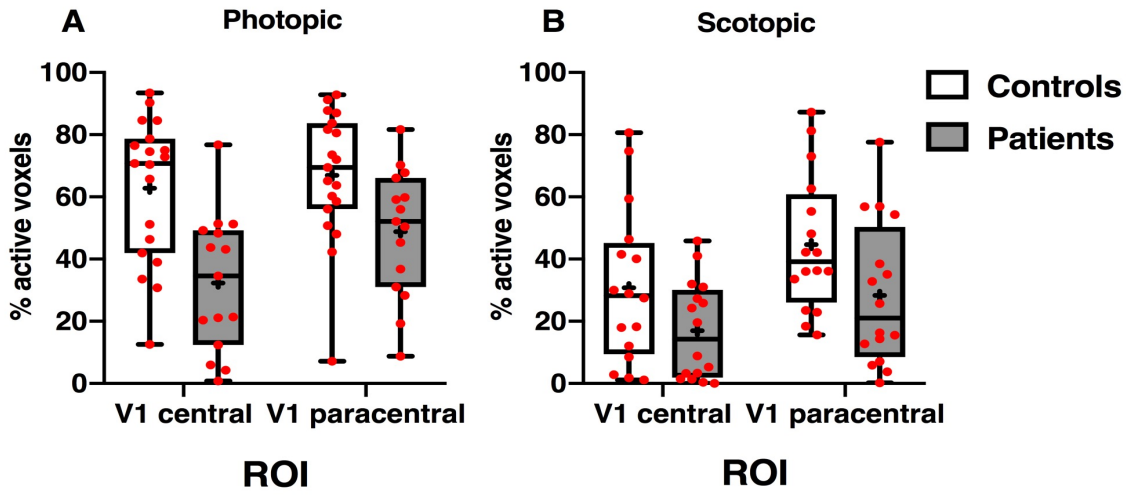

Figure 4.8 Percentage of active voxels in the central and paracentral proportion of primary visual cortex under two luminance conditions. Active proportions of V1 are determined by the number of voxels that show at least 10% variance explained in relation to the total number of voxels within the respective ROI. In A) we plotted the visual cortical activity for controls and patients under photopic luminance conditions while B) represents the percent of active cortex, derived under scotopic conditions. Whiskers represent min. and max. values, with mean percentage 'active' values denoted as '+'; individual data points are shown in red; $n(photopic/scotopic)^{Control}$ = 19/16; $n(photopic/scotopic)^{Patient}$ = 15/16;

This analysis stream was first applied to all patients to determine if the patient group in general showed signs of cortical remapping, which would be evidenced by a greater than normal percentage of V1 responding. Under photopic condition the control group exhibits a percentage of V1 responding that is consistent across both ROIs. However, the patient group showed a clear reduction in the percentage of V1

responding, although it is less pronounced in the paracentral ROI (Figure 4.8A). A two-way mixed ANOVA was applied to test for an effect of participant group and ROI on the dependent variable of cortical activation.

The test revealed a main effect for participant group ($F(1,32) = 14.68$, $p=.001$) and ROI ($F(1,32) = 6.864$, $p=.013$) but no significant interaction ROI* Group ($F(1,32)= 2.454$, $p=.127$). This indicates that patients exhibited overall a lower percentage of V1 responding compared to controls and that the percentage differed in general between foveal and parafoveal cortical representations. It was anticipated that controls would have a greater percentage of V1 responding in central representations given the cone driven regions there. However, the reduction overall for patients, which included the representation of paracentral regions was not anticipated. As under scotopic condition controls have no cone input both participant groups should exhibit similar cortical inputs, thus any signs of cortical remapping should be most pronounced under scotopic conditions. Figure 4.8B shows that under scotopic conditions the percentage of V1 responding is markedly reduced compared to the photopic condition for both groups and the patient group exhibited percentages of V1 responding in both ROIs that were lower still than controls. A two-way mixed ANOVA was again performed to test for an effect of participant group and ROI on the dependent variable of cortical activation. The test revealed a main effect for participant group ($F (1,30) = 4.415$, $p= .044$) and ROI ($F (1,30) = 21.064$, $p<. 0001$) but no significant ROI* Group interaction ($F (1,30)= .204$, $p= .655$).

Previous analysis streams already emphasised that cortical activation in Rod^- participants differs noticeably from Rod^+ patients, thus it is possible that these participants drive the reduction in the percentage of V1 responding in the patient group.

Consequently, we determined if a reduction in rod function was linked with a reduction in cortical activation level. Under photopic conditions patients with reduced rod function showed a profound reduction in percentage of V1 responding, evident in both ROIs (Figure 4.9A). A two-way, mixed ANOVA was applied and revealed a main effect of group ($F(1,13) = 16.50$, $p = .0013$) and ROI ($F(1,13) = 8.799$, $p = .0109$), while an interaction between group and ROI was not significant ($F(1,13) = .01414$, $p = .9072$). Under scotopic condition this difference in cortical responses between Rod^+ and Rod^- was even more prominent with a nearly complete absence of response in the ROD- group (Figure 4.9B). A two-way, mixed ANOVA revealed only main effects on percentage of V1 responding (Group: $F(1,14) = 12.09$, $p = .0037$; ROI = 8.629, $p = .0108$) and no significant interaction between these two factors ($F(1,14) = 1.295$, $p = .2742$).

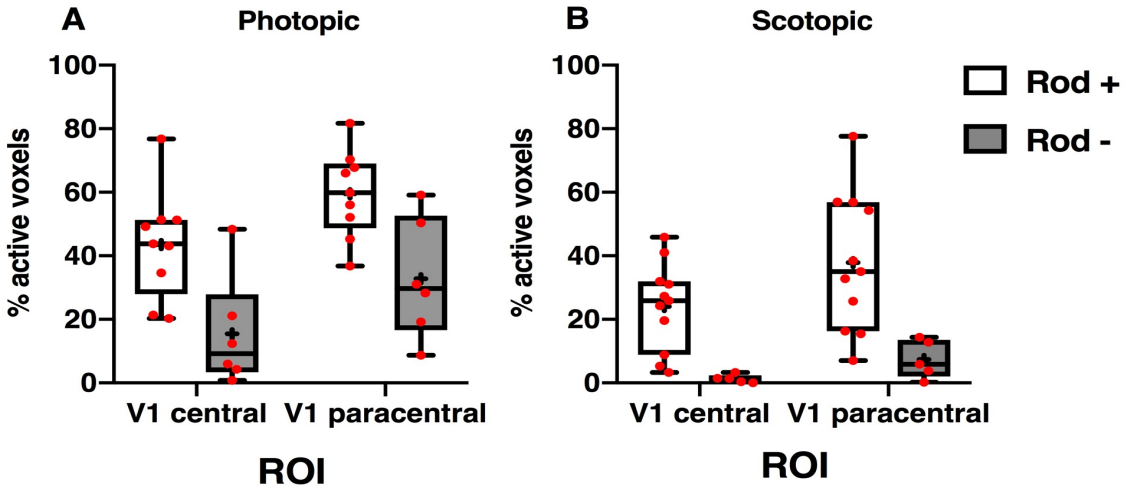

Figure 4.9 Percentage of active voxels in the central and paracentral proportion of primary visual cortex under two luminance conditions in patient subpopulations. Active proportions of V1 are determined by the number of voxels that show at least 10% variance explained in relation to the total number of voxels within the respective ROI. In A) we plotted the visual cortical activity for rod achormats with typical rod and atypical rod function, derived under photopic conditions while B) represents the percentage of active cortex, derived under scotopic conditions. Whiskers represent min. and max. values, with mean percentage 'active' values denoted as '+'; individual data points are shown in red**;** $n(photopic/scotopic)^{Rod+} = 9/11$; $n(photopic/scotopic)^{Rod-} = 6/5$;

This result confirmed that reduced rod function resulted in significantly less cortical activation, thus for subsequent analysis only patients with typical rod function were included to avoid any bias introduced by the reduced rod function phenotype.

We applied the same analysis approach for data obtained under photopic condition and revealed a similar response pattern to previously but with a less pronounced difference between control and the patient (Rod^{+}) group (Figure 4.10A). A two-way, mixed ANOVA was applied to test the effects of ROI and GROUP on the dependent variable of percentage of V1 responding. Accordingly, the ANOVA revealed a trend effect of GROUP ($F(1, 26) = 3.963$, $p = .0571$) but a significant main effect of ROI ($F(1, 26) = 4.652$, $p = .0404$). The interaction between the two factors still failed to reach significance ($F(1, 26) = 1.605$, $p = .2165$). Under scotopic conditions the percentage of V1 responding to only rod driven signals is quite comparable between groups while responses in $ROI^{central}$ were smaller compared to the $ROI^{paracentral}$ (Figure 4.10B). This was reflected by the ANOVA results as no main effect of GROUP was observed ($F(1, 25) = .7513$, $p = .3943$), while the main effect of ROI was highly significant ($F(1, 25) = 18.00$, $p = .0003$). The interaction between the two factors was again not significant ($F(1, 25) = .0004$, $p = .9907$). It appears therefore that the group difference that approached significance under photopic conditions disappear under scotopic conditions. At the same time however there is no evidence for increased representations of rod driven signals in patients compared to controls, a feature that if present would have indicated remapping of visual cortex.

Overall, we found that the percentage of V1 responding is affected by the light level; values are reduced under low luminance conditions. This effect was largely unanticipated and previous work relied on the effect being absent as the stimuli presented by Baseler at al. (2002) were at different light levels for the patients and

controls respectively. The authors took the precaution to isolate the rod signals using silent substitution techniques at a relatively high luminance for patients, but in controls necessarily presented stimuli at lower, scotopic light levels. We were intrigued therefore to compare the responses from patients obtained under photopic conditions with control data obtained under scotopic conditions as this more closely followed the previous study (Figure 4.10C). Now, compared to controls the patients showed an increase in percentage of V1 responding compared to controls, which would be indicative for cortical remapping.

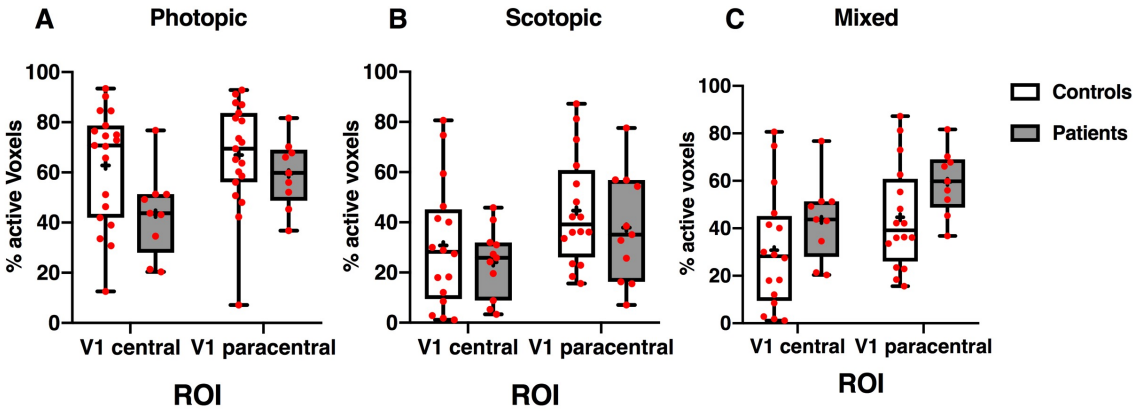

Figure 4.10 Percentage of active voxels in the central and paracentral proportion of primary visual cortex. Percentages of V1 are determined by the number of voxels that show at least 10% variance explained in relation to the total number of voxels within the respective ROI. In A) we plotted the visual cortical activity for rod monochormats with typical rod rod function and controls, both derived under photopic conditions while B) represents the percentage of V1 responding, derived under scotopic conditions for both, Rod+ and controls. In C) luminance conditions are mixed and the percentage of V1 responding of controls under scotopic conditions is contrasted with the percentage of V1 responding within the respective ROI of Rod+ patients derived under photopic conditions; Whiskers represent min. and max. values, with mean percentage 'active' values denoted as '+'; individual data points are shown in red**;** n(photopic/scotopic)^{Control} = 19/16; n(photopic/scotopic)^{Patient} = 9/11;

However, the two-way, mixed ANOVA only revealed an effect of ROI ($F(1, 23) = 14.92$, $p = .0008$) but did not detect a main effect of GROUP ($F(1, 23) = 3.080$, $p = .0926$) and no interaction between these two factors ($F(1, 23) = .0730$, $p = .7894$). So

while the difference is now in the direction consistent with remapping, the difference between groups is not significant.

4.5.5 Eccentricity of responses in visual cortex

If remapping is a feature in this patient sample this should result in the larger eccentricity values in the central visual field representations in patients compared to controls. To test this, we extracted the mean eccentricity values of the significant, above threshold responses (> 10% variance explained), for both ROIs under each luminance condition.

As before, we only included patients with typical rod function (Rod+) and Figure 4.11A highlights that under photopic conditions patients seem exhibit greater eccentricity values compared to controls at the central visual field representation, while the eccentricity differences in the paracentral ROI are less pronounced.

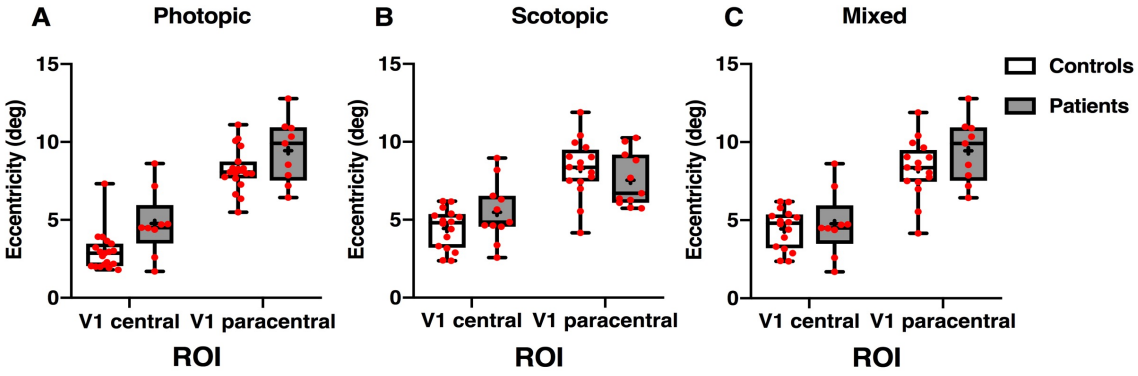

Figure 4.11 Mean eccentricity in the central and paracentral proportion of primary visual cortex under different luminance conditions. Plotted is the mean eccentricity of voxels that show at least 10% variance explained within the respective ROI. In A) mean eccentricity is plotted for achromats with typical rod rod function and controls, both derived under photopic conditions while B) represents the mean eccentricity, derived under scotopic conditions. In C) luminance conditions are mixed and the mean eccentricity in controls under scotopic conditions is contrasted with mean eccentricity of rod + patients derived under photopic conditions within the respective ROI; Whiskers represent min. and max. values, with mean eccentricity values denoted as '+'; individual data points are shown in red; $n(photopic/scotopic)^{Control} = 19/16$; $n(photopic/scotopic)^{Patient} = 9/11$;

The ANOVA revealed only a main effects of ROI ($F(1, 26) = 174.7$, $p<0.0001$) and GROUP $F(1, 26) = 8.398$, $p= .0075$) while the interaction between ROI and GROUP was not significant ($F(1, 26) = .5912$, $p= .4489$).

Similar results were found under scotopic viewing conditions for the central visual field representations where patients exhibited greater eccentricity values. In contrast, within the cortical representation of more paracentral visual field representations eccentricity values in controls were slightly increased compared to patients (Figure 4.11B). The two-way, mixed ANOVA revealed a main effect of ROI ($F(1, 25) = 54.89$, $p<0.0001$) but no main effect of group ($F(1, 25) = .07070$, $p=0.7925$). Importantly, the interaction between the two factors is significant ($F(1, 25) = 5.112$, $p=.0327$). An independent samples t-tests did not reveal significant group differences at either region of interest, indicating that the interaction is driven by sign differences across regions of interest (central representation: $t = 1.700$, $df = 25$, $p = .101$, paracentral representation: $t = -1.080$, $df = 25$, $p = .291$).

We also explored the compared results for patients under photopic and the controls under scotopic conditions. More subtle group differences were found: For the central representation the eccentricity values exhibited only a slight increase in the patient group, which were slightly more pronounced within the paracentral visual field representation (Figure 4.11C). This was reflected by the statistical analysis as well as the ANOVA revealed only a main effect of ROI ($F(1, 23) = 97.34$, $p<0.0001$) but no main effect of GROUP ($F(1, 23) = 1.495$, $p= .2338$) and no interaction between these two factors ($F(1, 23) = .8758$, $p= .3591$).

4.5.6 pRF size of responses in visual cortex

As Baseler et al. (2002) used conventional phase-encoded retinotopy, population receptive field size was not assessed in achromats. Here, we have the opportunity to test whether or not there were changes in pRF size given the approach we have now taken. In the case of remapping one might expect slightly smaller population receptive fields as animal studies showed that previously enlarged and shifted pRFs seem to reduce their size again upon completion of reorganisation in the visual cortex (Gilbert & Wiesel, 1992). To test this, mean pRF size values were extracted for each participant and plotted for both ROIs under the respective luminance condition (Figure 4.12).

Under the photopic condition pRF size was generally higher in paracentral compared to central representations of V1. Patients exhibited overall greater pRF sizes than controls in both ROIs (Figure 4.12A). This is also reflected in a main effect of GROUP ($F(1,26) = 44.58$, $p < .0001$) and a main effect of ROI ($F(1,26) = 33.34$, $p < .0001$) while an interaction between these two factors was not evident ($F(1,26) = .1480$, $p = .7036$

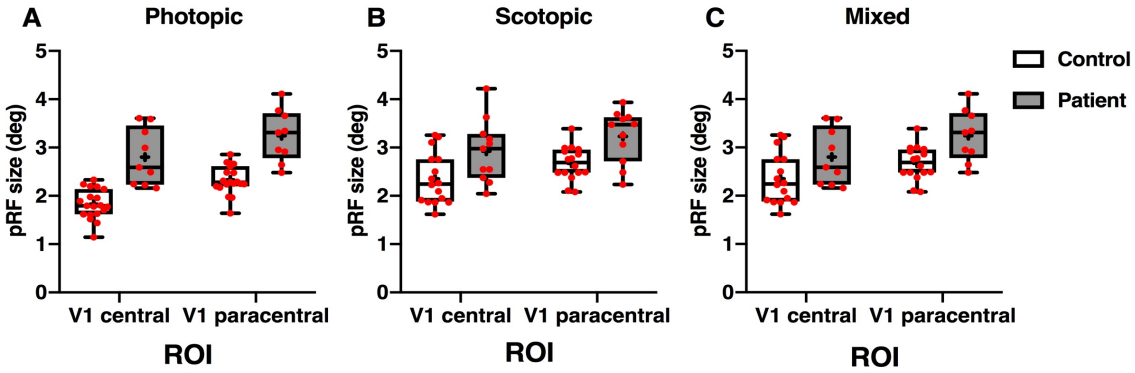

Figure 4.12 Mean pRF size in the central and paracentral proportion of primary visual cortex in different luminance conditions. Plotted is the mean pRF size of voxels that show at least 10% variance explained within the respective ROI. In A) mean pRF size is plotted for achromats with typical rod rod function and controls, both derived under photopic conditions while B) represents the mean pRF size derived under scotopic conditions. In C) luminance conditions are mixed and the mean pRF size in controls under scotopic conditions is contrasted with mean eccentricity of rod + patients derived under photopic conditions within the respective ROI; Whiskers represent min. and max. values, with mean pRF size values denoted as '+'; individual data points are shown in red; $n(photopic/scotopic)^{Control} = 19/16$; $n(photopic/scotopic)^{Patient} = 9/11$;

Similarly, under the scotopic condition (Figure 4.12B), difference in pRF size between patients and controls were also present, although less pronounced ($F(1,25) = 11.25$, $p = 0.0025$). Also, paracentral proportions of visual cortex still showed larger pRFs compared to central proportions, reflected in a main effect of ROI ($F(1,25) = 8.388$, $p = 0.0077$). No interactions between these two factors were evident ($F(1,25) = 0.003742$, $p = 0.9517$).

In line with the preceding results larger population receptive fields were also found in patients compared to controls, when we considered control data obtained under scotopic condition and patient pRF size estimates derived under photopic conditions (Figure 4.12C). While again a main effect of GROUP ($F(1, 23) = 8.452$, $p=0.0079$) and ROI ($F(1, 23) = 12.39$, $p=0.0018$) could be observed, interactions between these two factors were not significant ($F(1, 23) = 0.2942$, $p=0.5927$). It appears therefore that instead of a refinement of pRF to smaller sizes in patients, there is an increase in size.

4.6 Discussion

4.6.1 General overview

The aim of experiments presented in this chapter was to revisit the pioneering study by Baseler et al. (2002) and examine the reported reorganisation in achromats in a larger and thus more representative cohort with state of the art imaging methods. Recruitment efforts were shared across different scanner sites (University of York, UK; Otto-van-Guericke University, Magdeburg, DE; Haddassah medical Centre, Jerusalem, IL) and resulted in a total of 18 patients and 19 controls. Diagnoses for all patients were genetically confirmed, with equal distribution of the two main involved disease-causing genes (Table 4.2). While the characterisation of visual cortical estimates in a representative cohort was the main aim of this study, this cohort also included patients with atypical rod function. Thus, we first discuss how their response profiles compare with patients that show typical rod function, before we focus on changes in cortical organisation and the relation to cortical remapping in patients with typical rod function

4.6.2 Atypical rod function in achromats results in reduced cortical responses

The cohort of rod achromats we recruited included those with atypical rod function (Table 4.2), a subpopulation that is characterised by reduced rod ERGs (Khan et al., 2007; J. Maguire et al., 2018; Moskowitz et al., 2009; Wang et al., 2012). If not only cone but also rod signalling is impaired this will have a pronounced effect on cortical responses and is likely to have influenced the measures we took. The responses to

expanding ring stimuli indicated that this might be the case. Further, when the proportion of ROIs that responded significantly were compared between patient subgroups, a significant reduction in response level in the ROD^- cohort compared to ROD^+ patients could be observed. Our data therefore reveal that impoverished rod function does indeed affect responses in visual cortex. As a consequence it is important to exclude such participants from assessment of remapping of visual cortex because no control group exists. Forthwith therefore we refer only to results comparing patients with typical rod function with controls.

4.6.3 No increases in primary visual cortex responses in achromats

According to our hypothesis, if remapping is a feature in ACHM, a greater proportion of primary visual cortex should be responsive under scotopic conditions in patients compared to controls. Following the results of Baseler et al. (2002), it was also predicted that this effect would be most evident in the cortical representation of the central visual field. The first approach, that largely replicated the design used by Baseler et al. (2002), showed no evidence of increased response patterns in primary visual cortex in patients with typical rod function, even at central visual field representations under scotopic conditions.

These cortical responses were further investigated using a more up-to-date pRF mapping approach, which should exhibit an increased sensitivity, as a greater volume of pRF data was acquired for each participant. But, even with a more sensitive approach, the same response pattern was observed as patients showed again no increased responses within central visual field representations under scotopic conditions when compared to controls. This lead to the interim conclusion, that

cortical remapping, as found by Baseler et al. (2002), does not seem to be a general feature of ACHM once a larger cohort of patients is examined.

4.6.4 Absence of cone function does not result in a remapping of cortical visual field eccentricity estimates

Estimates derived from the pRF data allows for further exploration of remapping. Specifically, Baseler et al. (2002) showed a shift in phase for foveal visual field representations in achromats, thus we expected to see a shift in eccentricity estimates, which should again be most pronounced at central visual field representations (Baseler et al., 2002). Again, the scotopic condition is the most meaningful comparison as cortical signals reflect similar, rod-initiated input to primary visual cortex in both participant cohorts. Contrary to our hypothesis, patients exhibited no significant shift in eccentricity. An additional comparison of eccentricity representations obtained under photopic conditions in patients and scotopic conditions in control – a feature of the Baseler et al. (2002) study – revealed only a trend for greater eccentricities in patients at central visual field representations. Importantly, the phase-encoded data highlighted some participants that showed distinct response amplitudes, paired with a phase shift at foveal representations that seemed quite comparable to the phase shift reported by Baseler et al (2002). Thus, while an increase in eccentricity, indicative for remapping, does not hold on a group level, the possibility persists that some participants still exhibit signs of reorganisation which might drive the trend to greater eccentricities observed in the pRF data.

It is possible though, that this trend to increased eccentricity estimates in patients could simply be explained by fixation instability as nystagmus is a characteristic trait commonly occurring in patients with ACHM (Aboshiha et al., 2016; Haegerstrom-Portnoy et al., 1996; Reeves, 2003). This possibility can be ruled out though, as first of all, precautions were undertaken to minimise nystagmus and secondly, while nystagmus would add noise to the fitting procedure, it was already shown that this has no influence on eccentricity estimates (Baseler et al., 2002; Levin et al., 2010).

It is worth noting, that the pRF eccentricity data also yielded a predicted result as eccentricity estimates under photopic conditions differed significantly between groups, especially noticeable at central visual field representations. This difference reflects the influence of foveal cones in control participants, which are absent in patients, thus highlights the capability of the pRF method to register differences in the cortical mapping of eccentricity.

4.6.5 PRF size estimates enlarged in patients

Another advantage of pRF mapping compared to conventional phase encoded retinotopy is that it also allows the estimation of the pRF size, which so far has not been assessed in rod achromats. Generally, pRF size could be influenced by many factors: One might predict smaller pRFs as in rod achromats a greater amount of cortex is now available for rod input. Also, animal studies showed that previously enlarged and shifted pRFs seem to reduce their size upon completion of reorganisation in the visual cortex (Gilbert & Wiesel, 1992). Controls showed an increase in pRF size under scotopic condition, notable for both ROIs. This is in line with our previous results (Chapter 3), and expected due to the difference in spatial summation between cone and rod pathway (Barlow, 1958; Hallett, 2003; Scholtes &

Bouman, 1977; Sharpe et al., 1993; Westheimer, 1965). However, contrary to the initial prediction rod achromats exhibit generally larger pRFs under both conditions. Importantly, size estimates are more or less constant across conditions, reflecting the absence of cone responses at both light levels in patients. More in line with our findings is a study in patients with homonymous visual field defects, that also indicated an increase in pRF size (Papanikolaou et al., 2014). They claimed that this might be related to a decreased inhibition of the area surrounding the scotoma (Eysel, 1999) or related to reorganisation of subcortical areas (Rose, Malis, Kruger, & Baker, 1960).

Any further interpretation of our pRF size changes has to be taken with precautions. Contrary to eccentricity estimates, nystagmus and the resulting fixation instability might indeed have lead to overestimated pRF size estimates (Haak, Langers, et al., 2014; Levin et al., 2010)

Interestingly, an increased in pRF size in patients was already put forward as an alternative explanation for findings in Baseler et al. (2002) (Beyeler, Rokem, Boynton, & Fine, 2017). If this increase is indeed real and not a side effect of external factors, this might lead to foveal activation in patients under brighter light conditions, as more pRFs with a broad spread would be active. Under scotopic condition though, signal-to-noise ratio (SNR) decreases, fewer voxels will reach the applied threshold and the foveal responses, interpreted as remapping, disappear.

4.6.6 Possible explanations of discrepancies with initial patient study

A misregistration of the anatomical atlas (Benson et al., 2014) used for ROI definition might offer one possible explanation for the difference to Baseler et al. (2002), as this could mask remapping in patients. This possibility is rather unlikely as the phase-

encoded data showed clear stimulus related responses within the respective ROIs. Also, we found overall the predicted change in eccentricity with location in V1; the more anterior ROI represented more eccentric visual field locations and a clear effect of ROI on pRF characteristics was evident. More importantly, this anatomical atlas has been successfully used to characterise anatomical and functional differences in patient related studies (Aguirre et al., 2017; Cideciyan et al., 2008; Winawer & Parvizi, 2016) .

An important difference to Baseler et al. (2002) might be better suited to explain the discrepancy between the two studies. As outlined already earlier, Baseler et al. (2002) compared visual responses from patients derived under brighter luminance levels than controls. Our results show that the reduction in luminance levels can lead to a distinct decrease in signal amplitude in controls when shifting from photopic to scotopic even under two different scotopic luminances (see Chapter 3). Our patient responses seem to exhibit generally a weaker signal at scotopic luminance levels indicating a lowered SNR in achromats. Subsequently, stimulus related signals might now be masked by noise and cannot be easily detected with fMRI. Response modulation derived from ring stimulus corroborates this possibility, as under scotopic condition even the quite robust signal from central visual field representations is nearly absent in patients. Further, also robust responses as revealed by the pRF analysis were markedly reduced in achromats, noticeable at both ROIs.

Importantly, once we contrasted cortical activation from patients derived from the photopic luminance condition with scotopic driven responses in controls, we could observe the trend to increased cortical responses in patients, a feature that is more

comparable to the results of Baseler et al. (2002). This means that that luminance differences may indeed have had a potential influence on previously reported results. Even though the usage of mixed luminance levels offers an explanation for the discrepancy between the two studies, it emphasises that the underlying cause for responses in patients at central visual field representations is more likely related to differences in SNR than cortical remapping. Moreover, subsequent comparison of other pRF characteristics between different luminance levels lead to less pronounced differences between both participant groups. In addition to differences in SNR levels this might be related to the presence of the cortical equivalents of the rod scotoma, which here will influence control estimates more severely (Barton & Brewer, 2015; Baseler et al., 2011; Haak et al., 2012), thus reduce any differences between participant groups even further.

4.6.7. Conclusion and outlook

Data presented within this multicentre study provides little evidence for large-scale reorganisation of visual cortex in achromats. Overall patients show no increased cortical responses at central visual field representations under scotopic conditions. This discrepancy to Baseler et al. (2002) seems mainly related to the fact that patients were tested at higher luminance levels than controls, thus increased responses might rather reflect a difference in SNR than cortical remapping.

Moreover, their recruited participants were described as high functioning achromats, which indicates that their chosen subjects might not have reflected the general patient population to begin with.

Thus, our finding in a representative cohort of achromats is likely of more clinical value as it highlights that cortical remapping will not have to be counteracted to

optimise currently on-going vision restoration approaches. Equally importantly, this study indicates that patients that present with abnormal rod function have incomplete cortical representations, which emphasises the necessity to research this subpopulation further to guarantee an efficient treatment regime.

Ultimately, this study cannot fully exclude the possibility that some high functioning individuals indeed exhibit some form of reorganisation, which might just be reflected in a simple peripheral shift in eccentricity values around the LPZ. On the whole, this study also underlines heterogeneity of the ACHM disease phenotype (Hirji, Aboshiha, et al., 2018; Remmer et al., 2015; Sundaram et al., 2014) which elucidates the importance for clinical settings to combination state of the art clinical assessment with fMRI. This would not only offer additional objective information to evaluate patients but also help to increase the efficacy of therapeutic interventions (Ritter et al., 2019; Silson, Aleman, et al., 2018; Smirnakis, 2016).

Chapter 5

Characterisation of anatomical properties in primary visual cortex in congenital photoreceptor abnormalities using a surface based approach.

5.1 Abstract

While rod achromats congenitally lack cone function a pioneering study by Baseler et al. (2002) showed that the cortical area representing cone-only input is still responsive, demonstrating evidence of functional reorganisation. To investigate organisation of visual cortex further, we performed a multi-centre study utilising high resolution T1-weighted scans from the currently largest cohort of rod achromats (n = 16) and compared cortical thickness, surface area and grey matter volume in a central and paracentral representation of primary visual cortex to a broad baseline control data set (n = 42) using surface-based morphometry. We found a general reduction in surface area in both regions of interest (ROIs) in the patient cohort, while grey matter volume was only reduced in paracentral visual field representation. In contrast, a thickening of the cortex within the central visual field representation was detected. To further detail the affected cortical regions, the central ROI was subdivided to represent the foveal area encompassing the cortical equivalent of the rod scomotma (0-2 degrees) and the parafoveal area (2-4 degrees). While area reduction was observed in achromats in both sub divisions, thickening of the cortex was only observed within the most central representation. These results are in

accordance with other studies and indicate that changes to brain integrity in congenitally blind are quite comparable, in terms of a thickening of cortex resulting from a reduction in developmental pruning, irrespective of the underlying vision loss. Further, these changes indicate that there may be an optimum window for gene augmentation treatment.

5.2 Introduction

The aim of this empirical chapter is to utilise high-resolution T1-weighted images, collected as part of a large data set, and apply surface-based morphology to systematically assess structural cortical changes in achromatopsia (ACHM), a congenital photoreceptor abnormality. The use of functional magnetic resonance imaging (fMRI) already helped to determine the effects of this congenital vision loss on the functional organisation of visual cortex. A pioneering study in a small sample of achromats reported functional reorganisation in the cortical region that normally represents cone input alone (Baseler et al., 2002). In contrast, the proceeding chapter applied state of the art population receptive field (pRF) mapping (Dumoulin & Wandell, 2008) in a larger, thus more representative cohort and could not replicate these findings. While the current clinical therapeutic approaches would generally benefit from this novel finding, the absence of remapping could be accompanied by cortical atrophy in the deafferented structures as has been found in those with acquired visual loss (Boucard et al., 2009; Hernowo et al., 2014; Plank et al., 2011). Cortical changes may also be present in terms of a thickening within the representation of the scotoma as has been found in other congenital retinal diseases (Aguirre et al., 2017, 2016; Bridge et al., 2009; J. Jiang et al., 2009; Park et al., 2009).

This empirical chapter therefore tries to systemically analyse structural changes in primary visual cortex, which will not only add additional, objective information useful for clinical evaluation in this patient population but also inform the current literature how a defined congenital visual field loss affects anatomical properties.

The present chapter will first summarise current findings of structural changes in visual cortex as seen in congenital disorders and outline how such changes might affect current available treatment options before highlighting the necessity for a systematic assessment of cortical integrity in ACHM.

Over the past decades, the usage of MRI has enabled researchers to examine the integrity of cortical structures in blindness and to characterise occurring changes in more detail. This is important as advances in current visual rehabilitation regimes rely on the brain's ability to receive and interpret restored signals where any changes to the underlying morphology could negatively impact those efforts. Initially, early structural studies used mainly T1-weighted images to measure the overall extend of certain brain structures but technological advances over the last decades have improved signal contrast and spatial resolution, allowing for more refined assessments of cortical structure (Brown et al., 2016; Prins, Hanekamp, & Cornelissen, 2016).

Postgeniculate structural differences, often localised at the pericalcarine sulcus, are frequently reported in congenital visual disorders like congenital anopthalmia, congenital glaucoma or retinitis pigmentosa (Bridge, Cowey, Ragge, & Watkins, 2009a; Jiang et al., 2009; Park et al., 2009). Several voxel-based morphometry (VBM) studies highlighted a reduction in grey matter volume but due to the limited specificity of this method in the highly convoluted early visual cortex it could not be

determined if the volumetric reduction is driven by local changes in surface area or cortical thickness (Noppeney, Friston, Ashburner, Frackowiak, & Price, 2005; Pan et al., 2007; Park et al., 2009; Ptito, Schneider, Paulson, & Kupers, 2008). Further studies in congenitally blind applied a surface-based approach and linked the volumetric reduction to a decrease in surface area (Aguirre et al., 2016; J. Jiang et al., 2009; Park et al., 2009). Changes in cortical volume and surface area were partially explained by the lack of use of early visual cortex in early blind (J. Jiang et al., 2009; Park et al., 2009; Ptito et al., 2008). However, the lack of use of cortex may not fully explain the atrophy seen in congenital blind as for example, no significant correlation was shown between level of surface decrease and disease duration (Park et al., 2009).

An independent finding is an increase in cortical thickness, as reported for Leber congenital amaurosis (Aguirre et al., 2017), congenital anophthalmia (Bridge et al., 2009), Leber's hereditary optic neuropathy (d'Almeida, Mateus, Reis, Grazina, & Castelo-Branco, 2013) but also in cross sectional studies including participants with several forms of congenital blindness (Aguirre et al., 2016; Anurova, Renier, Volder, Carlson, & Rauschecker, 2015; J. Jiang et al., 2009; Park et al., 2009).

The discrepancy between thickening of cortical areas accompanied by a reduction in surface area and/or volume was generally attributed to different developmental trajectories of horizontal and vertical cortical properties (Kelly, Desimone, Gallie, & Steeves, 2015; Park et al., 2009; Rakic, 1995; Wierenga, Langen, Oranje, & Durston, 2014).

In this respect, increased cortical thickness might be related to aberrant cortical maturation, where synaptic pruning, a process to abolish weaker cortical connections, is halted due to the missing sensory input (Aguirre et al., 2017; Bourgeois, Jastreboff, & Rakic, 1989; Guerreiro, Erfort, Henssler, Putzar, & Röder,

2015; Park et al., 2009; Stryker & Harris, 1986). Several studies showed that in congenitally blind these cortical regions with increased thickness quite frequently compute input from other sensory modalities, commonly referred to as cross-modal plasticity (Anurova et al., 2015; Bavelier & Neville, 2002; Bedny, Pascual-Leone, Dodell-Feder, Fedorenko, & Saxe, 2011; Guerreiro et al., 2015; Sadato et al., 2002, 1996).

These quite consistent changes in cortical morphology might have manifold implications for current clinical vision restoration approaches. While cortical atrophy is not proven, the reduction in surface area and cortical volume could indicate some form of degenerative mechanisms which might limit vision restoration approaches (Lemos, Pereira, & Castelo-Branco, 2016; Prins, Hanekamp, et al., 2016).

Findings in blind born, cataract-reversal patients emphasises the importance of early visual input as increased cortical thickness was still measurable after surgery and more importantly, negatively correlated with visual task performance. In contrast, auditory task performance resulted in a positive correlation. Thus, while the brain seems capable to compensate for visual impairment by making use of still existing and not erased thalamo-cortical or cortico-cortical connections, the thickening of the cortex seems to have limiting effects on sight recovery procedures (Guerreiro et al., 2015). While cortical thickening of early visual cortex is observed in patients with Leber congenital amaurosis (LCA), several reports highlighted signs of recovery after gene augmentation interventions in these patients (Ashtari et al., 2011; Bennett et al., 2016; Cideciyan et al., 2008, 2013; Cideciyan & Jacobson, 2019). Thus, while an increase in cortical thickness might potentially limit the treatment efficacy it seems to be not per se contradictory for successful therapeutic interventions and other factors,

like the integrity of post retinal pathways, might also play a crucial role (Aguirre et al., 2017).

ACHM, another inherited photoreceptor dysfunction leads to an even more refined visual loss as underlying mutations mainly affect cone photoreceptors (Haegerstrom-Portnoy et al., 1996; Remmer et al., 2015). Similar to LCA, gene augmentation therapies are currently being evaluated in several ongoing clinical trails (NCT03758404, NCT03001310, NCT03278873, NCT02935517, NCT02599922, NCT02610582). Beneficial factors for successful gene therapy in ACHM are the stationary phenotype (Hirji, Georgiou, et al., 2018) and the fact that previous reports of cortical reorganisation in this patient population have recently been called into question (see proceeding chapter).

5.3. Aims and hypothesis

Importantly, the integrity of cortical structure in ACHM has not yet been assessed so the possibility persist that structural changes similar to the ones seen in other congenital disorders, might still negatively impact on current therapeutic approaches and influence the window for optimum intervention.

Thus, the aim of this current chapter is to utilise high-resolution T1-weighted images collected as part of a multi centre study at three different scanner (University of York, UK; Otto-van-Guericke University, Magdeburg, DE; Haddassah medical Centre, Jerusalem, IL) and apply surface-based morphometry to detail potential differences in cortical microstructure in this patient population.

To increase comparability, a region-of-interest based analysis was applied, using the same ROIs as in the proceeding fMRI study, one representing the central proportions

of the visual field (0-4 degrees) and another representing the more paracentral visual field (> 4- 8 degrees) in primary visual cortex. Subsequently, we assessed differences in cortical thickness, grey matter volume and surface area between achromats and control participants.

1. In line with previous studies, we expect any potential differences to be most prominent for $ROI^{central}$ as it was shown that vision loss leads to cortical changes within the retinotopic representation of the scotoma (Boucard et al., 2009; Burge et al., 2016; Plank et al., 2011; Prins, Plank, et al., 2016)
2. We would expect to see a decrease in surface area, similar to findings in other congenital disorders (Aguirre et al., 2016; J. Jiang et al., 2009; Park et al., 2009).
3. Further, a reduction in grey matter volume is also expected for $ROI^{central}$ as volumetric changes are mainly driven by changes to surface area and reduction in cortical volume has been shown in several congenital visual disorders.
4. As cortical thickness is generally reported to increase in congenitally blind, we expect to see similar changes, again most pronounced in the retinotopic representation of the visual defect.
5. To detail changes in cortical thickness further, we subdivided $ROI^{central}$ into a foveal and parafoveal ROI, spanning 0-2 degrees and 2-4 degrees, respectively. If changes are indeed related to aberrant pruning processes, cortical thickening should be most prominent in the most central ROI that includes the representation of the rod scotoma. On the other hand, if cortical thickening were rather indicative for compensatory plasticity, we would expect an increase in thickness at $ROI^{parafovea}$.

5.3 Methods

5.3.1 Participants

Data used in this study were collected as part of a multicentre project at three scanner sites (University of York, UK; Otto-van-Guericke University, Magdeburg, DE; Haddassah medical Centre, Jerusalem, IL). High resolution structural scans from 42 participants (mean ± SD age, 30.29 ± 9.72; 19 males) with normal or corrected-to-normal vision and 16 achromats (mean ± SD age, 37.81 ± 11.43; 9 males) were utilised in this study. Experimental protocols received approval from the site-specific ethics committee and were in accordance with the Declaration of Helsinki.

Participant	Gender	Age	Site	Participant	Gender	Age	Site
C	m	33	M	C	f	26	Y
C	f	58	M	C	f	26	Y
C	m	25	J	C	m	35	Y
C	f	33	J	C	m	29	Y
C	m	19	J	C	f	23	Y
C	f	22	J	C	m	24	Y
C	f	24	J	C	f	30	Y
C	m	34	J	C	m	23	Y
C	f	27	J	C	f	19	Y
C	m	26	J	C	m	22	Y
C	m	29	J	C	f	53	M
C	f	29	J	C	f	35	M
C	f	24	J	C	m	27	M
C	f	32	J	P	f	42	M
C	f	46	J	P	m	42	M
C	f	30	J	P	f	53	M
C	f	22	J	P	m	16	M
C	f	57	J	P	m	28	J
C	f	23	J	P	f	51	Y
C	m	23	J	P	m	28	Y
C	m	50	J	P	f	27	M
C	m	43	J	P	m	34	Y
C	f	25	J	P	m	35	J
C	f	27	J	P	f	54	Y
C	m	26	J	P	m	51	M
C	m	25	J	P	f	40	Y
C	m	29	M	P	m	22	M
C	m	27	M	P	f	41	J
C	f	32	M	P	m	41	J

Table 5.1 Participant demographics. Overview table summarising participant type, scanner site, age and gender; (C = control, P = patient; Y = York, M = Magdeburg, J = Jerusalem; m = male, f = female);

5.3.2 Processes

5.3.2.1 Data acquisition

York

A single, high resolution, anatomical, T1 weighted scan (TR, 2500ms; TE, 2.26ms; TI, 900 ms; voxel size, 1×1×1mm^3 ; flip angle, 7°; matrix size, 256×256×176), using a 64 channel, surface head coil , was acquired on a SIEMENS MAGNETOME Prisma 3T scanner at the York Neuro Imaging Centre (YNiC).

Jerusalem

A single, high resolution, anatomical, T1 weighted scan (TR, 2300ms; TE, 1.5ms; TI, 900 ms; voxel size, 1×1×1mm^3; flip angle, 9°; matrix size, 256×256×160) using a 32-channel surface head coil, was acquired, on a SIEMENS MAGNETOM Skyra scanner at the Edmond & Lily Safra Center for Brain Sciences, Hebrew University of Jerusalem

Magdeburg

A single, high resolution, anatomical, T1 weighted scan (TR, 2600ms; TE, 4.46ms; TI, 1100 ms; voxel size, 0.9×0.9×0.9mm^3 ; flip angle, 7°; matrix size, 256×256×256), using a 64-channel surface head coil, was acquired, on a SIEMENS MAGNETOM Prisma scanner at the University Hospital, Magdeburg.

5.3.2.2 Data pre-processing

Surface based morphology analysis was performed using Freesurfer analysis suit, Version 6.0 (http://surfer.nmr.mgh.harvard.edu/). Cortical reconstruction and volumetric segmentation of the T1-weighted scans was automatically performed using the 'recon_all' script, described in more detail elsewhere (Dale et al., 1999; Bruce Fischl, Sereno, & Dale, 1999). In brief, steps involved in this process include the removal of non-brain tissue (Ségonne et al., 2004), automated Talairach transformation, intensity normalisation (Sled, Zijdenbos, & Evans, 1998), tessellation

of the grey/ white matter and pial boundary (grey/cerebrospinal fluid) including automated topology correction and surface deformation (Dale et al., 1999; Bruce Fischl, Sereno, & Dale, 1999; Ségonne, Pacheco, & Fischl, 2007). After cortical models were derived, the cortical surface was inflated and registered to a sphere (Bruce Fischl, Sereno, Tootell, & Dale, 1999) and the surface parcellated according to gyral and sulcal structures (Desikan et al., 2006; Bruce Fischl et al., 2004).

The final surface reconstruction was inspected for potential cortical segmentation errors and, when necessary, manually corrected using the FreeView Visualisation GUI. All manually corrected reconstructions were rerun ('autoreconall2') utilising the edited brainmask.mgz files.

5.3.2.3 Data analysis

A subsequent region-of-interest-based analysis was applied where we compared differences in three surface based measures between patients and their age matched controls: cortical thickness (mm), surface area (mm^2) and cortical volume (mm^3).

Cortical thickness detailed the shortest distance between each grey/white boundary vertex and the pial surface (white matter/cerebrospinal fluid boundary) and vice versa. The final value depicted the average of the two measured thickness value (B. Fischl & Dale, 2000). Surface area was measured by calculating the summed surface area of each triangle, the unit used to connect the cortical surface between each vertex. Cortical volume was computed as the volume of a truncated tetrahedron as described in Winkler et al. (2018).

ROIs used for this analysis stream were again derived utilising the anatomically defined retinotopy atlas (Benson et al., 2014) implemented in the python analysis tool box 'neurophythy' (Benson & Winawer, 2018)). This allowed us to analyse the

structural data set on a similar basis as the preceding functional study. The atlas created several freesurfer based maps (visual area, eccentricity, polar angle, pRF size), which were used to delineate two ROI labels for each participant. The created ROIs represented, in line with the preceding chapter, the central (0-4°) and paracentral proportions (4-8°) of V1. For further analysis the central proportion was subdivided in a foveal and a parafoveal ROI, spanning 0-2 degree and 2-4 degrees, respectively (Figure 5.1).

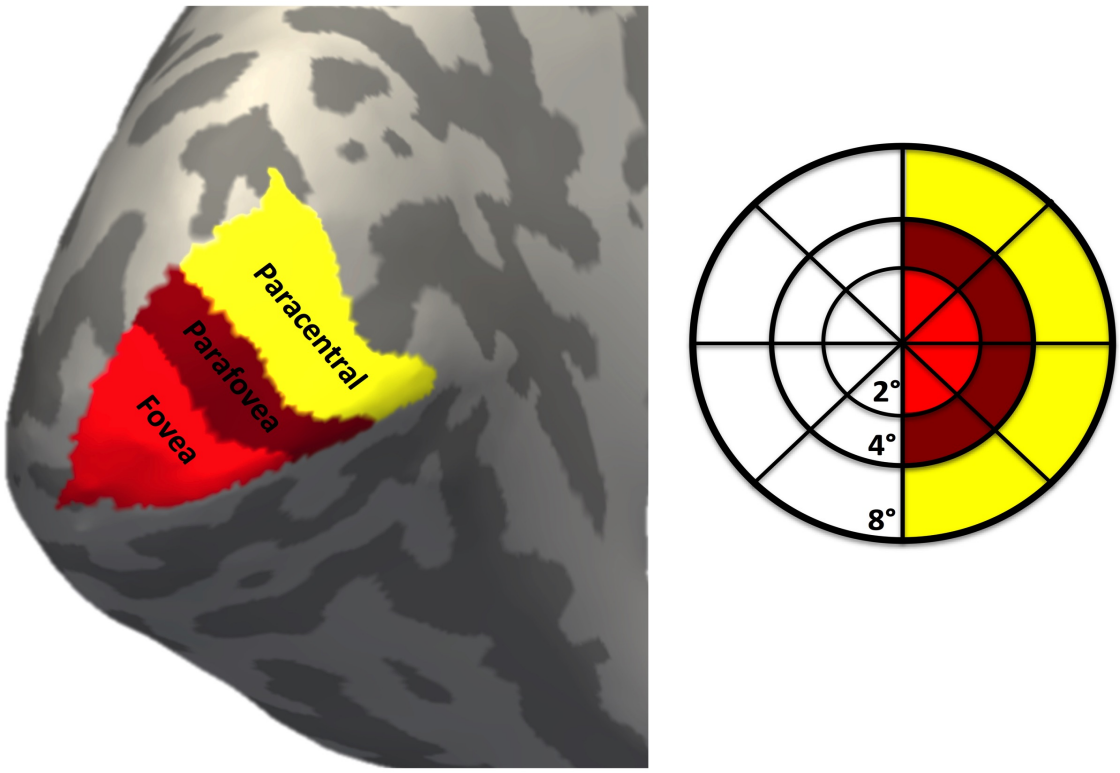

Figure 5.1 Delineation of visual areas. Representation of the left hemisphere of one participant, shown as inflated cortical surface in FreeView (6.0). ROIs derived from the retinotopy freesurfer template (Benson et al., 2014) overlaid on the surface as cortical labels. The V1central ROI refers to cortical areas representing the central 4 degrees of the visual field (red) while V1 paracentral refers to cortical areas representing paracentral areas (4-8 deg) of the visual field (yellow). The central ROI was further subdivided in a foveal and paravoveal ROI, spanning 0- 2 degrees and 2-4 degrees, respectively.

Extracted values were pooled for both hemispheres, where surface area and cortical volumes was simply summed for each participant. For cortical thickness, the values

were weighted by the respective surface area value and the overall cortical thickens value derived via following calculation:

ThicknessTotal = ((lh.thickness * lh.surfacearea) + (rh.thickness * rh.surfacearea))/ (lh.surfacearea + rh.surfaceare).

Equation 5.1 Equation for calculating pooled thickness values across both cortical hemispheres

5.3.2.4 Statistical analysis

A hierarchical linear regression was applied to predict the three outcome measures (cortical thickness, grey matter volume, surface area) in each of our four ROIs from participant group. To account for differences in gender, age and scanner site these variables were entered in the first step of the hierarchical linear regression model, while participant group (controls and patients) was added in the second analysis step. R^2 of the first applied model and ΔR^2 of the second model are reported alongside the F statistics, while coefficients for predictors in both models are detailed in the appendix. All analysis steps were performed in the IBM SPSS Statistics software package, version 25. Graphs were created using Prism version 8.00 for Mac (GraphPad Software, La Jolla California USA, www.graphpad.com).

5. 4 Results

To estimate the integrity of primary visual cortex in ACHM we utilised high-resolution T1-weighted scans for each subject and applied surface based morophometry. This allowed us to determine any potential differences in surface area (mm^2), grey matter volume (mm^3) and cortical thickness (mm). The first analysis stream was kept close to the proceeding chapter and used the same ROIs, derived from the Benson atlas, were one represents the central proportions of the visual field (0-4 degrees, $ROI^{central}$) and the other the more paracentral proportions (>4 -8 degrees, $ROI^{paracentral}$).

First, influence of scanner site on global morphometric values (mean surface area, mean thickness and estimated total intracranial volume (eTIV)) were estimated (Appendix A.3). Scanner site showed a significant influence on global mean thickness ($F(2,55)= 4.802$, $p=.012$) but no significant influence on global mean surface area ($F(2, 55) = 2.672$, $p= .078$) and eTIV ($F (2, 55) = 0.3055$, $p=.7380$). As scanner site seemed to influence derived morphometric values, a hierarchical regression was applied where scanner site, but also the influence of gender and age were assessed at the first stage, which allowed us to determine any differences in the patient population without being cofounded by aforementioned factors.

For surface area the applied hierarchical regression revealed that at stage one, entered predictors (gender, age and scanner site) did not contributed significantly to the regression model ($F (4,53) = 1.482$, $p = .221$) and explained only 10.1% of the variation of the dependent variable surface area for $ROI^{central}$. At stage two, participant group was added as an additional predictor variable, which explained an additional 13% of variation in surface area within $ROI^{central}$. This resulted in a

significant R^2 change, F (1,52) = 8.780, p = .005) indicating a significant decrease in surface area in achromats for central visual field representations (Figure 5.2A, Appendix A.6).

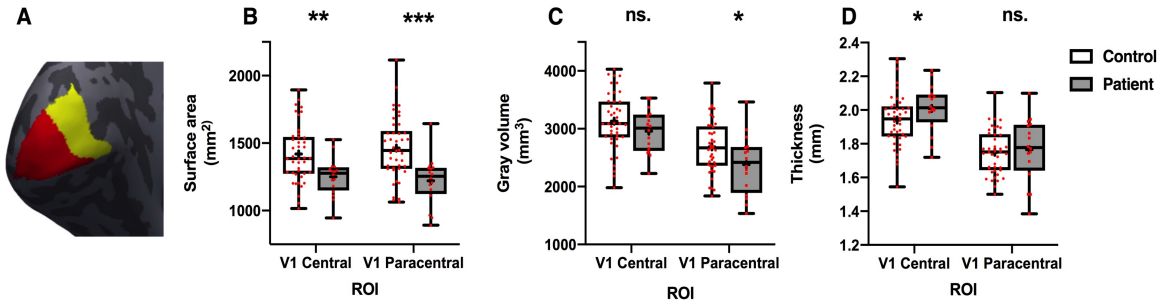

Figure 5.2 ROI surface based morphometric values. **(A)** shows the left hemisphere cortical surface reconstruction of an example participant with the two overlaid ROI labels: $ROI^{central}$l (red) and $ROI^{paracentral}$.(yellow); Total surface area **(B)**, grey volume **(C)** and cortical thickness (**D)** of both ROI for controls and achromats; Whiskers represent min. and max. values, with mean morphometric values denoted as '+'; individual data points are shown in red; *p<.05, **p<.001, ***p<.001;

For paracentral visual field representation ($ROI^{paracentral}$) the hierarchical regression revealed again a similar picture. Predictors (gender, age, scanner site) added at stage one did not contributed significantly to the regression model, F (4,53) = 2.040, p = .102) and could only accounted for 13.3% of the variation. Once participant group was added at stage two an additional 19 % of variation in the depended variable surface area cold be explained. Again, this change in R^2 was significant (F (1,52) = 14.588, p< .0001) and indicated that surface area is also reduced in achromats at paracentral visual field proportions (Figure 5.2A, Appendix A. 7).

While surface area was significantly reduced in achromats overall grey matter volume in the $ROI^{central}$ seemed only marginally affected. This was also reflected by the applied hierarchal regression. Gender, age and scanner site did not significantly contribute to the regression model, F (4,53) = 1.773, p = .148) and accounted for 11.8 % of the variation seen in the dependent variable grey matter volume. Importantly,

participant group could only explain an additional 2%, which did not result in a significant change of R^2 (F (1,52) = 1.226, p = .273) (Appendix A. 4).

In contrast, for $ROI^{paracentral}$ patients showed a reduction in grey matter volume, which was indeed significant (F (1,52) = 5.151, p = .027). Here, the applied hierarchal regression indicated no significant impact from gender, age and scanner site (F (4,53) = 1.508, p = .213) which explained only 10.2% of the variation in grey volume, while participant group accounted for an additional 8.1% of the seen variation to grey matter volume (Figure 5.2C; Appendix A. 5).

We further extracted cortical thickness values, as previous studies often highlighted a thickening of early visual cortex or pericalcarine regions, related to aberrant pruning processes caused by the missing sensory input. As predicted, central visual field representations ($ROI^{central}$) in achromats showed a marginal increase in cortical thickness. The applied hierarchical regression highlight a significant contribution of predictors added at stage one, mainly driven by scanner site, which accounted in total for 20.7% of the variation in the derived data set. Still, adding participant group explained an additional 9.2%, highlighting a significant contribution to the regression model (F (1,52) = 6.836, p = .012) (Figure 5.2C; Appendix A. 4).

The thickening of the cortex seemed to be restricted to only central visual field representations, which was confirmed by the applied hierarchical regression. Neither predictors at stage one (R^2: 1,9%; F (4,53) = .251, p = .907)) or participant group (ΔR^2: 0.2%; F (1,52) = .114, p = .737) contributed significantly to the regression model and only accounted together for 11.4% of the variation in cortical thickness for $ROI^{paracentral}$ (Figure 5.2C; Appendix A. 5).

This first analysis stream emphasised changes to cortical microstructure in ACHM. While surface area is reduced in both ROIs, cortical thickening seems to be localised to visual field regions affected by the actual absolute visual loss in these patients. To investigate if cortical thickening is indeed highly localised at the fovea, thus related to aberrant cortical pruning in this cortical region, or rather a feature of the parafovea, which might indicate compensatory plasticity, we applied the same analysis steps with more refined ROIs. Thus, $ROI^{central}$ was subdivided to represent either the fovea (0-2 degrees) or the parafoveal area (2-4 degrees), which should still result in ROIs with sufficient amount of cortical tissue to guarantee reliable estimates.

Figure 5.3B shows that surface area was reduced at equal levels across both of the new ROIs. The hierarchal regression revealed that participant group contributed significantly to the regression model in both cases (Fovea: F (1,52) = 10.584, p = .002; Parafovea : F (1,52) = 8.846, p = .0.004) and explained an additional 10.7% and 11.3% of the variation, respectively (Appendix A. 12 & 13).

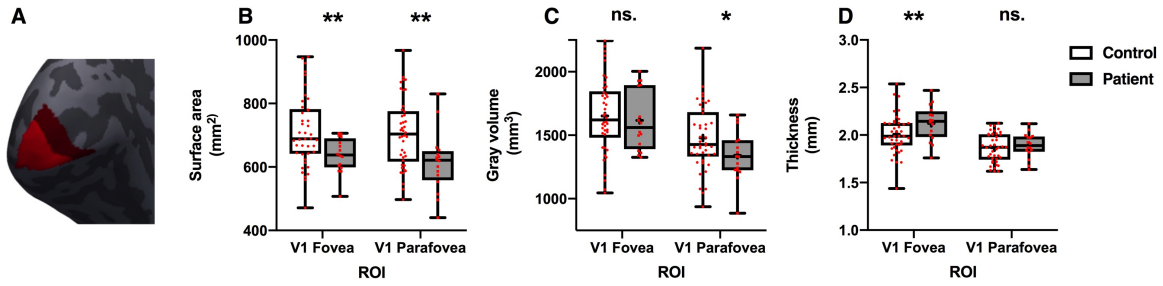

Figure 5.3 ROI surface based morphometric values. **(A)** Left hemisphere cortical shows the cortical surface reconstruction of an example participant with the two overlaid ROI labels: ROI^{fovea} (red) and $ROI^{parafovea}$ (dark red); Total surface area **(B)**, grey volume **(C)** and cortical thickness **(D)** of both ROI for controls and achromats; Whiskers represent min. and max. values, with mean morphometric values denoted as '+'; individual data points are shown in red; *p<.05, **p<.001, ***p<.001;

Compared to surface area, grey matter volume seemed to be only reduced in $ROI^{parafovea}$ (Figure 5.4B). Indeed, for the foveal ROI participant group could not account for any additional variation, resulting in no significant contribution to the

applied model (F (1,52) = 0, p = .9.88). In contrast, the contribution of participant group was significant for $ROI^{parafovea}$ (F (1,52) = 5.151, p = .027) and accounted for 8.1 % of variation (Figure 5.3C, Appendix A .15).

Interestingly, predictors added at stage 1 (gender, age, scanner site) explained up to 36% of the variation in surface area and 44.7% of the variation in grey matter volume in ROI^{fovea}, which was highly significant (surface area: F(4,53)= 7.663, p< 0.001 ; grey volume: F(4,53) = 10.693, p < .001) (Appendix A.12 & 14). Similar to the first analysis stream, the model was mainly driven by gender. A similar pattern can be observed for the $ROI^{parafovea}$, where predictors added at stage one were again significant (Surface area: F(4,53)= 3.727, p=.01; grey matter volume: (F (4,53) = 7.056, p < .001) and accounted for 22.0% (surface area) and 34.7% (grey volume) of the variation (Appendix table A.13 & 15).

For cortical thickness the results are reversed (Figure 5.3C). While the $ROI^{parafovea}$ showed no major differences, also highlighted by the hierarchical regression (2.2 % of variation; F(1,52) = 1.354, p = .250)(Appendix A. 11) participant group explained 12.4% of the variation for ROI^{fovea}, indicating a highly localised significant increased in cortical thickness in achromats (F (1,52) = 9.542, p = .003). Important to note is, that for ROI^{fovea} , stage 1 of the hierarchical regressions is again significant (F(4,53) = 3.313, p = .017) and able to explain 20% of the variation, which is mainly driven by scanner site (Appendix A.10).

In summary, surface area and grey matter volume in primary visual cortex were significantly reduced in patients, while we observed a clear increase in cortical thickness within the foveal representation that encompasses the LPZ.

5.5 Discussion

5.5.1 General overview

The aim of this chapter was to systematically analyse potential changes to cortical structure in achromats, a patient population that congenitally lacks cone function. A surface based approach was applied to detail differences in cortical thickness, surface area and grey matter volume in primary visual cortex utilising high resolution T1-weighted images collected as part of a multicentre collaboration. A region-of-interest-based analysis was performed to allow comparability to a functional imaging study in the same patient cohort; aforementioned measurements were extracted from the same two ROIs, representing the central (0-4 degrees) and paracentral (4-8 degrees) visual field. While surface area was significantly reduced in patients for both ROIs, a decrease in grey matter volume was only observed for $ROI^{paracentral}$. In contrast, cortical thickness increased in achromats for $ROI^{central}$, while no cortical thickening could be observed in paracentral visual field proportions.

We examined the central visual field presentations further to determine if the seen thickness increase was related to aberrant pruning processes in the fovea or indicative for compensatory plasticity in patients, thus more localised at parafoveal visual field representations. Again, surface area was reduced for both ROIs, while a reduction in grey matter volume was only found in the parafovea visual field representations. Further, our results showed that cortical thickening in achromats is highly localised in the fovea.

These fingings highlight that changes to cortical structure also occur in ACHM. All observed findings are in general agreement with other reported changes to cortical

structure in the congenitally blind, which highlight grey matter volume (Bridge et al., 2009; J. Jiang et al., 2009; Park et al., 2009) and surface area reduction (Aguirre et al., 2016; Noppeney et al., 2005; Pan et al., 2007; Park et al., 2009; Ptito et al., 2008) and an increase in cortical thickness within the LPZ (Aguirre et al., 2017, 2016; Anurova et al., 2015; Bridge et al., 2009; d'Almeida et al., 2013; J. Jiang et al., 2009; Park et al., 2009).

5.5.2 Reduction in cortical grey matter volume

Although a grey matter decrease is reported for congenital blind, the reduction in grey volume observed in this study seemed to be mainly localised outside the LPZ, thus extends further than the retinotopic presentation of the absolute scotoma in ACHM (Boucard et al., 2009; Burge et al., 2016; Plank et al., 2011; Prins, Plank, et al., 2016).

It has been shown that surface area and thickness follow separate developmental trajectories (Rakic, 1995; Wierenga et al., 2014), thus might be affected differently in disease. As volume encapsulates information of both, cortical thickness and surface area (Winkler et al., 2018, 2010), opposite changes of these two metrics might lead to no net change in volume. This would again just underpin the problem of limited specificity for cortical volume measurements (Winkler et al., 2018). Here, changes in grey matter volume seemed to be driven by changes to surface area, which was already reported elsewhere (Aguirre et al., 2016; Winkler et al., 2018) but indeed, for all ROIs that showed surface area and thickness changes in the opposite direction, grey matter volume maintained constant. This finding clearly highlights that without further metrics like surface area and thickness the true extent of changes to cortical

structure may not be captured, even when using a surface-based morphometry with an improved approach to estimate cortical volume (Winkler et al., 2018).

5.5.3 Reduction in surface area

While a decrease in surface area is a commonly reported change in congenital blind (Aguirre et al., 2016; Noppeney et al., 2005; Pan et al., 2007; Park et al., 2009; Ptito et al., 2008), the reduction seen here affects the whole extent of primary visual cortex we measured, contrary to the quite localised absolute visual field defect in ACHM (Baseler et al., 2002). Most studies that detailed changes in congenitally blind focused either on the whole primary visual cortex or the pericalcarine areas and were cross-sectional (Aguirre et al., 2016; Park et al., 2009), thus including participants with a variety of visual field defects. In a study by Aguirre et al. (2017) brain integrity in patients with a form of Leber congenital amaurosis (LCA) was examined. While the visual field defect in this patient cohort would be similar to ACHM, Aguirre et al. (2017) just described changes within V1. Importantly, their reported surface area reduction seemed less pronounced compared to a cross-sectional cohort of congenital blind, but if this is related to an overall smaller area reduction or the result of averaging across parts of V1 that show no reduction can not be determined (Aguirre et al., 2017). Thus we can only speculate if surface area in congenital photoreceptor abnormalities shows a reduction that extends beyond the retinotopic area of the absolute visual defect or if the extent of the reduction reported here is unusual.

It is possible that broad reduction in surface area could be a side effect of the methodological approach itself. The ROIs utilised for this study were derived from an anatomical atlas, developed using visual field map estimates from healthy participants with normal vision (Benson et al., 2014). Due to cortical magnification

the cortical area representing cone-only signals occupies a large extent of visual cortex (Baseler et al., 2002; Hadjikhani & Tootell, 2000; Horton & Hoyt, 1991). If in achromats such distinct parts of early visual cortex are indeed decreased, the fitting algorithm might have shifted the eccentricity atlas, perhaps, to more foveal locations. If the whole atlas is shifted this might have affected also paracentral and peripheral proportions of early visual cortex and potentially underestimated the real extend of these ROIs.

This is rather unlikely as first of all, the proceeding chapter showed significant effects of ROI in all analysis streams, indicating that they cover distinct parts of the visual field. More importantly, if the fitting algorithm would have underestimated these ROIs this should have had pronounced effects on mean eccentricity estimates in patients while we found no actual group differences in mean eccentricity under scotopic conditions (see Chapter 4).

Also, anatomical atlases are widely used in patient related structural studies and currently the most sensible way do delineated ROIs (Aguirre et al., 2016; Bridge et al., 2014; Park et al., 2009; Prins, Plank, et al., 2016). Additionally, the applicability of the here utilised retinotopic atlas was not only shown for visual disorders (Aguirre et al., 2017) but also in patients with mental disorders (Reavis et al., 2017).

Thus, it seems more likely that ACHM may have more widespread effects on cortical estimates.

In this respect, surface area is known to reach maximum levels later in life, around the age of nine. Interestingly, pericalcarine areas do not seem to follow this general trend and no age related peak could be observed (Wierenga et al., 2014). In line with this, an even earlier report highlighted peak surface area shortly after birth, especially within the highly convoluted foveal representations, important for central

vision (Leuba & Kraftsik, 1994). In ACHM exactly these cortical areas are deafferent and will not receive any sensory input. This might have profound effects on the cortical maturation process and might impact the later development of the peripheral representations, which would explain the broad area reduction observed here.

More over, while highest cone density is found at the foveola, leading to the absolute scotoma in ACHM, cone photoreceptors are observed at a decreased number up to an eccentricity of 15 degrees (Curcio et al., 1991, 1990; Osterberg, 1937). Thus, the visual defect in ACHM is not just limited to this central visual field region, additionally supporting the possibility that the absence of cone signalling may have more widespread consequences on cortical architecture.

5.5.4 Cortical thickening in the lesion projection zone

The observed cortical thickening in central visual field representations was expected and commonly related to aberrant pruning processes caused by the absent sensory input (Aguirre et al., 2017; Bourgeois et al., 1989; Guerreiro et al., 2015; Park et al., 2009; Stryker & Harris, 1986). While only reported for acquired vision loss, the thickness increase could have also been related to compensatory plasticity, as achromats might use areas adjacent to the lesion projection zone more frequently (Burge et al., 2016). The refined analysis stream quite clearly demonstrated that an increased cortical thickness is only a feature of the fovea, further supporting the idea of a disrupted pruning process. It has yet to be seen if this increase in cortical thickness is also correlated with cross-modal plasticity in ACHM, as reported for other congenital disorders (Aguirre et al., 2017, 2016; Anurova et al., 2015; Cohen et al., 1997, 1999; Cunningham, Weiland, Bao, Lopez-Jaime, & Tjan, 2015; Guerreiro et al., 2015). Important to note is that this study used a standardised automated

algorithm to define cortical thickness (B. Fischl & Dale, 2000), which is susceptible to the degree of intra cortical myelination. Thus, values reported here could just indicate an apparent change in cortical thickness while group differences actually reflect changes in intracortical myelination (Aguirre et al., 2016; Glasser & Van Essen, 2011; Park et al., 2009).

5.5.5 Influence of confounds on surface based estimates

While not of primary interest to this study, stage one of the applied hierarchical regression indicated that a significant amount of variance of our outcome measures can be explained by the either gender or scanner site. Gender mainly had an influence on surface area and volume. As females tend to have an overall smaller brain which results in a reduced grey matter volume and surface area compared to males, this finding is not surprising and is in line with the literature (Vijayakumar et al., 2016; Wierenga et al., 2014). Further, also scanner site had an impact and was able to explain some variability within the data set, especially for cortical thickness measurements. Studies comparing the reliability of surface based estimates generally indicated only small differences in cortical thickness across sessions and across different scanners. Importantly, the highest thickness differences between sessions but especially between scanners were found in the visual cortex (Han et al., 2006). These overall differences are similar to the ones reported here and are related to the increased myelin content at visual areas resulting in a low contrast ratio between grey and white matter (B. Fischl & Dale, 2000; Glasser & Van Essen, 2011). Interestingly, significant influence of confounds was mainly observed at the ROIs representing the central visual field. High gyrification and the increased myelin content at the occipital pole might have affected efficacy of the segmentation process,

thus making the pole region more susceptible for gender differences or scanner influences.

5.5.6 Implications of changes to cortical microstructure for cortical remapping and prospects for current restorative approaches

Initially, cortical reorganisation was reported in ACHM, indicated by the cortical responses seen in the deafferent cortical representations of the fovea (Baseler et al., 2002). A follow up study in a larger and more representative cohort showed that this reported reorganisation is not a general feature in ACHM. While this in itself is beneficial for current clinical interventions, ACHM could still affect cortical integrity. Here, we show that in primary visual cortex in achromats is clearly altered by the missing sensory input and found changes are in close relation to other congenital eye disorders (Aguirre et al., 2016; Park et al., 2009). How these changes will impact current restorative approaches in this patient population cannot be fully answered. While increased cortical thickness and the quite likely related cross-modal plasticity can be a limiting factor (Guerreiro et al., 2015), reports of successfully gene augmentation therapy in LCA highlight that cortical thickening per se is not a contraindication for treatment success (Ashtari et al., 2015; Bennett et al., 2016). Moreover, a study by Aguirre at al. (2017) already suggested that the integrity of the postretinal pathway might also play an important role for successful vision restoration, which has up to now not been investigated in achromats. Importantly, while disease onset has no impact on the extent of surface area reduction, disease duration seems to be correlated with cortical thickening (Q. Li et al., 2017). While ACHM is a mainly stationary disorder (Hirji, Georgiou, et al., 2018), this might

indicate that an early intervention is desirable. Longitudinal studies in this patient population would help to define a time course for the observed cortical changes and might allow defining an ideal time point for clinical interventions to maximise treatment efficacy.

Chapter 6

General Discussion and Outlook

6.1 Overview of the thesis

When visual input is lost due to disease, the brain may undergo changes to adapt to the absent sensory input. While vision loss acquired later in life is mainly associated with atrophic changes, the brain is capable of large-scale reorganisation when vision is lost from birth. A pioneering study by Baseler et al. (2002) was the first to describe compelling evidence for visual cortical remapping in humans. They demonstrated that in achromats, a patient population that congenitally lacks cone function, the designated cortical area that normally computes cone signal was highly responsive to rod-only input.

Vision restoration approaches in achromatopsia (ACHM) in the form of gene augmentation have been developed, with several ongoing clinical trials, but the brain's capability to reorganise might diminish the success of such interventions. As the initial study by Baseler et al. (2002) based their findings on only three high functioning participants, the reported reorganisation might not be representative of the general patient population.

Thus, the overall aim of this thesis was to re-examine cortical maps in further detail in ACHM in a large scale, and hence more representative cohort to aid the advancement of any future therapeutic interventions. This was done in three empirical chapters examining from different angles, if and to what extent the brain undergoes changes when visual input is lost.

We first examined the difference in the visual cortical representation of rod-driven signals compared to the representation of cone-driven signals in normally sighted human participants. This provided an important baseline to compare with interpreted changes to cortical estimates in ACHM, but also offered insight into cortical mechanisms that might maximise sensitivity when visual information is sparse.

Next, we applied both phase-encoded retinotopy and state-of-the-art population receptive field (pRF) modelling to systematically assess previously reported reorganisation in a larger cohort achromats (n=18), recruited as part of a multi-centre effort.

Last, we utilised T1-weighted, high-resolution structural images to examine any changes to cortical structure in primary visual cortex in ACHM using surface-based morphometry.

The following chapter will first summarise the key findings of each chapter before focusing on some shortcomings or additional, not yet mentioned factors that might offer a different perspective. Last, the implications of this study for clinical interventions in ACHM and ideas for future research will be outlined.

6.2 Summary of key findings

First, we found that with decreasing luminance to scotopic levels, foveal representations of primary visual cortex showed a clear reduction in overall responses while paracentral proportions are seemingly unaffected. Moreover, we showed for the first time that low light levels have a lesser impact on extrastriate response levels. Applying connective field modelling revealed that extrastriate foveal

responses under low luminance levels do not emerge from aberrant feedforward connections between V1 and V2, but are likely related to increased spatial pooling properties of V2. Finally, pRF size is increased under low luminance levels, indicating that the increased spatial summation properties of the rod pathway can be measured at the cortical level.

Secondly, visual field estimates of primary visual cortex in achromats revealed that large-scale visual cortical remapping does not seem to be a general feature in this patient population as responses in both central and paracentral proportions were clearly decreased compared to controls. Interestingly, eccentricity estimates showed a slight peripheral shift, which might indicate that some patients still show traces of cortical remapping. Importantly, this study also showed that a subgroup of achromats that presents with atypical rod function has nearly absent cortical responses and differs significantly from achromats with normal rod function.

Finally, surface-based morphometry revealed that brain integrity in primary visual cortex in ACHM is also affected. Results were comparable to other congenital visual disorders and indicated reduced surface area across primary visual cortex. Furthermore, grey matter volume followed the trend of reduced surface area except in portions of visual cortex that showed an increase in cortical thickness. Thickening of the cortex was localised to the cortical representation of the fovea in achromats, further supporting the notion of aberrant pruning processes in congenitally blind individuals.

6.3 Additional considerations

6.3.1 Applicability of different pRF models

Reduced or absent responses in the foveal representation of primary visual cortex under low luminance levels have been described previously (Barton & Brewer, 2015; Baseler et al., 2002; Hadjikhani & Tootell, 2000) and fit well with our general understanding of rod vision. To derive visual field estimates, this study used the standard pRF model fitting a single two-dimensional Gaussian (Dumoulin & Wandell, 2008). Thus, this model is only able to capture positive blood-oxygenation-level dependent (BOLD) responses elicited by the excitatory centre of the classical receptive field represented by the underlying neuronal population.

However, a key feature of receptive fields in the visual system is their antagonistic centre-surround configuration, where activation of the surround of a receptive field has an inhibitory effect (Cavanaugh, Bair, & Movshon, 2002; M. A. Smith, 2006; Spillmann, 2014). This configuration has been described in various electrophysiological studies, but also seems to influence the response patters of fMRI signals (Allman, 1985; Kastner et al., 2017; Nurminen, Kilpeläinen, Laurinen, & Vanni, 2009; Press, Brewer, Dougherty, Wade, & Wandell, 2001; Shmuel et al., 2002).

Zuiderbaan et al. (2012) extended the classical pRF model and incorporated the suppressive surround using a Difference of Gaussian (DoG) function (Spillmann, 2014; Zuiderbaan et al., 2012). The incorporation of the DoG pRF model could highlight if surround suppression is a relevant feature of cortical pRFs under scotopic conditions, thus adding valuable information to the ongoing debate (Barlow et al., 1957; Enroth‐Cugell & Lennie, 1975; Kaplan et al., 1979; Maffei & Fiorentini, 2017; Muller & Dacheux, 1997; Peichl & Wässle, 1983; Wiesel & Hubel, 1966). If

suppression levels are indeed similar across different luminance levels, the incorporation of such an alternative pRF model might be even more relevant as it was shown to account for a higher variance explained in cone-driven BOLD responses. This in turn should result in more stable pRF estimates compared to the standard model (Zuiderbaan et al., 2012).

The increase in pRF size we observed under low luminance levels supports our initial hypothesis, reflecting the larger spatial pooling properties of the rod pathway. This was in contrast to the results reported by Barton and Brewer (2015), and is discussed in detail (see Chapter 3.6.6). However, one other aspect has not been taken into consideration so far. The standard pRF model used bases its estimates on the assumption of linear spatial summation properties (Dumoulin & Wandell, 2008) however, a study by Kay et al. (2013) described nonlinear effects in primary visual cortex. The Compressive Spatial Summation (CSS) pRF model outperformed the standard linear pRF model, especially in extrastriate areas. More importantly, derived pRF size estimates were slightly smaller, concluding that the standard linear pRF model tends to overestimate pRF size. Fortunately, effects on primary visual cortex are only marginal, indicating that the linear assumption is still a close approximation in V1 (Kay et al., 2013). In line with this, a study using pRF mapping to examine chromatic pathway properties found no differences in pRF size or variance explained between the standard linear and the CSS model (Welbourne, Morland, & Wade, 2018). Given that our study makes distinct claims about the spatial pooling properties of the rod pathway, it might be beneficial to assess this dataset without the assumption of linearity, if only to further validate our findings. Another fact worth considering is, that the currently implemented model defines the aperture of the underlying receptive field as circular (Dumoulin & Wandell, 2008; Harvey & Dumoulin, 2011).

However, the receptive field of a neuron or a population of neuron was shown to be more elongated, thus an elliptical shape might capture the underlying orientation of neuronal receptive fields in a more biological relevant way (D. H. Hubel & Wiesel, 1962; Yoshor, Bosking, Ghose, & Maunsell, 2007). Silson et al. (2018) used a cross-validated approach to compare elliptical and circular pRF apertures and highlighted that an elliptical model, with pRFs oriented towards the fovea, is better in explaining the variance seen in the time series compared to the standard circular pRF model. While these findings would be in line with a model-free fMRI approach (Greene, Dumoulin, Harvey, & Ress, 2014) as well as findings from intracranial recordings (Yoshor et al., 2007) a comparative frame-work study by Zeidman et al. (2018) indicated, that the best fit for primary visual cortex was achieved when the DOG model, as proposed by Zuiderbaan et al. (2012), was combined with a circular pRF aperture. It is to note, that these results rely only on data from one participant, thus might not be representative (Zeidman et al., 2018), but might indicate that this model combination could be used as an initial starting point

6.3.2 Alternative explanations for extrastriate foveal responses

As shown, low luminance levels have a lesser impact on cortical maps in extrastriate areas. The presence of foveal responses in extrastriate areas in the absence of V1 signal was attributed to increased spatial pooling properties along the visual hierarchy. While this seems to be the most logical explanation given our results, there are several other peripheral factors, which might also explain foveal signalling in V2 in the absence of V1 responses.

Barton and Brewer hypothesised that extrastriate activity might be related to the bar stimulus used in pRF mapping, and represent a form of 'filling-in' elicited by top-down feedback (Barton & Brewer, 2011, 2015). In line with this, several other studies have also reported extrastriate, top-down feedback to foveal cortical representations, some exclusively to V2 (Shipp, Adams, Moutoussis, & Zeki, 2009; M. A. Williams et al., 2008; Zeki & Shipp, 1989).

Although V2 receives its main input from V1 (Schiller & Malpeli, 1977), there is also evidence for pathways emerging from the lateral geniculate nucleus (LGN) or the pulvinar that bypass V1 (Benevento & Yoshida, 1981; Schmid et al., 2009; Soares, Diogo, Fiorani, Souza, & Gattass, 2004). In addition to direct pathways from the LGN to V5 (Sincich, Park, Wohlgemuth, & Horton, 2004), animal studies also have revealed direct input from the LGN to V2 (Bullier & Kennedy, 1983).

While these possibilities might offer an alternative explanation of the foveal responses seen in V2 in this study, the question remains whether these responses are an independent feature caused by direct input to V2 from either the LGN or pulvinar, or if they are related to LGN input to V5, which subsequently provides top-down signals to V2 (Schmid et al., 2009). This possibility is interesting, as Hadjikhani & Tootell (2000) have shown that MT/V5 is responsive under scotopic conditions, reflecting rod input to the magnocellular pathway; this might indicate a promising avenue for future studies.

6.3.3 Improving fixation stability in patients

A crucial factor for the reliability of the pRF method is fixation stability. Under scotopic conditions, control participants may have decreased fixation performance due to the absence of foveal vision; this is even more relevant for patient studies, as

nystagmus is a general characteristic of ACHM. While fixation instability would have only marginal effects on eccentricity estimates (Baseler et al., 2002), pRF size estimates can be influenced by unstable fixation (Haak, Langers, et al., 2014; Levin et al., 2010). As mentioned previously, this has to be considered before any interpretation can be made.

The study design employed here was adjusted to minimise nystagmus and increase fixation performance in both patients and controls. However, it may be worth considering more advanced procedures that either model the effect of nystagmus, or correct for fixation instabilities in real time.

Ahmadi et al. (2016) overcame this issue by introducing another stimulus condition in which they modelled patient nystagmus in controls; this information was used to vary the location of the fixation cross for controls throughout the scan session. The comparison of estimates derived from this 'jittered' stimulus condition to estimates derived from static fixation allowed them to estimate the influence of nystagmus on the reliability of pRF estimates (Ahmadi et al., 2019). Implementing such a stimulus condition should lead to a more adequate comparison, thus facilitates the interpretation of derived patient pRF estimates.

To date, some studies have also used eye tracking to verify fixation stability (Papanikolaou et al., 2014; Somers, Dale, Seiffert, & Tootell, 1999). Hummer et al. (2016) went a step further and used eye tracker-based gaze correction during data acquisition and showed that this improved the reliability of pRF parameters especially in the data with highest fixation instability. Such an approach firstly requires the presence of an eyetracker at each respective scanner facility. Secondly, the use of goggles with neutral density filters to achieve low luminance conditions

made it impossible for standard video eye trackers to view the eye. Nevertheless, eye tracker-based estimates acquired under photopic conditions could be used as an initial estimate of fixation stability, and serve as an approximation for all other conditions.

6.3.4 The influence of scaling effects, time of the day (TOD) and patient subgroups on surface based measures

Changes to cortical structure in primary visual cortex in ACHM were overall consistent with previously reported changes in congenitally blind individuals, but localised to the foveal representation that lacked input. Global factors, such as age-related decline in grey matter volume, surface area and cortical thickness or distinct gender-related differences can also influence these measurements (Wierenga et al., 2014). While the applied hierarchical regression accounted for these nuisance factors, one further peripheral factor, accounting for global head size, was not included. While overall scaling effects have only marginal influence on cortical thickness, increasing brain size shows distinct effects on surface area and volume (Im et al., 2008). As we found that both, surface area and grey matter volume were reduced in primary visual cortex, controlling for overall brain size might me advisable, to assure these measurements have not been biased by global scaling effects. Moreover, once overall brain size effects are accounted for gender related differences are no longer observed, hence the influence of gender on surface area and volume reported here might actually be linked to overall scaling effects (Im et al., 2008).

Another confound, that was not taken into account in the here reported study is the impact of TOD on derived morphometric measures. In several studies using VBM,

TOD showed a distinct impact on cortical volume (Maclaren, Han, Vos, Fischbein, & Bammer, 2014; Miller et al., 2015; Nakamura, Brown, Narayanan, Collins, & Arnold, 2015) while differences related to TOD were also highlighted for studies using diffusion tensor MRI (C. Jiang et al., 2014; C. Thomas et al., 2018) or positron emission tomography (Buysse et al., 2004). A more recent study by Trefler et al. (2016) assessed the impact of (TOD) on surface-based-estimates and indicated a decrease in both, surface area and cortical thickness. Importantly, only a trend for a reduction in cortical thickness was shown for the occipital cortex. Additionally most scan session used in this study were conducted in the morning (not quantified) to avoid a drop in attention for subsequent functional imaging scans, so it is rather unlikely that TOD has affected our outcome measures in a meaningful way. Especially in multicentre patient studies the focus might be more on facilitating general recruitment to the expense of accurately timing the scans across sites, thus an alternative might be to account for potential TOD effects in the subsequent statistical analysis by adding TOD as another confounding factor.

A study by Aguirre et al. (2016) found high levels of variation within participant groups even when accounting for all peripheral factors, especially in surface area and volume. These variations were described as real, individual differences, where surface area and cortical volume were correlated but independent of thickness. They also showed that congenitally blind patients exhibit the same patterns of inter-subject variability, which again supports the impact of different developmental trajectories. Furthermore, they also noted that the degree of surface area reduction varied substantially across blind participants. As the study was cross-sectional, this may have been related to differences in the extent of visual loss of the patients. In line with this, another study by Aguirre et al (2017), investigating a more homogeneous

cohort of congenitally blind individuals with localised vision loss, showed both less variability and less reduction.

As cortical changes in ACHM have not been investigated previously, the current study pooled all patients to increase statistical power and determine overall changes to cortical structure in primary visual cortex. The preceding pRF study (see Chapter 4) has highlighted significant differences in visual cortical function in a subpopulation of achromats that present with atypical rod function. This subgroup of patients have more severe vision loss, which may lead to more pronounced cortical changes that extend to paracentral visual field regions, thus driving the reduction in surface area and volume observed there. This emphasises the need for further clinical and imaging studies in this subgroup, especially with respect to their suitability for gene augmentation therapy.

6.4 Implications for gene augmentation approaches

Results obtained from this multi-centre study indicated that remapping is not necessarily a general feature in ACHM, and on average, argue against large-scale visual cortical reorganisation. This finding is of important clinical value and increases the likelihood of successful interventions in ACHM. Importantly, applied surface based morphometric analysis showed changes to cortical structure are similar to other reports in congenitally blind and the increase in cortical thickness might indicate the presence of cross-modal plasticity as shown by other studies (Anurova et al., 2015; Bavelier & Neville, 2002; Bedny et al., 2011; Guerreiro et al., 2015; Sadato et al., 2002, 1996). Despite the fact that ACHM is largely a stationary congenital disorder (Hirji, Georgiou, et al., 2018), the findings from the surface-based analysis suggest that early intervention may be preferable to enable sensory input and subsequent

neuronal pruning before the increased cortical thickness and the potentially related cross-modal plasticity counteracts vision restoration approaches.

In summary, our current understanding of changes observed in ACHM present a cautiously optimistic future for successful gene augmentation approaches. Additionally, this study clearly highlighted the importance of evaluating rod function, as ACHM in conjunction with reduced rod function resulted in severely reduced cortical responses. Thus, atypical rod function can be used as a contraindication for current therapeutically interventions, as these participants are likely unsuitable for current treatment efforts and will potentially require an adjusted treatment regime. Our findings thus show the importance of combining clinical assessments with non-invasive imaging. Similar to other studies, the additional objective information gained from functional and structural MRI is of tremendous value that not only complements clinical evaluation, but also allows further assessment of suitability and potentially predict treatment success (Papanikolaou et al., 2014; Ritter et al., 2019; Silson, Aleman, et al., 2018; Smirnakis, 2016).

6.5 Future directions

Several additional experiments may help to answer open questions, and increase our understanding of cortical mechanisms of vision loss and improve the current clinical treatment regime for congenital disorders.

In the current study, the finding of foveal activity under scotopic conditions in extrastriate areas in healthy human participants was attributed to the increased spatial pooling capacities of V2. This could be tested by weighting the signal modulation within the cortical estimates of the rod scotoma in V1 by the connective field of a foveal V2 voxel. One would expect that spatial pooling should denoise

subthreshold signals and lead to more stable, stimulus-driven response patterns. If pooled signals do not show a closer relation to the predicted stimulus driven responses, this would further support the idea that signals within the 'rod scotoma' are indeed random, therefore making it most likely they are due to top-down feedback or to direct input to V2, bypassing V1. While this has no direct clinical relevance, such future experiments would help to decipher mechanisms that optimise cortical responses when visual information is sparse and aid our understanding how sensory information is integrated and interpreted.

Furthermore, our findings resulting from surfaces-based analysis indicated an increase in cortical thickness in the LPZ of patients. While broadly attributed to aberrant synaptic pruning, it is possible that the apparent increase in cortical thickness represents changes in myelin composition (Aguirre et al., 2016; Park et al., 2009). To address this possibility, one could include a scan protocol as described by Glasser et al. (2011) that uses both T1-weighted and T2-weighted images to measure myelin content. If no changes in myelin content are revealed this way, another option would be the use of ultra-high field imaging to determine which layers drive the increase in cortical thickness. For example, based on findings by Kingsbury et al. (2002), Voss and Zatorre (2012) have hypothesised that an increase in cortical thickness might be mainly restricted to layers II, III and V.

Another crucial point is that the current study focused only on changes within primary visual cortex. However, as already mentioned in the discussion of the previous chapter (see Chapter 5.6), post-retinal integrity might also play a key role in restorative success. In fact, congenital blindness has been associated with reduction of post-retinal structures, such as the LGN and optic chiasm (Aguirre et al., 2016; Bridge et al., 2009). Moreover, studies looking at white matter integrity have reported

changes in fractional anisotropy (FA) in the optic tract (Bridge et al., 2009; Levin et al., 2010; Pan et al., 2007). In contrast, while reporting changes in primary visual cortex similar to other studies in congenitally blind individuals, Aguirre et al. (2017) found no differences in FA of the optic tract, nor a significant reduction of LGN or optic chiasm volume in patients with a specific form of Leber congenital amaurosis, which they attributed to preserved retinal structure in these patients. Importantly, while optical-coherence-tomography reports in ACHM are not entirely consistent, they generally indicate some degree of disruption to foveal retinal structure (Genead et al., 2011; Remmer et al., 2015). This might therefore increase the likelihood that post-retinal structures or the optic tract are affected in ACHM and highlights the importance of such a follow-up study.

As visual disorders may affect visual cortical structure and function beyond primary cortex, another promising avenue would be to assess changes to extrastriate, higher order visual areas. While cortical thickness of the dorsal stream seems to covary with primary visual cortex, interpreted as signs of cross-modal plasticity (Voss & Zatorre, 2015), FA revealed a reduction in the ventral but not the dorsal stream in congenitally blind samples (Reislev, Kupers, Siebner, Ptito, & Dyrby, 2016). Based on experiments showing impaired form but seemingly intact motion performance in ACHM (Burton et al., 2016), one assumes that the dorsal stream is intact. Thus, it would be interesting to see if anatomical changes in extrastriate areas support this hypothesis and, with respect to restorative approaches, determine if any signs of structural plasticity in higher order visual areas can be observed.

6.6. Conclusion

This thesis examined cortical changes in a patient population with a congenital photoreceptor abnormality with the overall goal to aid vision restoration approaches. This was done from several angles, where we first described differences in visual cortical properties between the rod and cone pathway in healthy human participants. This revealed not only that the increased spatial pooling property of the rod pathway is reflected at the cortical level but also that the same mechanism might be responsible for persistent foveal responses under low light levels in extrastriate areas. Furthermore, functional MRI highlighted that reorganisation in ACHM is not a general feature at the group level, but that potential individual differences should be taken into account before any therapeutic interventions are initiated. Moreover, surface-based morphometry indicated that ACHM leads to similar changes to cortical structure observed in congenitally blind individuals, but showed for the first time that cortical thickening is highly localised to the foveal representations in ACHM patients. Peripheral factors and possible future avenues were discussed that all aim to improve analysis in patient populations and will help to further detail cortical changes and mechanisms when vision is lost from birth.

Appendix

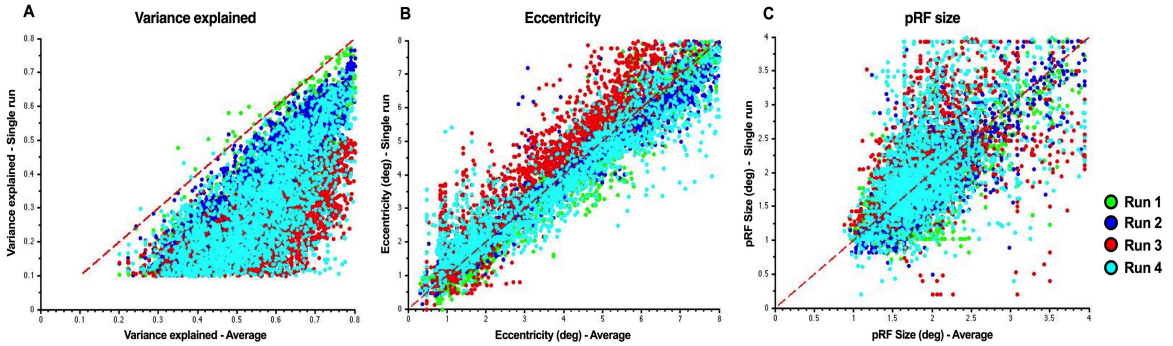

A. 1 Scatter plot correlating the derived V1 pRF estimates from a single stimulus run to pRF estimates derived from the averaged stimuli runs. (A) depicts the correlation of variance explained estimates, (B) pRF eccentricity estimates and (C) pRF size estimates. Depicted are all voxels within V1 of one participant that exceed 10% variance explained in each run.

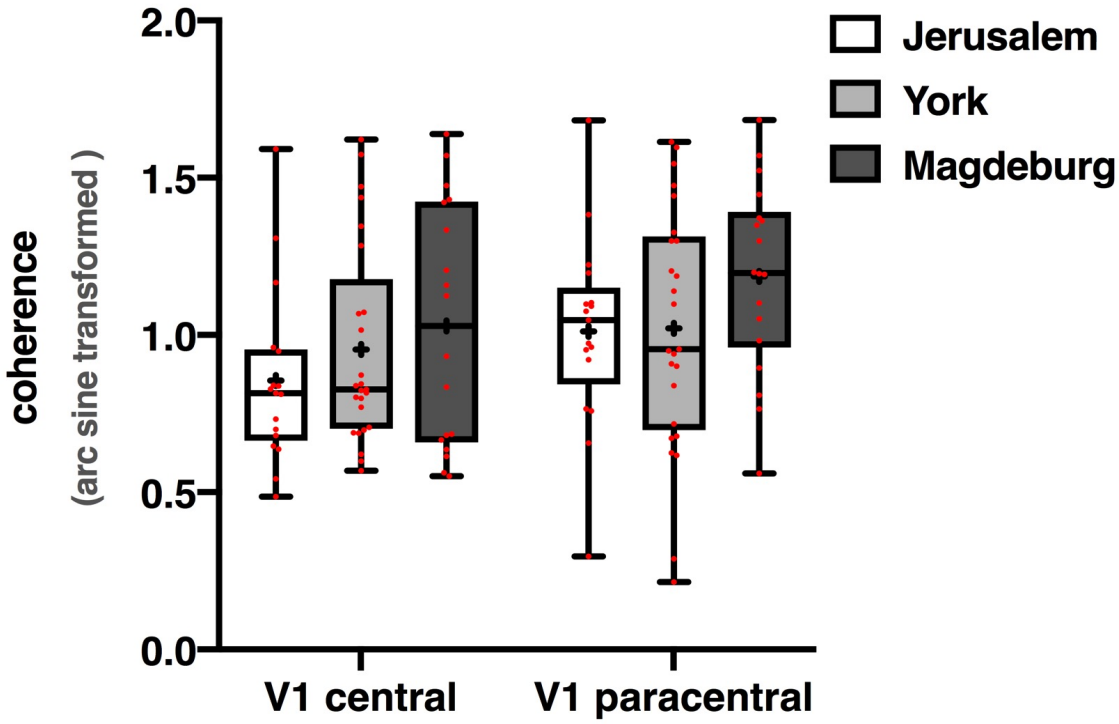

A.2 Reliability of fMRI signal across three different scanner sites. Coherence values were extracted from the phase-encoded data utilised in Chapter 4 for each participant in both regions of interest. All coherence values were sine acr transformed; whiskers represent min. and max. values, with mean coherence values denoted as '+'; individual data points are shown in red; $n^{Jerusalem}$ =17, n^{York} = 25, $n^{Magdeburg}$ = 18;

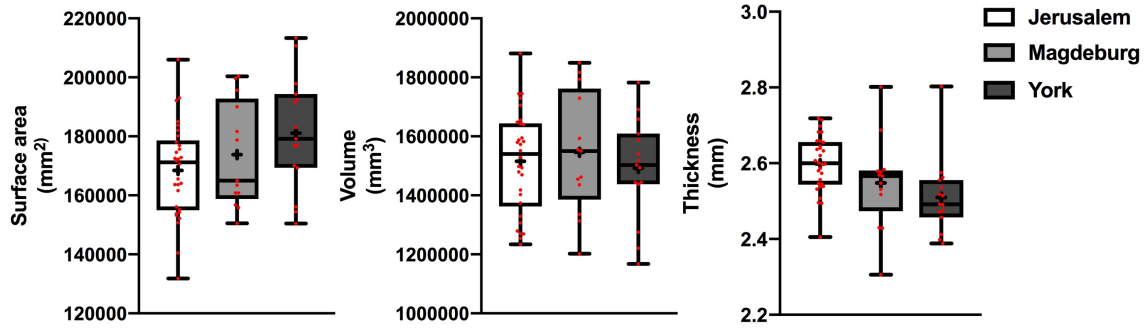

A.3 Reliability of derived global morphometric values across three different scanner sites. Estimates were pooled across hemispheres for mean surface area and mean thickness, where global mean thickness was computed via aforementioned formula (see 5.3.2.3.); whiskers represent min. and max. values, with mean morophmetric values denoted as '+'; individual data points are shown in red; $n^{Jerusalem}$ =30, n^{York} = 15, $n^{Magdeburg}$ = 13

	Variable	B	SE (B)	β	t	p value	R	R^2	ΔR^2
Model 1							.455	.207	.207
	Gender	-.050	.039	-.163	-1.297	.200			
	Age	-.001	.002	-.071	-.556	.581			
	Scanner site	-.155	.049	-.419	-3.199	.002			
	Scanner site	-.087	.046	-.245	-1.901	.063			
Model 2							.547	.299	.092
	Gender	-.034	.037	-.109	-.905	.369			
	Age	-.003	.002	-.184	-1.434	.158			
	Scanner site	-.169	.046	-.455	-.368	.001			
	Scanner site	-.103	.044	-.292	-2.358	.022			
	Participant	.114	.044	.329	2.615	.012			

A. 4 Summary of Hierarchical Regression Analysis for Variables predicting cortical thickness (mm) in ROIcentral; n = 58

	Variable	B	SE (B)	β	t	p value	R	R^2	ΔR^2
Model 1							.136	.019	.019
	Gender	-.019	.041	-.063	-.450	.655			
	Age	-.001	.002	-.053	-.378	.707			
	Scanner site	.018	.052	.051	.349	.729			
	Scanner site	.036	.048	.106	.739	.463			
Model 2							.144	.021	.114
	Gender	-.016	.042	-.055	-.382	.704			
	Age	-.001	.002	-.071	-.467	.643			
	Scanner site	.016	.052	.045	.306	.761			
	Scanner site	.033	.049	.099	.676	.502			
	Participant	.017	.049	.050	.338	.737			

A. 5 Summary of Hierarchical Regression Analysis for Variables predicting cortical thickness (mm) in $ROI^{paracentral}$; n = 58

	Variable	B	SE (B)	β	t	p value	R	R^2	ΔR^2
Model 1							.317	.101	.101
	Gender	-40.920	55.481	-.098	-.738	.464			
	Age	-1.176	2.654	-.060	-.443	.659			
	Scanner site	3.042	69.469	.006	.044	.965			
	Scanner site	-138.763	65.199	-.293	-2.128	.038			
Model 2							.480	.230	.130
	Gender	-67.242	52.564	-.162	-1.279	.206			
	Age	1.458	2.633	.074	.554	.582			
	Scanner site	24.296	65.266	.049	.372	.711			
	Scanner site	-112.602	61.520	-.237	-1.830	.073			
	Participant	-181.712	61.325	-.391	-2.963	.005			

A. 6 Summary of Hierarchical Regression Analysis for Variables predicting surface area (mm^2) in $ROI^{central}$; n = 58

	Variable	B	SE (B)	β	t	p value	R	R^2	ΔR^2
Model 1							.365	.133	.133
	Gender	-88.563	64.416	-.183	-1.397	.168			
	Age	-2.817	3.034	-.123	-.929	.357			
	Scanner site	-13.978	79.405	-.024	-.176	.861			
	Scanner site	-159.133	74.524	-.288	-2.135	.037			
Model 2							.569	.323	.190
	Gender	-125.614	57.402	-.259	-2.188	.033			
	Age	.891	2.876	.039	.310	.758			
	Scanner site	15.941	71.273	.027	.224	.824			
	Scanner site	-122.308	67.182	-.221	-1.821	.074			
	Participant	-255.788	66.970	-.473	-3.819	.000			

A. 7 Summary of Hierarchical Regression Analysis for Variables predicting surface area (mm^2) in $ROI^{paracentral}$; n = 58

	Variable	B	SE (B)	β	t	p value	R	R^2	ΔR^2
Model 1							.344	.118	.118
	Gender	-74.292	123.436	-.080	-.602	.550			
	Age	1.180	5.905	.027	.200	.842			
	Scanner site	-196.904	154.557	-.176	-1.274	.208			
	Scanner site	-369.635	145.057	-.347	-2.548	.014			
Model 2							.372	.138	.020
	Gender	-97.674	124.971	-.105	-.782	.438			
	Age	3.521	6.261	-.080	.562	.576			
	Scanner site	-178.023	155.169	-.159	-1.147	.257			
	Scanner site	-346.395	146.264	-.325	-2.368	.022			
	Participant	-161.421	145.800	-.155	-1.107	.273			

A. 8 Summary of Hierarchical Regression Analysis for Variables predicting grey matter volume (mm^3) in $ROI^{central}$; n = 58

	Variable	B	SE (B)	β	t	p value	R	R^2	ΔR^2
Model 1							.320	.102	.102
	Gender	-221.875	128.100	-.231	-1.732	.089			
	Age	-3.937	6.129	-.087	-.642	.523			
	Scanner site	-24.284	160.397	-.021	-.151	.880			
	Scanner site	-209.520	150.538	-.191	-1.392	.170			
Model 2							.428	.183	.081
	Gender	-269.877	125.161	-.281	-2.156	.036			
	Age	.868	6.270	.019	.138	.890			
	Scanner site	14.479	155.404	.013	.093	.926			
	Scanner site	-161.811	146.485	-.148	-1.105	.274			
	Participant	-33.397	146.021	-.309	-2.270	.027			

A. 9 Summary of Hierarchical Regression Analysis for Variables predicting grey matter volume (mm^3) in $ROI^{paracentral}$; n = 58

	Variable	B	SE (B)	β	t	p value	R	R^2	ΔR^2
Model 1							.447	.200	.200
	Gender	-.067	.051	-.165	-1.307	.197			
	Age	-.001	.002	-.043	-.335	.739			
	Scanner site	-.203	.064	-.416	-3.162	.003			
	Scanner site	-.119	.060	-.256	-1.973	.054			
Model 2							.569	.324	.124
	Gender	-.042	.048	-.103	-.866	.390			
	Age	-.003	.002	-.174	-1.383	.173			
	Scanner site	-.223	.060	-.458	-3.726	.000			
	Scanner site	-.144	.056	-.310	-2.547	.014			
	Participant	.174	.056	.382	3.089	.003			

A. 10 Summary of Hierarchical Regression Analysis for Variables predicting cortical thickness (mm) in ROI^{Fovea}; n = 58

	Variable	B	SE (B)	β	t	p value	R	R^2	ΔR^2
Model 1							.352	.124	.124
	Gender	-.035	.038	-.121	-.922	.361			
	Age	-.001	.002	-.077	-.579	.565			
	Scanner site	-.111	.047	-.323	-2.345	.023			
	Scanner site	-.053	.044	-.161	-1.185	.241			
Model 2							.382	.146	.022
	Gender	-.027	.038	-.095	-.715	.478			
	Age	-.002	.002	-.133	-.940	.352			
	Scanner site	-.117	.047	-.340	-2.466	.017			
	Scanner site	-.060	.045	-.184	-1.343	.185			
	Participant	.052	.045	.162	1.164	.250			

A. 11 Summary of Hierarchical Regression Analysis for Variables predicting cortical thickness (mm) in $ROI^{Parafovea}$; n = 58

	Variable	B	SE (B)	β	t	p value	R	R^2	ΔR^2
Model 1							.605	.366	.366
	Gender	-80.753	23.187	-.390	-3.483	.001			
	Age	-2.730	1.109	-.279	-2.461	.017			
	Scanner site	1.019	29.033	.004	.035	.972			
	Scanner site	69.198	27.248	.293	2.540	.014			
Model 2							.688	.474	.107
	Gender	-92.655	21.649	-.448	-4.280	.000			
	Age	-1.539	1.085	-.157	-1.419	.162			
	Scanner site	10.630	26.880	.043	.395	.694			
	Scanner site	81.027	25.337	.343	3.198	.002			
	Participant	-82.169	25.257	-.355	-3.253	.002			

A. 12 Summary of Hierarchical Regression Analysis for Variables predicting surface area (mm^2) in ROI^{Fovea}; n = 58

	Variable	B	SE (B)	β	t	p value	R	R^2	ΔR^2
Model 1							.469	.220	.220
	Gender	-61.027	27.847	-.272	-2.192	.033			
	Age	-3.048	1.332	-.288	-2.288	.026			
	Scanner site	-10.404	34.867	-.039	-.298	.767			
	Scanner site	35.465	32.724	.139	1.084	.283			
Model 2							.577	.333	.113
	Gender	-74.280	26.369	-.332	-2.817	.007			
	Age	-1.722	1.321	-.163	-1.303	.198			
	Scanner site	.298	32.740	.001	.009	.993			
	Scanner site	48.637	30.861	.190	1.576	.121			
	Participant	-91.495	30.763	-.365	-2.974	.004			

A. 13 Summary of Hierarchical Regression Analysis for Variables predicting surface area (mm^2) in $ROI^{Parafovea}$; n = 58

	Variable	B	SE (B)	β	t	p value	R	R^2	ΔR^2
Model 1							.668	.447	.447
	Gender	-267.020	58.503	-.478	-4.564	.000			
	Age	-5.138	2.799	-.195	-1.836	.072			
	Scanner site	-231.694	73.253	-.346	-3.163	.003			
	Scanner site	45.699	68.751	.072	.665	.509			
Model 2							.668	.447	.000
	Gender	-267.167	59.925	-.478	-4.458	.000			
	Age	-5.123	3.002	-.194	-1.706	.094			
	Scanner site	-231.575	74.405	-.346	-3.112	.003			
	Scanner site	45.845	70.135	.072	.654	.516			
	Participant	-1.015	69.913	-.002	-.015	.988			

A. 14 Summary of Hierarchical Regression Analysis for Variables predicting grey matter volume (mm^3) in ROI^{Fovea}; n = 58

	Variable	B	SE (B)	β	t	p value	R	R^2	ΔR^2
Model 1							.589	.347	.347
	Gender	-189.167	55.651	-.386	-3.399	.001			
	Age	-5.947	2.662	-.257	-2.234	.030			
	Scanner site	-145.241	69.682	-.248	-2.084	.042			
	Scanner site	46.439	65.399	.083	.710	.481			
Model 2							.621	.386	.038
	Gender	-205.940	55.317	-.421	-3.723	.000			
	Age	-4.268	2.771	-.185	-1.540	.130			
	Scanner site	-131.697	68.684	-.225	-1.917	.061			
	Scanner site	63.109	64.742	.113	.975	.334			
	Participant	-115.795	64.537	-.212	-1.794	.079			

A. 15 Summary of Hierarchical Regression Analysis for Variables predicting grey matter volume (mm^3) in $ROI^{Parafovea}$; n = 58

References

Aboshiha, J., Dubis, A. M., Carroll, J., Hardcastle, A. J., & Michaelides, M. (2016, February 1). The cone dysfunction syndromes. *British Journal of Ophthalmology*. https://doi.org/10.1136/bjophthalmol-2014-306505

Aguilar, M., & Stiles, W. S. (1971). Saturation of the rod mechanism of the retina at high levels of stimulation. *Optica Acta*, *18*(1), 59–65. https://doi.org/10.1080/09500347109696914

Aguirre, G. K., Butt, O. H., Datta, R., Roman, A. J., Sumaroka, A., Schwartz, S. B., … Jacobson, S. G. (2017). Postretinal structure and function in severe congenital photoreceptor blindness caused by mutations in the GUCY2D gene. *Investigative Ophthalmology and Visual Science*, *58*(2), 959–973. https://doi.org/10.1167/iovs.16-20413

Aguirre, G. K., Datta, R., Benson, N. C., Prasad, S., Jacobson, S. G., Cideciyan, A. V., … Gennatas, E. D. (2016). Patterns of individual variation in visual pathway structure and function in the sighted and blind. *PLoS ONE*, *11*(11), e0164677. https://doi.org/10.1371/journal.pone.0164677

Ahissar, M., & Hochstein, S. (2004). The reverse hierarchy theory of visual perceptual learning. *Trends in Cognitive Sciences*, *8*(10), 457–464. https://doi.org/10.1016/j.tics.2004.08.011

Ahmadi, K., Fracasso, A., van Dijk, J. A., Kruijt, C., Van genderen, M. M., Dumoulin, S. O., & Hoffmann, M. B. (2019, April 15). Altered organization of the visual cortex in FHONDA syndrome. *NeuroImage*. Academic Press. https://doi.org/10.1016/j.neuroimage.2018.02.053

Ahnelt, P. K. (1998). The photoreceptor mosaic. *Eye (Basingstoke)*, *12*(3), 531–540. https://doi.org/10.1038/eye.1998.142

Ahuja, Y., Kohl, S., & Traboulsi, E. I. (2008). CNGA3 mutations in two United Arab Emirates families with achromatopsia. *Molecular Vision*, *14*, 1293–1297. Retrieved from http://www.ncbi.nlm.nih.gov/pubmed/18636117

Alexander, J. J., Umino, Y., Everhart, D., Chang, B., Min, S. H., Li, Q., … Hauswirth, W. W. (2007). Restoration of cone vision in a mouse model of achromatopsia. *Nature Medicine*, *13*(6), 685–687. https://doi.org/10.1038/nm1596

Allman, J. (1985). Stimulus Specific Responses from Beyond the Classical Receptive Field: Neurophysiological Mechanisms for Local-Global Comparisons in Visual Neurons. *Annual Review of Neuroscience*, *8*(1), 407–430. https://doi.org/10.1146/annurev.neuro.8.1.407

Alvarez, I., de Haas, B., Clark, C. A., Rees, G., & Schwarzkopf, D. S. (2015). Comparing different stimulus configurations for population receptive field mapping in human fMRI. *Frontiers in Human Neuroscience*, *9*, 96. https://doi.org/10.3389/fnhum.2015.00096

Amicuzi, I., Stortini, M., Petrarca, M., Di Giulio, P., Di Rosa, G., Fariello, G., … Castelli, E. (2006). Visual recognition and visually guided action after early bilateral lesion of occipital cortex: A behavioral study of a 4.6-year-old girl. *Neurocase*, *12*(5), 263–279. https://doi.org/10.1080/13554790601026106

Andrews, T. J., Halpern, S. D., & Purves, D. (1997). Correlated size variations in human visual cortex, lateral geniculate nucleus, and optic tract. *The Journal of Neuroscience : The Official Journal of the Society for Neuroscience*, *17*(8), 2859–2868. Retrieved from http://www.jneurosci.org/content/17/8/2859.long

Anurova, I., Renier, L. A., Volder, A. G. De, Carlson, S., & Rauschecker, J. P. (2015). Relationship Between Cortical Thickness and Functional Activation in the Early Blind. *Cerebral Cortex (New York, NY)*, *25*(8), 2035. https://doi.org/10.1093/CERCOR/BHU009

Arden, G. B., & Frumkes, T. E. (1986). Stimulation of rods can increase cone flicker ERGs in man. *Vision Research*, *26*(5), 711–721. Retrieved from http://www.ncbi.nlm.nih.gov/pubmed/3750851

Ashburner, J., & Friston, K. J. (2000). Voxel-based morphometry - The methods. *NeuroImage*, *11*(6 I), 805–821. https://doi.org/10.1006/nimg.2000.0582

Ashtari, M., Cyckowski, L. L., Monroe, J. F., Marshall, K. A., Chung, D. C., Auricchio, A., … Bennett, J. (2011). The human visual cortex responds to gene therapy-mediated recovery of retinal function. *Journal of Clinical Investigation*, *121*(6), 2160–2168. https://doi.org/10.1172/JCI57377

Ashtari, M., Zhang, H., Cook, P. A., Cyckowski, L. L., Shindler, K. S., Marshall, K. A., … Bennett, J. (2015). Plasticity of the human visual system after retinal gene therapy in patients with Leber's congenital amaurosis. *Science Translational Medicine*, *7*(296), 296ra110. https://doi.org/10.1126/scitranslmed.aaa8791

Bainbridge, J. W., Smith, A. J., Barker, S. S., Robbie, S., Henderson, R., Balaggan, K., … Ali, R. R. (2008). Effect of gene therapy on visual function in Leber's congenital amaurosis. *The New England Journal of Medicine*, *358*(21), 2231–2239. https://doi.org/10.1056/NEJMoa0802268

Baker, C. I., Dilks, D. D., Peli, E., & Kanwisher, N. (2008). Reorganization of visual processing in macular degeneration: Replication and clues about the role of foveal loss. *Vision Research*, *48*(18), 1910–1919. https://doi.org/10.1016/j.visres.2008.05.020

Baker, C. I., Peli, E., Knouf, N., Kanwisher, N. G., Nicholas, K., & Kanwisher, N. G. (2005). Reorganization of Visual Processing in Macular Degeneration. *The Journal of*

Neuroscience, *25*(3), 614–618. https://doi.org/10.1523/JNEUROSCI.3476-04.2005

Banin, E., Gootwine, E., Obolensky, A., Ezra-Elia, R., Ejzenberg, A., Zelinger, L., … Ofri, R. (2015). Gene Augmentation Therapy Restores Retinal Function and Visual Behavior in a Sheep Model of CNGA3 Achromatopsia. *Molecular Therapy*, *23*(9), 1423–1433. https://doi.org/10.1038/mt.2015.114

Barbur, J. L., Watson, J. D., Frackowiak, R. S., & Zeki, S. (1993). Conscious visual perception without V1. *Brain : A Journal of Neurology*, *116 (Pt 6*, 1293–1302. https://doi.org/10.1093/brain/116.6.1293

Barlow, H. B. (1956). Retinal Noise and Absolute Threshold. *Journal of the Optical Society of America*, *46*(8), 634. https://doi.org/10.1364/josa.46.000634

Barlow, H. B. (1958). Temporal and spatial summation in human vision at different background intensities. *The Journal of Physiology*, *141*(2), 337–350. https://doi.org/10.1113/jphysiol.1958.sp005978

Barlow, H. B., Fitzhugh, R., & Kuffler, S. W. (1957). Change of organization in the receptive fields of the cat's retina during dark adaptation. *The Journal of Physiology*, *137*(3), 338–354. https://doi.org/10.1113/jphysiol.1957.sp005817

Barton, B., & Brewer, A. (2011). FMRI of the rod scotoma: Cortical projections, filling-in and insights into plasticity. *Journal of Vision*. Retrieved from https://scholar.google.com/scholar?cluster=7038644515373238425&hl=en&oi=scholarr

Barton, B., & Brewer, A. A. (2015). fMRI of the rod scotoma elucidates cortical rod pathways and implications for lesion measurements. *Proceedings of the National Academy of Sciences*, *112*(16), 5201–5206. https://doi.org/10.1073/pnas.1423673112

Baseler, H. A., Brewer, A. A., Sharpe, L. T., Morland, A. B., Jaägle, H., & Wandell, B. A. (2002). Reorganization of human cortical maps caused by inherited photoreceptor abnormalities. *Nature Neuroscience*, *5*(4), 364–370. https://doi.org/10.1038/nn817

Baseler, H. A., Gouws, A. D., Haak, K. V., Racey, C., Crossland, M. D., Tufail, A., … Morland, A. B. (2011). Large-scale remapping of visual cortex is absent in adult humans with macular degeneration. *Nature Neuroscience*, *14*(5), 649–657. https://doi.org/10.1038/nn.2793

Battista, J., Kalloniatis, M., & Metha, A. (2005, September 1). Visual function: The problem with eccentricity. *Clinical and Experimental Optometry*. John Wiley & Sons, Ltd (10.1111). https://doi.org/10.1111/j.1444-0938.2005.tb06715.x

Bavelier, D., & Neville, H. J. (2002). Cross-modal plasticity: where and how? *Nature Reviews Neuroscience*, *3*(6), 443–452. https://doi.org/10.1038/nrn848

Bedny, M., Pascual-Leone, A., Dodell-Feder, D., Fedorenko, E., & Saxe, R. (2011). Language processing in the occipital cortex of congenitally blind adults. *Proceedings of the National*

Academy of Sciences, *108*(11), 4429–4434. https://doi.org/10.1073/pnas.1014818108

Benevento, L. A., & Yoshida, K. (1981). The afferent and efferent organization of the lateral geniculo-prestriate pathways in the macaque monkey. *Journal of Comparative Neurology*, *203*(3), 455–474. https://doi.org/10.1002/cne.902030309

Bennett, J., Wellman, J., Marshall, K. A., McCague, S., Ashtari, M., DiStefano-Pappas, J., … Maguire, A. M. (2016). Safety and durability of effect of contralateral-eye administration of AAV2 gene therapy in patients with childhood-onset blindness caused by RPE65 mutations: a follow-on phase 1 trial. *The Lancet*, *388*(10045), 661–672. https://doi.org/10.1016/S0140-6736(16)30371-3

Benson, N. C., Butt, O. H., Brainard, D. H., & Aguirre, G. K. (2014). Correction of Distortion in Flattened Representations of the Cortical Surface Allows Prediction of V1-V3 Functional Organization from Anatomy. *PLoS Computational Biology*, *10*(3), e1003538. https://doi.org/10.1371/journal.pcbi.1003538

Benson, N. C., & Winawer, J. (2018). Large individual differences in human visual cortex revealed by Bayesian analysis of retinotopic maps. *BioRxiv*, 325597. https://doi.org/10.1101/325597

Berger, W., Kloeckener-Gruissem, B., & Neidhardt, J. (2010, September). The molecular basis of human retinal and vitreoretinal diseases. *Progress in Retinal and Eye Research*. https://doi.org/10.1016/j.preteyeres.2010.03.004

Beyeler, M., Rokem, A., Boynton, G. M., & Fine, I. (2017). Learning to see again: Biological constraints on cortical plasticity and the implications for sight restoration technologies. *Journal of Neural Engineering*. https://doi.org/10.1088/1741-2552/aa795e

Binda, P., Thomas, J. M., Boynton, G. M., & Fine, I. (2013). Minimizing biases in estimating the reorganization of human visual areas with BOLD retinotopic mapping. *Journal of Vision*, *13*(7), 13–13. https://doi.org/10.1167/13.7.13

Boucard, C. C., Hernowo, A. T., Maguire, R. P., Jansonius, N. M., Roerdink, J. B. T. M., Hooymans, J. M. M., & Cornelissen, F. W. (2009). Changes in cortical grey matter density associated with long-standing retinal visual field defects. *Brain*, *132*(7), 1898–1906. https://doi.org/10.1093/brain/awp119

Bourgeois, J. P., Jastreboff, P. J., & Rakic, P. (1989). Synaptogenesis in visual cortex of normal and preterm monkeys: evidence for intrinsic regulation of synaptic overproduction. *Proceedings of the National Academy of Sciences*, *86*(11), 4297–4301. https://doi.org/10.1073/pnas.86.11.4297

Brainard, D. H. (1997). The Psychophysics Toolbox. *Spatial Vision*, *10*(4), 433–436. https://doi.org/10.1163/156856897X00357

Brewer, A. A., & Barton, B. (2012). Visual Field Map Organization in Human Visual Cortex. In

Visual Cortex - Current Status and Perspectives. InTech. https://doi.org/10.5772/51914

Brewer, A. A., & Barton, B. (2014). Developmental Plasticity: FMRI Investigations into Human Visual Cortex. In *Advanced Brain Neuroimaging Topics in Health and Disease - Methods and Applications*. InTech. https://doi.org/10.5772/58277

Bridge, H., Cowey, A., Ragge, N., & Watkins, K. E. (2009). Imaging studies in congenital anophthalmia reveal preservation of brain architecture in "visual" cortex. *Brain*, *132*(12), 3467–3480. https://doi.org/10.1093/brain/awp279

Bridge, H., von dem Hagen, E. A. H., Davies, G., Chambers, C., Gouws, A. D., Hoffmann, M. B., & Morland, A. B. (2014). Changes in brain morphology in albinism reflect reduced visual acuity. *Cortex*, *56*, 64–72. https://doi.org/10.1016/j.cortex.2012.08.010

Brown, H. D. H., Woodall, R. L., Kitching, R. E., Baseler, H. A., & Morland, A. B. (2016, May). Using magnetic resonance imaging to assess visual deficits: A review. *Ophthalmic and Physiological Optics*. https://doi.org/10.1111/opo.12293

Buck, S. L. (2014). The interaction of rod and cone signals: pathways and psychophysics. In *The New Visual Neurosciences* (pp. 485–497). Retrieved from https://pdfs.semanticscholar.org/5fba/795dfad44312dc5ec9118144071262e1d6aa.pdf

Bullier, J., & Kennedy, H. (1983). Projection of the lateral geniculate nucleus onto cortical area V2 in the macaque monkey. *Experimental Brain Research*, *53*(1), 168–172. https://doi.org/10.1007/BF00239409

Burge, W. K., Griffis, J. C., Nenert, R., Elkhetali, A., Decarlo, D. K., Ver Hoef, L. W., … Visscher, K. M. (2016). Cortical thickness in human V1 associated with central vision loss. *Scientific Reports*, *6*(1), 23268. https://doi.org/10.1038/srep23268

Burton, E., Wattam-Bell, J., S Rubin, G., Aboshiha, J., Michaelides, M., Atkinson, J., … Nardini, M. (2016). Dissociations in Coherence Sensitivity Reveal Atypical Development of Cortical Visual Processing in Congenital Achromatopsia. *Investigative Ophthalmology & Visual Science*, *57*(4), 2251–2259. https://doi.org/10.1167/iovs.15-18414

Buysse, D. J., Nofzinger, E. A., Germain, A., Meltzer, C. C., Wood, A., Ombao, H., … Moore, R. Y. (2004). Regional brain glucose metabolism during morning and evening wakefulness in humans: Preliminary findings. *Sleep*, *27*(7), 1245–1254. https://doi.org/10.1093/sleep/27.7.1245

Callaway, E. M. (2005, July 1). Structure and function of parallel pathways in the primate early visual system. *Journal of Physiology*. Wiley-Blackwell. https://doi.org/10.1113/jphysiol.2005.088047

Carroll, J., Choi, S. S., & Williams, D. R. (2008). In vivo imaging of the photoreceptor mosaic of a rod monochromat. *Vision Research*, *48*(26), 2564–2568.

https://doi.org/10.1016/j.visres.2008.04.006

Carvalho, L. S., Xu, J., Pearson, R. A., Smith, A. J., Bainbridge, J. W., Morris, L. M., … Ali, R. R. (2011). Long-term and age-dependent restoration of visual function in a mouse model of CNGB3-associated achromatopsia following gene therapy. *Human Molecular Genetics*, *20*(16), 3161–3175. https://doi.org/10.1093/hmg/ddr218

Cavanaugh, J. R., Bair, W., & Movshon, J. A. (2002). Selectivity and Spatial Distribution of Signals From the Receptive Field Surround in Macaque V1 Neurons. *Journal of Neurophysiology*, *88*(5), 2547–2556. https://doi.org/10.1152/jn.00693.2001

Chader, G. J. (2002). Animal models in research on retinal degenerations: past progress and future hope. *Vision Research*, *42*(4), 393–399. Retrieved from http://www.ncbi.nlm.nih.gov/pubmed/11853755

Chang, B., Grau, T., Dangel, S., Hurd, R., Jurklies, B., Sener, E. C., … Wissinger, B. (2009). A homologous genetic basis of the murine cpfl1 mutant and human achromatopsia linked to mutations in the PDE6C gene. *Proceedings of the National Academy of Sciences*, *106*(46), 19581–19586. https://doi.org/10.1073/pnas.0907720106

Cideciyan, A. V., Aleman, T. S., Boye, S. L., Schwartz, S. B., Kaushal, S., Roman, A. J., … Hauswirth, W. W. (2008). Human gene therapy for RPE65 isomerase deficiency activates the retinoid cycle of vision but with slow rod kinetics. *Proceedings of the National Academy of Sciences*, *105*(39), 15112–15117. https://doi.org/10.1073/pnas.0807027105

Cideciyan, A. V., & Jacobson, S. G. (2019). Leber Congenital Amaurosis (LCA): Potential for Improvement of Vision. *Investigative Ophthalmology & Visual Science*, *60*(5), 1680–1695. https://doi.org/10.1167/iovs.19-26672

Cideciyan, A. V., Jacobson, S. G., Beltran, W. A., Sumaroka, A., Swider, M., Iwabe, S., … Aguirre, G. D. (2013). Human retinal gene therapy for Leber congenital amaurosis shows advancing retinal degeneration despite enduring visual improvement. *Proceedings of the National Academy of Sciences*, *110*(6), E517–E525. https://doi.org/10.1073/pnas.1218933110

Clarke, F. J. J. (1960). A Study of Troxler's Effect. *Optica Acta: International Journal of Optics*, *7*(3), 219–236. https://doi.org/10.1080/713826335

Cohen, L. G., Celnik, P., Pascual-Leone, A., Corwell, B., Faiz, L., Dambrosia, J., … Hallett, M. (1997). Functional relevance of cross-modal plasticity in blind humans. *Nature*, *389*(6647), 180–183. https://doi.org/10.1038/38278

Cohen, L. G., Weeks, R. A., Sadato, N., Celnik, P., Ishii, K., & Hallett, M. (1999). Period of susceptibility for cross-modal plasticity in the blind. *Annals of Neurology*, *45*(4), 451–460. Retrieved from http://www.ncbi.nlm.nih.gov/pubmed/10211469

Colella, P., & Auricchio, A. (2012). Gene Therapy of Inherited Retinopathies: A Long and Successful Road from Viral Vectors to Patients. *Human Gene Therapy*, *23*(8), 796–807. https://doi.org/10.1089/hum.2012.123

Cunningham, S. I., Weiland, J. D., Bao, P., Lopez-Jaime, G. R., & Tjan, B. S. (2015). Correlation of vision loss with tactile-evoked V1 responses in retinitis pigmentosa. *Vision Research*, *111*(Pt B), 197–207. https://doi.org/10.1016/j.visres.2014.10.015

Curcio, C. A., & Allen, K. A. (1990). Topography of ganglion cells in human retina. *The Journal of Comparative Neurology*, *300*(1), 5–25. https://doi.org/10.1002/cne.903000103

Curcio, C. A., Allen, K. A., Sloan, K. R., Lerea, C. L., Hurley, J. B., Klock, I. B., & Milam, A. H. (1991). Distribution and morphology of human cone photoreceptors stained with anti-blue opsin. *Journal of Comparative Neurology*, *312*(4), 610–624. https://doi.org/10.1002/cne.903120411

Curcio, C. A., Sloan, K. R., Kalina, R. E., & Hendrickson, A. E. (1990). Human photoreceptor topography. *Journal of Comparative Neurology*, *292*(4), 497–523. https://doi.org/10.1002/cne.902920402

d'Almeida, O. C., Mateus, C., Reis, A., Grazina, M. M., & Castelo-Branco, M. (2013). Long term cortical plasticity in visual retinotopic areas in humans with silent retinal ganglion cell loss. *NeuroImage*, *81*, 222–230. https://doi.org/10.1016/j.neuroimage.2013.05.032

Dacey, D. M., & Petersen, M. R. (1992). Dendritic field size and morphology of midget and parasol ganglion cells of the human retina. *Proceedings of the National Academy of Sciences of the United States of America*, *89*(20), 9666–9670. Retrieved from https://www.pnas.org/content/pnas/89/20/9666.full.pdf

Dale, A. M., Fischl, B., & Sereno, M. I. (1999). Cortical surface-based analysis: I. Segmentation and surface reconstruction. *NeuroImage*, *9*(2), 179–194. https://doi.org/10.1006/nimg.1998.0395

Desikan, R. S., Ségonne, F., Fischl, B., Quinn, B. T., Dickerson, B. C., Blacker, D., … Killiany, R. J. (2006). An automated labeling system for subdividing the human cerebral cortex on MRI scans into gyral based regions of interest. *NeuroImage*, *31*(3), 968–980. https://doi.org/10.1016/j.neuroimage.2006.01.021

Dhruv, N. T., & Carandini, M. (2014). Cascaded Effects of Spatial Adaptation in the Early Visual System. *Neuron*, *81*(3), 529–535. https://doi.org/10.1016/j.neuron.2013.11.025

Dubis, A. M., Cooper, R. F., Aboshiha, J., Langlo, C. S., Sundaram, V., Liu, B., … Michaelides, M. (2014). Genotype-dependent variability in residual cone structure in achromatopsia: Toward developing metrics for assessing cone health. *Investigative Ophthalmology and Visual Science*, *55*(11), 7303–7311. https://doi.org/10.1167/iovs.14-14225

Dubra, A., Sulai, Y., Norris, J. L., Cooper, R. F., Dubis, A. M., Williams, D. R., & Carroll, J. (2011).

Noninvasive imaging of the human rod photoreceptor mosaic using a confocal adaptive optics scanning ophthalmoscope. *Biomedical Optics Express*, *2*(7), 1864. https://doi.org/10.1364/BOE.2.001864

Dumoulin, S. O., & Wandell, B. A. (2008). Population receptive field estimates in human visual cortex. *NeuroImage*, *39*(2), 647–660. https://doi.org/10.1016/j.neuroimage.2007.09.034

Engel, S. A., Glover, G. H., & Wandell, B. A. (1997). Retinotopic organization in human visual cortex and the spatial precision of functional MRI. *Cerebral Cortex*, *7*(2), 181–192. https://doi.org/10.1093/cercor/7.2.181

Engel, S. A., Rumelhart, D. E., Wandell, B. A., Lee, A. T., Glover, G. H., Chichilnisky, E. J., & Shadlen, M. N. (1994, June 16). FMRI of human visual cortex [5]. *Nature*. Nature Publishing Group. https://doi.org/10.1038/369525a0

Enroth-Cugell, C., & Lennie, P. (1975). The control of retinal ganglion cell discharge by receptive field surrounds. *The Journal of Physiology*, *247*(3), 551–578. https://doi.org/10.1113/jphysiol.1975.sp010947

Eysel, U. T. (1999). Increased Receptive Field Size in the Surround of Chronic Lesions in the Adult Cat Visual Cortex. *Cerebral Cortex*, *9*(2), 101–109. https://doi.org/10.1093/cercor/9.2.101

Felleman, D. J., & Van Essen, D. C. (1991). Distributed hierarchical processing in the primate cerebral cortex. *Cerebral Cortex*, *1*(1), 1–47. https://doi.org/10.1093/cercor/1.1.1

Fine, I., Cepko, C. L., & Landy, M. S. (2015). Vision research special issue: Sight restoration: Prosthetics, optogenetics and gene therapy. *Vision Research*, *111*(Pt B), 115–123. https://doi.org/10.1016/j.visres.2015.04.012

Fine, I., Wade, A. R., Brewer, A. A., May, M. G., Goodman, D. F., Boynton, G. M., … MacLeod, D. I. A. (2003). Long-term deprivation affects visual perception and cortex. *Nature Neuroscience*, *6*(9), 915–916. https://doi.org/10.1038/nn1102

Fischl, B., & Dale, A. M. (2000). Measuring the thickness of the human cerebral cortex from magnetic resonance images. *Proceedings of the National Academy of Sciences of the United States of America*, *97*(20), 11050–11055. https://doi.org/10.1073/pnas.200033797

Fischl, Bruce, Sereno, M. I., & Dale, A. M. (1999). Cortical surface-based analysis: II. Inflation, flattening, and a surface-based coordinate system. *NeuroImage*, *9*(2), 195–207. https://doi.org/10.1006/nimg.1998.0396

Fischl, Bruce, Sereno, M. I., Tootell, R. B. H., & Dale, A. M. (1999). High-resolution intersubject averaging and a coordinate system for the cortical surface. *Human Brain Mapping*, *8*(4), 272–284. https://doi.org/10.1002/(SICI)1097-0193(1999)8:4<272::AID-

HBM10>3.0.CO;2-4

Fischl, Bruce, Van Der Kouwe, A., Destrieux, C., Halgren, E., Ségonne, F., Salat, D. H., … Dale, A. M. (2004). Automatically Parcellating the Human Cerebral Cortex. *Cerebral Cortex*, *14*(1), 11–22. https://doi.org/10.1093/cercor/bhg087

Fisher, K., & Carr, C. (1970). *A study of individual variability in dark adaptation and night vision in man*. *Washington, D.C: Life Sciences Division, Army Research Office*. Retrieved from https://apps.dtic.mil/docs/citations/AD0722798

Genead, M. A., Fishman, G. A., Rha, J., Dubis, A. M., Bonci, D. M. O., Dubra, A., … Carroll, J. (2011). Photoreceptor structure and function in patients with congenital achromatopsia. *Investigative Ophthalmology and Visual Science*, *52*(10), 7298–7308. https://doi.org/10.1167/iovs.11-7762

Giaschi, D., Jan, J. E., Bjorson, B., Young, S. A., Tata, M., Lyons, C. J., … Wong, P. K. H. (2003). Conscious visual abilities in a patient with early bilateral occipital damage. *Developmental Medicine and Child Neurology*, *45*(11), 772–781. https://doi.org/10.1017/S0012162203001439

Gilbert, C. D., & Wiesel, T. N. (1992). Receptive field dynamics in adult primary visual cortex. *Nature*, *356*(6365), 150–152. https://doi.org/10.1038/356150a0

Girard, P., & Bullier, J. (2017). Visual activity in area V2 during reversible inactivation of area 17 in the macaque monkey. *Journal of Neurophysiology*, *62*(6), 1287–1302. https://doi.org/10.1152/jn.1989.62.6.1287

Glasser, M. F., & Van Essen, D. C. (2011). Mapping Human Cortical Areas In Vivo Based on Myelin Content as Revealed by T1- and T2-Weighted MRI. *Journal of Neuroscience*, *31*(32), 11597–11616. https://doi.org/10.1523/jneurosci.2180-11.2011

Goodchild, A. K., Ghosh, K. K., & Martin, P. R. (1996). Comparison of photoreceptor spatial density and ganglion cell morphology in the retina of human, macaque monkey, cat, and the marmoset Callithrix jacchus. *Journal of Comparative Neurology*, *366*(1), 55–75. https://doi.org/10.1002/(SICI)1096-9861(19960226)366:1<55::AID-CNE5>3.0.CO;2-J

Gootwine, E., Abu-Siam, M., Obolensky, A., Rosov, A., Honig, H., Nitzan, T., … Seroussi, E. (2017). Gene augmentation therapy for a missense substitution in the cGMP-binding domain of ovine CNGA3 gene restores vision in day-blind sheep. *Investigative Ophthalmology and Visual Science*, *58*(3), 1577–1584. https://doi.org/10.1167/iovs.16-20986

Green, D. G. (1970). Regional variations in the visual acuity for interference fringes on the retina. *The Journal of Physiology*, *207*(2), 351–356. https://doi.org/10.1113/jphysiol.1970.sp009065

Greene, C. A., Dumoulin, S. O., Harvey, B. M., & Ress, D. (2014). Measurement of population

receptive fields in human early visual cortex using back-projection tomography. *Journal of Vision*, *14*(1). https://doi.org/10.1167/14.1.17

Gregory, R. L., & Wallace, J. G. (1963). Recovery from Early Blindness: A Case Study. In *Experimental Psychology Society Monograph 2* (pp. 65–129). Retrieved from http://www.richardgregory.org/papers/recovery_blind/recovery-from-early-blindness.pdf

Grünert, U. (1997). Anatomical evidence for rod input to the parvocellular pathway in the visual system of the primate. *European Journal of Neuroscience*, *9*(3), 617–621. https://doi.org/10.1111/j.1460-9568.1997.tb01638.x

Guerreiro, M. J. S., Erfort, M. V., Henssler, J., Putzar, L., & Röder, B. (2015). Increased visual cortical thickness in sight-recovery individuals. *Human Brain Mapping*, *36*(12), 5265–5274. https://doi.org/10.1002/hbm.23009

Guzzetta, A., Cioni, G., Cowan, F., & Mercuri, E. (2001, May). Visual disorders in children with brain lesions: 1. Maturation of visual function in infants with neonatal brain lesions: Correlation with neuroimaging. *European Journal of Paediatric Neurology*. https://doi.org/10.1053/ejpn.2001.0480

Guzzetta, A., D'acunto, G., Rose, S., Tinelli, F., Boyd, R., & Cioni, G. (2010, October). Plasticity of the visual system after early brain damage. *Developmental Medicine and Child Neurology*. https://doi.org/10.1111/j.1469-8749.2010.03710.x

Haak, K. V., Cornelissen, F. W., & Morland, A. B. (2012). Population receptive field dynamics in human visual cortex. *PLoS ONE*, *7*(5), 1–8. https://doi.org/10.1371/journal.pone.0037686

Haak, K. V., Fast, E., Bao, M., Lee, M., & Engel, S. A. (2014). *Four Days of Visual Contrast Deprivation Reveals Limits of Neuronal Adaptation*. *Current Biology* (Vol. 24). https://doi.org/10.1016/j.cub.2014.09.027

Haak, K. V., Langers, D. R. M., Renken, R., van Dijk, P., Borgstein, J., & Cornelissen, F. W. (2014). Abnormal visual field maps in human cortex: A mini-review and a case report. *Cortex*, *56*, 14–25. https://doi.org/10.1016/j.cortex.2012.12.005

Haak, K. V., Morland, A. B., & Engel, S. A. (2015). Plasticity, and Its Limits, in Adult Human Primary Visual Cortex. *Multisensory Research*, *28*(3), 297–307. https://doi.org/10.1163/22134808-00002496

Haak, K. V., Morland, A. B., Rubin, G. S., & Cornelissen, F. W. (2016). Preserved retinotopic brain connectivity in macular degeneration. *Ophthalmic and Physiological Optics*, *36*(3), 335–343. https://doi.org/10.1111/opo.12279

Haak, K. V., Winawer, J., Harvey, B. M., Renken, R., Dumoulin, S. O., Wandell, B. A., & Cornelissen, F. W. (2013). Connective field modeling. *NeuroImage*, *66*, 376–384.

https://doi.org/10.1016/j.neuroimage.2012.10.037

Hadjikhani, N. K., & Tootell, R. B. H. (2000). Projection of rods and cones within human visual cortex. *Human Brain Mapping*, *9*(1), 55–63. https://doi.org/10.1002/(SICI)1097-0193(2000)9:1<55::AID-HBM6>3.0.CO;2-U

Haegerstrom-Portnoy, G., Schneck, M. E., Verdon, W. A., & Hewlett, S. E. (1996). Clinical vision characteristics of the congenital achromatopsias. II. Color vision. *Optometry and Vision Science*, *73*(7), 457–465. https://doi.org/10.1097/00006324-199607000-00002

Hallett, P. E. (2003). Spatial summation. *Vision Research*, *3*(1–2), 9–24. https://doi.org/10.1016/0042-6989(63)90063-4

Han, X., Jovicich, J., Salat, D. H., van der Kouwe, A., Quinn, B. T., Czanner, S., … Fischl, B. (2006). Reliability of MRI-derived measurements of human cerebral cortical thickness: The effects of field strength, scanner upgrade and manufacturer. *NeuroImage*, *32*(1), 180–194. https://doi.org/10.1016/j.neuroimage.2006.02.051

Hartline, H. K. (1938). THE RESPONSE OF SINGLE OPTIC NERVE FIBERS OF THE VERTEBRATE EYE TO ILLUMINATION OF THE RETINA. *American Journal of Physiology-Legacy Content*, *121*(2), 400–415. https://doi.org/10.1152/ajplegacy.1938.121.2.400

Harvey, B. M., & Dumoulin, S. O. (2011). The Relationship between Cortical Magnification Factor and Population Receptive Field Size in Human Visual Cortex: Constancies in Cortical Architecture. *Journal of Neuroscience*, *31*(38), 13604–13612. https://doi.org/10.1523/jneurosci.2572-11.2011

Hassall, M. M., Barnard, A. R., & MacLaren, R. E. (2017). Gene Therapy for Color Blindness. *The Yale Journal of Biology and Medicine*, *90*(4), 543–551. Retrieved from http://www.ncbi.nlm.nih.gov/pubmed/29259520

Hasson, U., Andric, M., Atilgan, H., & Collignon, O. (2016). Congenital blindness is associated with large-scale reorganization of anatomical networks. *NeuroImage*, *128*, 362–372. https://doi.org/10.1016/j.neuroimage.2015.12.048

Heeger, D. J., & Ress, D. (2002, February 1). What does fMRI tell us about neuronal activity? *Nature Reviews Neuroscience*. https://doi.org/10.1038/nrn730

Hensch, T. K. (2005). Critical period plasticity in local cortical circuits. *Nature Reviews. Neuroscience*, *6*(11), 877–888. https://doi.org/10.1038/nrn1787

Hernowo, A. T., Prins, D., Baseler, H. A., Plank, T., Gouws, A. D., Hooymans, J. M. M., … Cornelissen, F. W. (2014). Morphometric analyses of the visual pathways inmacular degeneration. *Cortex*, *56*, 99–110. https://doi.org/10.1016/j.cortex.2013.01.003

Hickman, S., & Morland, A. B. (2011). Assessing visual dysfunction with fMRI, *11*(3), 20–21.

Hirji, N., Aboshiha, J., Georgiou, M., Bainbridge, J. W., & Michaelides, M. (2018, March 4). Achromatopsia: clinical features, molecular genetics, animal models and therapeutic

options. *Ophthalmic Genetics*. Taylor & Francis. https://doi.org/10.1080/13816810.2017.1418389

Hirji, N., Georgiou, M., Kalitzeos, A., Bainbridge, J. W., Kumaran, N., Aboshiha, J., … Michaelides, M. (2018). Longitudinal assessment of retinal structure in achromatopsia patients with long-term follow-up. *Investigative Ophthalmology and Visual Science*, *59*(15), 5735–5744. https://doi.org/10.1167/iovs.18-25452

Hirsch, J., & Curcio, C. A. (1989). The spatial resolution capacity of human foveal retina. *Vision Research*, *29*(9), 1095–1101. https://doi.org/10.1016/0042-6989(89)90058-8

Hoffmann, M. B., & Dumoulin, S. O. (2015). Congenital visual pathway abnormalities: a window onto cortical stability and plasticity. *Trends in Neurosciences*, *38*(1), 55–65. https://doi.org/10.1016/j.tins.2014.09.005

Hoffmann, M. B., Kaule, F. R., Levin, N., Masuda, Y., Kumar, A., Gottlob, I., … Dumoulin, S. O. (2012). Plasticity and Stability of the Visual System in Human Achiasma. *Neuron*, *75*(3), 393–401. https://doi.org/10.1016/j.neuron.2012.05.026

Hoffmann, M. B., Tolhurst, D. J., Moore, A. T., & Morland, A. B. (2003). Organization of the visual cortex in human albinism. *The Journal of Neuroscience : The Official Journal of the Society for Neuroscience*, *23*(26), 8921–8930. Retrieved from http://www.ncbi.nlm.nih.gov/pubmed/14523094

Holmes, G. (1918). DISTURBANCES OF VISION BY CEREBRAL LESIONS. *British Journal of Ophthalmology*, *2*(7), 353–384. https://doi.org/10.1136/bjo.2.7.353

Hood, D. C., & Finkelstein, M. A. (1986). Sensitivity to light. In *Handbook of Perception and Human Performance (Vol. 1: Sensory Processes and Perception). John Wiley and Sons, New York.* (pp. 5.1-5.66). Retrieved from http://scholarcommons.usf.edu/psy_facpub/793

Horton, J. C., & Hoyt, W. F. (1991). The Representation of the Visual Field in Human Striate Cortex: A Revision of the Classic Holmes Map. *Archives of Ophthalmology*, *109*(6), 816–824. https://doi.org/10.1001/archopht.1991.01080060080030

Hubel, D. H., & Wiesel, T. N. (1962). Receptive fields, binocular interaction and functional architecture in the cat's visual cortex. *The Journal of Physiology*, *160*(1), 106–154. https://doi.org/10.1113/jphysiol.1962.sp006837

Hubel, David H., & Wiesel, T. N. (1965). Receptive fileds and functional architecture in two nonstriate visual areas (18 and 19) of the cat. *Journal of Neurophysiology*, *28*(2), 229–289. https://doi.org/10.1152/jn.1965.28.2.229

Hubel, David H., & Wiesel, T. N. (1970). The period of susceptibility to the physiological effects of unilateral eye closure in kittens. *The Journal of Physiology*, *206*(2), 419–436. Retrieved from http://www.ncbi.nlm.nih.gov/pubmed/5498493

Hubel, David H., Wiesel, T. N., & LeVay, S. (1977). Plasticity of ocular dominance columns in

monkey striate cortex. *Philosophical Transactions of the Royal Society of London. Series B, Biological Sciences*, *278*(961), 377–409. https://doi.org/10.1098/rstb.1977.0050

Huber, E., Webster, J. M., Brewer, A. A., MacLeod, D. I. A., Wandell, B. A., Boynton, G. M., … Fine, I. (2015). A Lack of Experience-Dependent Plasticity After More Than a Decade of Recovered Sight. *Psychological Science*, *26*(4), 393–401. https://doi.org/10.1177/0956797614563957

Hummer, A., Ritter, M., Tik, M., Ledolter, A. A., Woletz, M., Holder, G. E., … Windischberger, C. (2016). Eyetracker-based gaze correction for robust mapping of population receptive fields. *NeuroImage*, *142*, 211–224. https://doi.org/10.1016/j.neuroimage.2016.07.003

Im, K., Lee, J.-M., Lyttelton, O., Kim, S. H., Evans, A. C., & Kim, S. I. (2008). Brain Size and Cortical Structure in the Adult Human Brain. *Cerebral Cortex*, *18*(9), 2181–2191. https://doi.org/10.1093/cercor/bhm244

Jancke, D., Erlhagen, W., Schöner, G., & Dinse, H. R. (2004). Shorter latencies for motion trajectories than for flashes in population responses of cat primary visual cortex. *Journal of Physiology*, *556*(3), 971–982. https://doi.org/10.1113/jphysiol.2003.058941

Jenkinson, M., Bannister, P., Brady, M., & Smith, S. M. (2002). Improved optimization for the robust and accurate linear registration and motion correction of brain images. *NeuroImage*, *17*(2), 825–841. Retrieved from http://www.ncbi.nlm.nih.gov/pubmed/12377157

Jiang, C., Zhang, L., Zou, C., Long, X., Liu, X., Zheng, H., … Diao, Y. (2014). Diurnal microstructural variations in healthy adult brain revealed by diffusion tensor imaging. *PLoS ONE*, *9*(1), e84822. https://doi.org/10.1371/journal.pone.0084822

Jiang, J., Zhu, W., Shi, F., Liu, Y., Li, J., Qin, W., … Jiang, T. (2009). Thick Visual Cortex in the Early Blind. *Journal of Neuroscience*, *29*(7), 2205–2211. https://doi.org/10.1523/JNEUROSCI.5451-08.2009

Kaplan, E., Marcus, S., & So, Y. T. (1979). Effects of dark adaptation on spatial and temporal properties of receptive fields in cat lateral geniculate nucleus. *The Journal of Physiology*, *294*(1), 561–580. https://doi.org/10.1113/jphysiol.1979.sp012946

Kastner, S., De Weerd, P., Pinsk, M. A., Elizondo, M. I., Desimone, R., & Ungerleider, L. G. (2017). Modulation of Sensory Suppression: Implications for Receptive Field Sizes in the Human Visual Cortex. *Journal of Neurophysiology*, *86*(3), 1398–1411. https://doi.org/10.1152/jn.2001.86.3.1398

Kaule, F. R., Wolynski, B., Gottlob, I., Stadler, J., Speck, O., Kanowski, M., … Hoffmann, M. B. (2014). Impact of chiasma opticum malformations on the organization of the human ventral visual cortex. *Human Brain Mapping*, *35*(10), 5093–5105. https://doi.org/10.1002/hbm.22534

Kay, K. N., Winawer, J., Mezer, A., & Wandell, B. A. (2013). Compressive spatial summation in human visual cortex. *Journal of Neurophysiology*, *110*(2), 481–494. https://doi.org/10.1152/jn.00105.2013

Kelly, K. R., Desimone, K. D., Gallie, B. L., & Steeves, J. K. E. (2015). Increased cortical surface area and gyrification following long-term survival from early monocular enucleation. *NeuroImage: Clinical*, *7*, 297–305. https://doi.org/10.1016/j.nicl.2014.11.020

Kennard, M., & Fulton JF. (1942). Age and reorganization of central nervous system. *Journal of the Mount Sinai Hospital*, *9*, 594–606.

Khan, N. W., Wissinger, B., Kohl, S., & Sieving, P. A. (2007). CNGB3 achromatopsia with progressive loss of residual cone function and impaired rod-mediated function. *Investigative Ophthalmology and Visual Science*, *48*(8), 3864–3871. https://doi.org/10.1167/iovs.06-1521

Kingsbury, M. A., Lettman, N. A., & Finlay, B. L. (2002). Reduction of early thalamic input alters adult corticocortical connectivity. *Brain Research. Developmental Brain Research*, *138*(1), 35–43. Retrieved from http://www.ncbi.nlm.nih.gov/pubmed/12234656

Kleiner, M., Brainard, D. H., Pelli, D. G., Broussard, C., Wolf, T., & Niehorster, D. (2007). What's new in Psychtoolbox-3? A free cross-platform toolkit for psychophysiscs with Matlab and GNU/Octave. *Cognitive and Computational Psychophysics*, *36*, 1–89. https://doi.org/10.1068/v070821

Kohl, S., Baumann, B., Broghammer, M., Jägle, H., Sieving, P. A., Kellner, U., … Wissinger, B. (2000). Mutations in the CNGB3 gene encoding the beta-subunit of the cone photoreceptor cGMP-gated channel are responsible for achromatopsia (ACHM3) linked to chromosome 8q21. *Human Molecular Genetics*, *9*(14), 2107–2116. https://doi.org/10.1093/hmg/9.14.2107

Kohl, S., Coppieters, F., Meire, F., Schaich, S., Roosing, S., Brennenstuhl, C., … Wissinger, B. (2012). A nonsense mutation in PDE6H causes autosomal-recessive incomplete achromatopsia. *American Journal of Human Genetics*, *91*(3), 527–532. https://doi.org/10.1016/j.ajhg.2012.07.006

Kohl, S., Marx, T., Giddings, I., Jägle, H., Jacobson, S. G., Apfelstedt-Sylla, E., … Wissinger, B. (1998). Total colourblindness is caused by mutations in the gene encoding the α-subunit of the cone photoreceptor cGMP-gated cation channel. *Nature Genetics*, *19*(3), 257–259. https://doi.org/10.1038/935

Kohl, S., Varsanyi, B., Antunes, G. A., Baumann, B., Hoyng, C. B., Jägle, H., … Wissinger, B. (2005). CNGB3 mutations account for 50% of all cases with autosomal recessive achromatopsia. *European Journal of Human Genetics*, *13*(3), 302–308. https://doi.org/10.1038/sj.ejhg.5201269

Kohl, S., Zobor, D., Chiang, W. C., Weisschuh, N., Staller, J., Menendez, I. G., … Lin, J. H. (2015). Mutations in the unfolded protein response regulator ATF6 cause the cone dysfunction disorder achromatopsia. *Nature Genetics*, *47*(7), 757–765. https://doi.org/10.1038/ng.3319

Kolb, H., & Dekorver, L. (1991). Midget ganglion cells of the parafovea of the human retina: A Study by electron microscopy and serial section reconstructions. *Journal of Comparative Neurology*, *303*(4), 617–636. https://doi.org/10.1002/cne.903030408

Komáromy, A. M., Alexander, J. J., Rowlan, J. S., Garcia, M. M., Chiodo, V. A., Kaya, A., … Aguirre, G. D. (2010). Gene therapy rescues cone function in congenital achromatopsia. *Human Molecular Genetics*, *19*(13), 2581–2593. https://doi.org/10.1093/hmg/ddq136

Komáromy, A. M., Rowlan, J. S., Corr, A. T. P., Reinstein, S. L., Boye, S. L., Cooper, A. E., … Aguirre, G. D. (2013). Transient photoreceptor deconstruction by CNTF enhances rAAV-Mediated cone functional rescue in late stage CNGB3-achromatopsia. *Molecular Therapy*, *21*(6), 1131–1141. https://doi.org/10.1038/mt.2013.50

Kupers, R., & Ptito, M. (2011). Cross-Modal Brain Plasticity in Congenital Blindness: Lessons from the Tongue Display Unit. *I-Perception*, *2*(8), 748–748. https://doi.org/10.1068/ic748

Langlo, C. S., Patterson, E. J., Higgins, B. P., Summerfelt, P., Razeen, M. M., Erker, L. R., … Carroll, J. (2016). Residual foveal cone structure in CNGB3-associated achromatopsia. *Investigative Ophthalmology and Visual Science*, *57*(10), 3984–3995. https://doi.org/10.1167/iovs.16-19313

Lansing, E. (2002). Canine inherited retinal degenerations : update on molecular genetic research. *The Journal of Small Animal Practice*, *43*(October), 426–432. Retrieved from http://www.ncbi.nlm.nih.gov/pubmed/12400639

Larsson, J., & Heeger, D. J. (2006). Two Retinotopic Visual Areas in Human Lateral Occipital Cortex. *Journal of Neuroscience*, *26*(51), 13128–13142. https://doi.org/10.1523/jneurosci.1657-06.2006

Lazzouni, L., & Lepore, F. (2014). Compensatory plasticity: time matters. *Frontiers in Human Neuroscience*, *8*, 340. https://doi.org/10.3389/fnhum.2014.00340

Lee, B. B., Smith, V. C., Pokorny, J., & Kremers, J. (1997). Rod inputs to macaque ganglion cells. *Vision Research*, *37*(20), 2813–2828. https://doi.org/10.1016/S0042-6989(97)00108-9

Lee, H., Purohit, R., Sheth, V., McLean, R. J., Kohl, S., Leroy, B. P., … Gottlob, I. (2015). Retinal Development in Infants and Young Children with Achromatopsia. *Ophthalmology*, *122*(10), 2145–2147. https://doi.org/10.1016/j.ophtha.2015.03.033

Legge, G. E., & Chung, S. T. L. (2016). Low Vision and Plasticity: Implications for Rehabilitation. *Annual Review of Vision Science*, *2*(1), 321–343.

https://doi.org/10.1146/annurev-vision-111815-114344

Lemos, J., Pereira, D., & Castelo-Branco, M. (2016, October 20). Visual Cortex Plasticity Following Peripheral Damage To The Visual System: fMRI Evidence. *Current Neurology and Neuroscience Reports*. https://doi.org/10.1007/s11910-016-0691-0

Lennie, P., & Fairchild, M. D. (1994). Ganglion cell pathways for rod vision. *Vision Research*, *34*(4), 477–482. https://doi.org/10.1016/0042-6989(94)90161-9

Leuba, G., & Kraftsik, R. (1994). Changes in volume, surface estimate, three-dimensional shape and total number of neurons of the human primary visual cortex from midgestation until old age. *Anatomy and Embryology*, *190*(4), 351–366. https://doi.org/10.1007/BF00187293

Levin, N., Dumoulin, S. O., Winawer, J., Dougherty, R. F., & Wandell, B. A. (2010). Cortical Maps and White Matter Tracts following Long Period of Visual Deprivation and Retinal Image Restoration. *Neuron*, *65*(1), 21–31. https://doi.org/10.1016/j.neuron.2009.12.006

Li, Q., Song, M., Xu, J., Qin, W., Yu, C., & Jiang, T. (2017). Cortical thickness development of human primary visual cortex related to the age of blindness onset. *Brain Imaging and Behavior*, *11*(4), 1029–1036. https://doi.org/10.1007/s11682-016-9576-8

Li, X., Dumoulin, S. O., Mansouri, B., & Hess, R. F. (2007). The fidelity of the cortical retinotopic map in human amblyopia. *European Journal of Neuroscience*, *25*(5), 1265–1277. https://doi.org/10.1111/j.1460-9568.2007.05356.x

Lima, B., Farias, M. F., Fiorani, M., Diogo, A. C. M., Botelho, Marco Marcondes, E. P., Nascimento-Silva, S., … Gattass, R. (2005). Cortical visual areas in monkeys: location, topography, connections, columns, plasticity and cortical dynamics. *Philosophical Transactions of the Royal Society B: Biological Sciences*, *360*(1456), 709–731. https://doi.org/10.1098/rstb.2005.1629

Liu, T., Cheung, S.-H., Schuchard, R. A., Glielmi, C. B., Hu, X., He, S., & Legge, G. E. (2010). Incomplete cortical reorganization in macular degeneration. *Investigative Ophthalmology and Visual Science*, *51*(12), 6826–6834. https://doi.org/10.1167/iovs.09-4926

Logothetis, N. K., & Wandell, B. A. (2004). Interpreting the BOLD Signal. *Annual Review of Physiology*, *66*(1), 735–769. https://doi.org/10.1146/annurev.physiol.66.082602.092845

Maclaren, J., Han, Z., Vos, S. B., Fischbein, N., & Bammer, R. (2014). Reliability of brain volume measurements: A test-retest dataset. *Scientific Data*, *1*, 140037. https://doi.org/10.1038/sdata.2014.37

Maffei, L., & Fiorentini, A. (2017). Retinogeniculate convergence and analysis of contrast. *Journal of Neurophysiology*, *35*(1), 65–72. https://doi.org/10.1152/jn.1972.35.1.65

Maguire, A. M., Simonelli, F., Pierce, E. A., Pugh, E. N., Mingozzi, F., Bennicelli, J., … Bennett, J. (2008). Safety and efficacy of gene transfer for Leber's congenital amaurosis. *The New England Journal of Medicine*, *358*(21), 2240–2248. https://doi.org/10.1056/NEJMoa0802315

Maguire, J., McKibbin, M., Khan, K., Kohl, S., Ali, M., & McKeefry, D. J. (2018). CNGB3 mutations cause severe rod dysfunction. *Ophthalmic Genetics*, *39*(1), 108–114. https://doi.org/10.1080/13816810.2017.1368087

Masland, R. H. (2001, September). The fundamental plan of the retina. *Nature Neuroscience*. Nature Publishing Group. https://doi.org/10.1038/nn0901-877

Masuda, Y., Horiguchi, H., Dumoulin, S. O., Furuta, A., Miyauchi, S., Nakadomari, S., & Wandell, B. A. (2010). Task-dependent V1 responses in human retinitis pigmentosa. *Investigative Ophthalmology and Visual Science*, *51*(10), 5356–5364. https://doi.org/10.1167/iovs.09-4775

McKeefry, D. J., Gouws, A. D., Burton, M. P., & Morland, A. B. (2009, October 13). The noninvasive dissection of the human visual cortex: Using fMRI and TMS to study the organization of the visual brain. *Neuroscientist*. SAGE PublicationsSage CA: Los Angeles, CA. https://doi.org/10.1177/1073858409334424

Merabet, L. B., Battelli, L., Obretenova, S., Maguire, S., Meijer, P., & Pascual-Leone, A. (2009). Functional recruitment of visual cortex for sound encoded object identification in the blind. *NeuroReport*, *20*(2), 132–138. https://doi.org/10.1097/WNR.0b013e32832104dc

Merigan, W., Byrne, C. E., & Maunsell, J. H. R. (1991). Does primate motion perception depend on the magnocellular pathway? *The Journal of Neuroscience : The Official Journal of the Society for Neuroscience*, *11*(11), 3422–3429. Retrieved from http://www.ncbi.nlm.nih.gov/pubmed/1941091

Merigan, W., Katz, L., & Maunsell, J. H. R. (2018). The effects of parvocellular lateral geniculate lesions on the acuity and contrast sensitivity of macaque monkeys. *The Journal of Neuroscience*, *11*(4), 994–1001. https://doi.org/10.1523/jneurosci.11-04-00994.1991

Michalakis, S., Mühlfriedel, R., Tanimoto, N., Krishnamoorthy, V., Koch, S., Fischer, M. D., … Seeliger, M. W. (2010). Restoration of cone vision in the CNGA3-/- mouse model of congenital complete lack of cone photoreceptor function. *Molecular Therapy*, *18*(12), 2057–2063. https://doi.org/10.1038/mt.2010.149

Michalakis, S., Schön, C., Becirovic, E., & Biel, M. (2017, March 1). Gene therapy for achromatopsia. *Journal of Gene Medicine*. John Wiley & Sons, Ltd. https://doi.org/10.1002/jgm.2944

Miller, M. A., Leckie, R. L., Donofry, S. D., Gianaros, P. J., Erickson, K. I., Manuck, S. B., & Roecklein, K. A. (2015). Photoperiod is associated with hippocampal volume in a large

community sample. *Hippocampus*, *25*(4), 534. https://doi.org/10.1002/hipo.22390

Morland, A. B. (2015). Organization of the Central Visual Pathways Following Field Defects Arising from Congenital, Inherited, and Acquired Eye Disease. *Annual Review of Vision Science*, *1*(1), 329–350. https://doi.org/10.1146/annurev-vision-082114-035600

Morland, A. B., Baseler, H. A., Hoffmann, M. B., Sharpe, L. T., & Wandell, B. A. (2001). Abnormal retinotopic representations in human visual cortex revealed by fMRI. *Acta Psychologica*, *107*(1–3), 229–247. https://doi.org/10.1016/S0001-6918(01)00025-7

Morland, A. B., Hoffmann, M. B., Neveu, M., & Holder, G. E. (2002). Abnormal visual projection in a human albino studied with functional magnetic resonance imaging and visual evoked potentials. *Journal of Neurology Neurosurgery and Psychiatry*, *72*(4), 523–526. https://doi.org/10.1136/jnnp.72.4.523

Moskowitz, A., Hansen, R. M., Akula, J. D., Eklund, S. E., & Fulton, A. B. (2009). Rod and rod-driven function in achromatopsia and blue cone monochromatism. *Investigative Ophthalmology and Visual Science*, *50*(2), 950–958. https://doi.org/10.1167/iovs.08-2544

Muckli, L., Naumer, M. J., & Singer, W. (2009). Bilateral visual field maps in a patient with only one hemisphere. *Proceedings of the National Academy of Sciences*, *106*(31), 13034–13039. https://doi.org/10.1073/pnas.0809688106

Mühlfriedel, R., Tanimoto, N., Schön, C., Sothilingam, V., Garrido, M. G., Beck, S. C., … Michalakis, S. (2017). AAV-mediated gene supplementation therapy in achromatopsia type 2: Preclinical data on therapeutic time window and long-term effects. *Frontiers in Neuroscience*, *11*(MAY), 292. https://doi.org/10.3389/fnins.2017.00292

Muller, J. F., & Dacheux, R. F. (1997). Alpha ganglion cells of the rabbit retina lose antagonistic surround responses under dark adaptation. *Visual Neuroscience*, *14*(2), 395–401. https://doi.org/10.1017/s0952523800011512

Mustafi, D., Engel, A. H., & Palczewski, K. (2009, July). Structure of cone photoreceptors. *Progress in Retinal and Eye Research*. NIH Public Access. https://doi.org/10.1016/j.preteyeres.2009.05.003

Nakamura, K., Brown, R. A., Narayanan, S., Collins, D. L., & Arnold, D. L. (2015). Diurnal fluctuations in brain volume: Statistical analyses of MRI from large populations. *NeuroImage*, *118*, 126–132. https://doi.org/10.1016/j.neuroimage.2015.05.077

Nestares, O., & Heeger, D. J. (2000). Robust multiresolution alignment of MRI brain volumes. *Magnetic Resonance in Medicine*, *43*(5), 705–715. https://doi.org/10.1002/(SICI)1522-2594(200005)43:5<705::AID-MRM13>3.0.CO;2-R

Nickells, R. W. (2012). The First Steps in Seeing. *Archives of Ophthalmology*, *117*(4), 550. https://doi.org/10.1001/archopht.117.4.550

Noppeney, U., Friston, K. J., Ashburner, J., Frackowiak, R., & Price, C. J. (2005, July 12). Early visual deprivation induces structural plasticity in gray and white matter [1]. *Current Biology*. https://doi.org/10.1016/j.cub.2005.06.053

Nurminen, L., Kilpeläinen, M., Laurinen, P., & Vanni, S. (2009). Area Summation in Human Visual System: Psychophysics, fMRI, and Modeling. *Journal of Neurophysiology*, *102*(5), 2900–2909. https://doi.org/10.1152/jn.00201.2009

Okawa, H., & Sampath, A. P. (2007). Optimization of Single-Photon Response Transmission at the Rod-to-Rod Bipolar Synapse. *Physiology*, *22*(4), 279–286. https://doi.org/10.1152/physiol.00007.2007

Osterberg, G. (1937). Topography of the Layer of Rods and Cones in the Human Retina. *Journal of the American Medical Association*, *108*(3), 232. https://doi.org/10.1001/jama.1937.02780030070033

Pan, W. J., Wu, G., Li, C. X., Lin, F., Sun, J., & Lei, H. (2007). Progressive atrophy in the optic pathway and visual cortex of early blind Chinese adults: A voxel-based morphometry magnetic resonance imaging study. *NeuroImage*, *37*(1), 212–220. https://doi.org/10.1016/j.neuroimage.2007.05.014

Pang, J. J., Alexander, J. J., Lei, B., Deng, W., Zhang, K., Li, Q., … Hauswirth, W. W. (2010). Achromatopsia as a potential candidate for gene therapy. In *Advances in Experimental Medicine and Biology* (Vol. 664, pp. 639–646). NIH Public Access. https://doi.org/10.1007/978-1-4419-1399-9_73

Pang, J. J., Deng, W. T., Dai, X., Lei, B., Everhart, D., Umino, Y., … Hauswirth, W. W. (2012). AAV-mediated cone rescue in a naturally occurring mouse model of CNGA3-achromatopsia. *PLoS ONE*, *7*(4), e35250. https://doi.org/10.1371/journal.pone.0035250

Papanikolaou, A., Keliris, G. A., Lee, S., Logothetis, N. K., & Smirnakis, S. M. (2015). Nonlinear population receptive field changes in human area V5/MT+ of healthy subjects with simulated visual field scotomas. *NeuroImage*, *120*, 176–190. https://doi.org/10.1016/j.neuroimage.2015.06.085

Papanikolaou, A., Keliris, G. A., Papageorgiou, T. D., Shao, Y., Krapp, E., Papageorgiou, E., … Smirnakis, S. M. (2014). Population receptive field analysis of the primary visual cortex complements perimetry in patients with homonymous visual field defects. *Proceedings of the National Academy of Sciences*, *111*(16), E1656–E1665. https://doi.org/10.1073/pnas.1317074111

Park, H. J., Lee, J. D., Kim, E. Y., Park, B., Oh, M. K., Lee, S. C., & Kim, J. J. (2009). Morphological alterations in the congenital blind based on the analysis of cortical thickness and surface area. *NeuroImage*, *47*(1), 98–106. https://doi.org/10.1016/j.neuroimage.2009.03.076

Patel, U., Boucher, M., de Léséleuc, L., & Visintini, S. (2016). *Voretigene Neparvovec: An*

Emerging Gene Therapy for the Treatment of Inherited Blindness. *CADTH Issues in Emerging Health Technologies*. Retrieved from http://www.ncbi.nlm.nih.gov/pubmed/30855774

Patterson, C. A., Wissig, S. C., & Kohn, A. (2014). Adaptation Disrupts Motion Integration in the Primate Dorsal Stream. *Neuron*, *81*(3), 674–686. https://doi.org/10.1016/j.neuron.2013.11.022

Payne, B. R., & Lomber, S. G. (2002, April 29). Plasticity of the visual cortex after injury: What's different about the young brain? *Neuroscientist*. https://doi.org/10.1177/107385840200800212

Peichl, L., & Wässle, H. (1983). The structural correlate of the receptive field centre of alpha ganglion cells in the cat retina. *The Journal of Physiology*, *341*(1), 309–324. https://doi.org/10.1113/jphysiol.1983.sp014807

Pelli, D. G. (1997). The VideoToolbox software for visual psychophysics: Transforming numbers into movies. *Spatial Vision*, *10*(4), 437–442. https://doi.org/10.1163/156856897X00366

Plank, T., Frolo, J., Brandl-Rühle, S., Renner, A. B., Hufendiek, K., Helbig, H., & Greenlee, M. W. (2011). Gray matter alterations in visual cortex of patients with loss of central vision due to hereditary retinal dystrophies. *NeuroImage*, *56*(3), 1556–1565. https://doi.org/10.1016/j.neuroimage.2011.02.055

Press, W. A., Brewer, A. A., Dougherty, R. F., Wade, A. R., & Wandell, B. A. (2001). Visual areas and spatial summation in human visual cortex. *Vision Research*, *41*(10–11), 1321–1332. https://doi.org/10.1016/S0042-6989(01)00074-8

Prins, D., Hanekamp, S., & Cornelissen, F. W. (2016, March 1). Structural brain MRI studies in eye diseases: Are they clinically relevant? A review of current findings. *Acta Ophthalmologica*. John Wiley & Sons, Ltd (10.1111). https://doi.org/10.1111/aos.12825

Prins, D., Jansonius, N. M., & Cornelissen, F. W. (2017). Loss of binocular vision in monocularly blind patients causes selective degeneration of the superior lateral occipital cortices. *Investigative Ophthalmology and Visual Science*, *58*(2), 1304–1313. https://doi.org/10.1167/iovs.16-20404

Prins, D., Plank, T., Baseler, H. A., Gouws, A. D., Beer, A., Morland, A. B., … Cornelissen, F. W. (2016). Surface-Based Analyses of Anatomical Properties of the Visual Cortex in Macular Degeneration. *PLOS ONE*, *11*(1), e0146684. https://doi.org/10.1371/journal.pone.0146684

Ptito, M., Schneider, F. C. G., Paulson, O. B., & Kupers, R. (2008). Alterations of the visual pathways in congenital blindness. *Experimental Brain Research*, *187*(1), 41–49. https://doi.org/10.1007/s00221-008-1273-4

Purpura, K., Kaplan, E., & Shapley, R. M. (1988). Background light and the contrast gain of primate P and M retinal ganglion cells. *Proceedings of the National Academy of Sciences of the United States of America*, *85*(12), 4534–4537. https://doi.org/10.1073/pnas.85.12.4534

Purves, D., Augustine, G., & Fitzpatrick, D. (2001). Functional Specialization of the Rod and Cone Systems. In *Neuroscience* (p. na). Sinauer Associates. Retrieved from https://www.ncbi.nlm.nih.gov/books/NBK10850/

Qin, W., Liu, Y., Jiang, T., & Yu, C. (2013). The Development of Visual Areas Depends Differently on Visual Experience. *PLoS ONE*, *8*(1), e53784. https://doi.org/10.1371/journal.pone.0053784

Rakic, P. (1995). A small step for the cell, a giant leap for mankind: a hypothesis of neocortical expansion during evolution. *Trends in Neurosciences*, *18*(9), 383–388. https://doi.org/10.1016/0166-2236(95)93934-P

Reavis, E. A., Lee, J., Wynn, J. K., Engel, S. A., Jimenez, A. M., & Green, M. F. (2017). Cortical Thickness of Functionally Defined Visual Areas in Schizophrenia and Bipolar Disorder. *Cerebral Cortex*, *27*(5), 2984–2993. https://doi.org/10.1093/cercor/bhw151

Reeves, B. C. (2003). Night Vision: Basic, Clinical and Applied Aspects. *Neurochemistry International*, *19*(3), 383–384. https://doi.org/10.1016/0197-0186(91)90025-9

Reislev, N. L., Kupers, R., Siebner, H. R., Ptito, M., & Dyrby, T. B. (2016). Blindness alters the microstructure of the ventral but not the dorsal visual stream. *Brain Structure and Function*, *221*(6), 2891–2903. https://doi.org/10.1007/s00429-015-1078-8

Remmer, M. H., Rastogi, N., Ranka, M. P., & Ceisler, E. J. (2015, July). Achromatopsia: A review. *Current Opinion in Ophthalmology*. https://doi.org/10.1097/ICU.0000000000000189

Ricco, A. (1877). Relazione fra il minimo angolo visuale e l'intensità luminosa. *Memorie Della Regia Academia Di Scienze, Lettere Ed Arti in Modena*, *17*, 47–160. Retrieved from http://adsabs.harvard.edu/abs/1877MmSSI...6B..29R

Rieke, F., & Baylor, D. A. (1998). Single-photon detection by rod cells of the retina. *Reviews of Modern Physics*, *70*(3), 1027–1036. https://doi.org/10.1103/RevModPhys.70.1027

Ritter, M., Hummer, A., Ledolter, A. A., Holder, G. E., Windischberger, C., Schmidt-Erfurth, U. M., & Schmidt, U. M. (2019). Clinical science Correspondence between retinotopic cortical mapping and conventional functional and morphological assessment of retinal disease. *Br J Ophthalmol*, *103*, 208–215. https://doi.org/10.1136/bjophthalmol-2017-311443

Rodieck, R. W., Binmoeller, K. F., & Dineen, J. (1985). Parasol and midget ganglion cells of the human retina. *Journal of Comparative Neurology*, *233*(1), 115–132. https://doi.org/10.1002/cne.902330107

Roorda, A., & Williams, D. R. (1999). The arrangement of the three cone classes in the living human eye. *Nature*, *397*(6719), 520–522. https://doi.org/10.1038/17383

Rose, J. E., Malis, L. I., Kruger, L., & Baker, C. P. (1960). Effects of heavy, ionizing, monoenergetic particles on the cerebral cortex. II. Histological appearance of laminar lesions and growth of nerve fibers after laminar destructions. *The Journal of Comparative Neurology*, *115*, 243–255. Retrieved from http://www.ncbi.nlm.nih.gov/pubmed/13743284

Rudvin, I., Valberg, A., & Kilavik, B. E. (2000). Visual evoked potentials and magnocellular and parvocellular segregation. *Visual Neuroscience*, *17*(4), 579–590. https://doi.org/10.1017/s0952523800174085

Sadato, N., Okada, T., Honda, M., & Yonekura, Y. (2002). Critical period for cross-modal plasticity in blind humans: A functional MRI study. *NeuroImage*, *16*(2), 389–400. https://doi.org/10.1006/nimg.2002.1111

Sadato, N., Pascual-Leone, A., Grafman, J., Ibañez, V., Deiber, M. P., Dold, G., & Hallett, M. (1996). Activation of the primary visual cortex by Braille reading in blind subjects. *Nature*, *380*(6574), 526–528. https://doi.org/10.1038/380526a0

Schiller, P. H., Logothetis, N. K., & Charles, E. R. (1990). Functions of the colour-opponent and broad-band channels of the visual system. *Nature*, *343*(6253), 68–70. https://doi.org/10.1038/343068a0

Schiller, P. H., & Malpeli, J. G. (1977). The effect of striate cortex cooling on area 18 cells in the monkey. *Brain Research*, *126*(2), 366–369. https://doi.org/10.1016/0006-8993(77)90734-X

Schmid, M. C., Panagiotaropoulos, T., Augath, M. A., Logothetis, N. K., & Smirnakis, S. M. (2009). Visually driven activation in macaque areas V2 and V3 without input from the primary visual cortex. *PLoS ONE*, *4*(5), e5527. https://doi.org/10.1371/journal.pone.0005527

Schoenfeld, M. A., Noesselt, T., Poggel, D., Tempelmann, C., Hopf, J. M., Woldorff, M. G., … Hillyard, S. A. (2002). Analysis of pathways mediating preserved vision after striate cortex lesions. *Annals of Neurology*, *52*(6), 814–824. https://doi.org/10.1002/ana.10394

Scholtes, A. M. W., & Bouman, M. A. (1977). Psychophysical experiments on spatial summation at threshold level of the human peripheral retina. *Vision Research*, *17*(7), 867–873. https://doi.org/10.1016/0042-6989(77)90131-6

Schumacher, E. H., Jacko, J. A., Primo, S. A., Main, K. L., Moloney, K. P., Kinzel, E. N., & Ginn, J. (2008). Reorganization of visual processing is related to eccentric viewing in patients with macular degeneration. *Restorative Neurology and Neuroscience*, *26*(4–5), 391–402. Retrieved from http://www.ncbi.nlm.nih.gov/pubmed/18997314

Schwartz, O., Hsu, A., & Dayan, P. (2007, July). Space and time in visual context. *Nature Reviews Neuroscience*. Nature Publishing Group. https://doi.org/10.1038/nrn2155

Ségonne, F., Dale, A. M., Busa, E., Glessner, M., Salat, D. H., Hahn, H. K., & Fischl, B. (2004). A hybrid approach to the skull stripping problem in MRI. *NeuroImage*, *22*(3), 1060–1075. https://doi.org/10.1016/j.neuroimage.2004.03.032

Ségonne, F., Pacheco, J., & Fischl, B. (2007). Geometrically accurate topology-correction of cortical surfaces using nonseparating loops. *IEEE Transactions on Medical Imaging*, *26*(4), 518–529. https://doi.org/10.1109/TMI.2006.887364

Sereno, M. I., Dale, A. M., Reppas, J. B., Kwong, K. K., Belliveau, J. W., Brady, T. J., … Tootell, R. B. H. (1995). Borders of multiple visual areas in humans revealed by functional MRI. *Science*, *268*(5212), 889–893. Retrieved from http://www.ncbi.nlm.nih.gov/pubmed/7754376

Seriès, P., Stocker, A. A., & Simoncelli, E. P. (2009). Is the homunculus "aware" of sensory adaptation? *Neural Computation*, *21*(12), 3271–3304. https://doi.org/10.1162/neco.2009.09-08-869

Sharpe, L. T., & Stockman, A. (1999). Rod pathways: the importance of seeing nothing. *Trends in Neurosciences*, *22*(11), 497–504. Retrieved from http://www.ncbi.nlm.nih.gov/pubmed/10529817

Sharpe, L. T., Stockman, A., Fach, C. C., & Markstahler, U. (1993). Temporal and spatial summation in the human rod visual system. *The Journal of Physiology*, *463*(1), 325–348. https://doi.org/10.1113/jphysiol.1993.sp019597

Sherrington, C. S. (1906). Observations on the scratch-reflex in the spinal dog. *The Journal of Physiology*, *34*(1–2), 1–50. https://doi.org/10.1113/jphysiol.1906.sp001139

Shigihara, Y., & Zeki, S. (2014). Parallel processing in the brain's visual form system: an fMRI study. *Frontiers in Human Neuroscience*, *8*, 506. https://doi.org/10.3389/fnhum.2014.00506

Shipp, S., Adams, D. L., Moutoussis, K., & Zeki, S. (2009). Feature binding in the feedback layers of area V2. *Cerebral Cortex*, *19*(10), 2230–2239. https://doi.org/10.1093/cercor/bhn243

Shmuel, A., Yacoub, E., Pfeuffer, J., Van de Moortele, P. F., Adriany, G., Hu, X., & Ugurbil, K. (2002). Sustained negative BOLD, blood flow and oxygen consumption response and its coupling to the positive response in the human brain. *Neuron*, *36*(6), 1195–1210. https://doi.org/10.1016/S0896-6273(02)01061-9

Shushruth, S., Ichida, J. M., Levitt, J. B., & Angelucci, A. (2009). Comparison of Spatial Summation Properties of Neurons in Macaque V1 and V2. *Journal of Neurophysiology*, *102*(4), 2069–2083. https://doi.org/10.1152/jn.00512.2009

Silson, E. H., Aleman, T. S., Willett, A., Serrano, L. W., Pearson, D. J., Rauschecker, A. M., … Ashtari, M. (2018). Comparing clinical perimetry and population receptive field measures in patients with choroideremia. *Investigative Ophthalmology and Visual Science*, *59*(8), 3249–3258. https://doi.org/10.1167/iovs.18-23929

Silson, E. H., Reynolds, R. C., Kravitz, D. J., & Baker, C. I. (2018). Differential sampling of visual space in ventral and dorsal early visual cortex. *Journal of Neuroscience*, *38*(9), 2294–2303. https://doi.org/10.1523/JNEUROSCI.2717-17.2018

Sincich, L. C., Park, K. F., Wohlgemuth, M. J., & Horton, J. C. (2004). Bypassing V1: A direct geniculate input to area MT. *Nature Neuroscience*, *7*(10), 1123–1128. https://doi.org/10.1038/nn1318

Sled, J. G., Zijdenbos, A. P., & Evans, A. C. (1998). A nonparametric method for automatic correction of intensity nonuniformity in MRI data. *IEEE Transactions on Medical Imaging*, *17*(1), 87–97. https://doi.org/10.1109/42.668698

Smirnakis, S. M. (2016). Probing Human Visual Deficits with Functional Magnetic Resonance Imaging. *Annual Review of Vision Science*, *2*(1), 171–195. https://doi.org/10.1146/annurev-vision-111815-114535

Smirnakis, S. M., Brewer, A. A., Schmid, M. C., Tolias, A. S., Schüz, A., Augath, M., … Logothetis, N. K. (2005). Lack of long-term cortical reorganization after macaque retinal lesions. *Nature*, *435*(7040), 300–307. https://doi.org/10.1038/nature03495

Smith, A. T. (2001). Estimating Receptive Field Size from fMRI Data in Human Striate and Extrastriate Visual Cortex. *Cerebral Cortex*, *11*(12), 1182–1190. https://doi.org/10.1093/cercor/11.12.1182

Smith, M. A. (2006). Surround suppression in the early visual system. *The Journal of Neuroscience : The Official Journal of the Society for Neuroscience*, *26*(14), 3624–3625. https://doi.org/10.1523/JNEUROSCI.0236-06.2006

Smith, S. M. (2002). Fast robust automated brain extraction. *Human Brain Mapping*, *17*(3), 143–155. https://doi.org/10.1002/hbm.10062

Soares, J. G. ., Diogo, A. C. M., Fiorani, M., Souza, A. P. B., & Gattass, R. (2004). Effects of inactivation of the lateral pulvinar on response properties of second visual area cells in Cebus monkeys. *Clinical and Experimental Pharmacology and Physiology*, *31*(9), 580–590. https://doi.org/10.1111/j.1440-1681.2004.04051.x

Solomon, S. G., & Lennie, P. (2007, April). The machinery of colour vision. *Nature Reviews Neuroscience*. Nature Publishing Group. https://doi.org/10.1038/nrn2094

Somers, D. C., Dale, A. M., Seiffert, A. E., & Tootell, R. B. H. (1999). Functional MRI reveals spatially specific attentional modulation in human primary visual cortex. *Proceedings of the National Academy of Sciences of the United States of America*, *96*(4), 1663–1668.

https://doi.org/10.1073/pnas.96.4.1663

Spillmann, L. (2014). Receptive fields of visual neurons: The early years. *Perception*, *43*(11), 1145–1176. https://doi.org/10.1068/p7721

Stern, J. A., von Senden, M., & Heath, P. (2006). Space and Sight: The Perception of Space in Congenitally Blind Patients, Before and After Operation. *Journal of Health and Human Behavior*, *4*(2), 148. https://doi.org/10.2307/2948890

Stone, J. L., Barlow, W. E., Milam, A. H., Juan, E., & Milam, A. H. (1992). Morphometric Analysis of Macular Photoreceptors and Ganglion Cells in Retinas with Retinitis Pigmentosa. *Archives of Ophthalmology*, *110*(11), 1634–1639. https://doi.org/10.1001/archopht.1992.01080230134038

Stryker, M. P., & Harris, W. A. (1986). Binocular impulse blockade prevents the formation of ocular dominance columns in cat visual cortex. *The Journal of Neuroscience : The Official Journal of the Society for Neuroscience*, *6*(8), 2117–2133. Retrieved from http://www.ncbi.nlm.nih.gov/pubmed/3746403

Sundaram, V., Wilde, C., Aboshiha, J., Cowing, J., Han, C., Langlo, C. S., … Michaelides, M. (2014). Retinal structure and function in achromatopsia: Implications for gene therapy. *Ophthalmology*, *121*(1), 234–245. https://doi.org/10.1016/j.ophtha.2013.08.017

Takesian, A. E., & Hensch, T. K. (2013). Balancing plasticity/stability across brain development. In *Progress in Brain Research* (Vol. 207, pp. 3–34). https://doi.org/10.1016/B978-0-444-63327-9.00001-1

Teuber, H.-L. (2008). Recovery of function after brain injury in man. *Outcome of Severe Damage to the Central Nervous System*, (34), 159–190. https://doi.org/10.1002/9780470720165.ch10

Teuber, H.-L., Battersby, W. S., & Bender, M. B. (1960). *Visual Field Defects after Penetrating Missile Wounds of the Brain*. *Visual Field Defects after Penetrating Missile Wounds of the Brain*. Cambridge, MA and London, England: Harvard University Press. https://doi.org/10.4159/harvard.9780674593121

Thiadens, A. A. H. J., Slingerland, N. W. R., Roosing, S., van Schooneveld, M. J., van Lith-Verhoeven, J. J. C., van Moll-Ramirez, N., … Klaver, C. C. W. (2009). Genetic Etiology and Clinical Consequences of Complete and Incomplete Achromatopsia. *Ophthalmology*, *116*(10), 1984-1989.e1. https://doi.org/10.1016/j.ophtha.2009.03.053

Thiadens, A. A. H. J., Somervuo, V., van den Born, L. I., Roosing, S., van Schooneveld, M. J., Kuijpers, R. W. A. M., … Klaver, C. C. W. (2010). Progressive loss of cones in achromatopsia: An imaging study using spectral-domain optical coherence tomography. *Investigative Ophthalmology and Visual Science*, *51*(11), 5952–5957. https://doi.org/10.1167/iovs.10-5680

Thomas, C., Sadeghi, N., Nayak, A., Trefler, A., Sarlls, J., Baker, C. I., & Pierpaoli, C. (2018). Impact of time-of-day on diffusivity measures of brain tissue derived from diffusion tensor imaging. *NeuroImage*, *173*, 25–34. https://doi.org/10.1016/j.neuroimage.2018.02.026

Thomas, M. G., Kumar, A., Kohl, S., Proudlock, F. A., & Gottlob, I. (2011). High-resolution in vivo imaging in achromatopsia. *Ophthalmology*, *118*(5), 882–887. https://doi.org/10.1016/j.ophtha.2010.08.053

Thomas, M. G., McLean, R. J., Kohl, S., Sheth, V., & Gottlob, I. (2012). Early signs of longitudinal progressive cone photoreceptor degeneration in achromatopsia. *British Journal of Ophthalmology*, *96*(9), 1232–1236. https://doi.org/10.1136/bjophthalmol-2012-301737

Tootell, R. B. H., Dale, A. M., Sereno, M. I., & Malach, R. (1996). New images from human visual cortex. *Trends in Neurosciences*. https://doi.org/10.1016/S0166-2236(96)10053-9

Tootell, R. B. H., Mendola, J. D., Hadjikhani, N. K., Ledden, P. J., Liu, A. K., Reppas, J. B., … Dale, A. M. (1997). Functional analysis of V3A and related areas in human visual cortex. *The Journal of Neuroscience : The Official Journal of the Society for Neuroscience*, *17*(18), 7060–7078. https://doi.org/10.1523/JNEUROSCI.17-18-07060.1997

Trefler, A., Sadeghi, N., Thomas, A. G., Pierpaoli, C., Baker, C. I., & Thomas, C. (2016). Impact of time-of-day on brain morphometric measures derived from T1-weighted magnetic resonance imaging. *NeuroImage*, *133*, 41–52. https://doi.org/10.1016/j.neuroimage.2016.02.034

Tusa, R. J., Palmer, L. A., & Rosenquist, A. C. (1978). The retinotopic organization of area 17 (striate cortex) in the cat. *The Journal of Comparative Neurology*, *177*(2), 213–235. https://doi.org/10.1002/cne.901770204

Valvo, A. (2014). Behavior Patterns and Visual Rehabilitation After Early and Long-Lasting Blindness. *American Journal of Ophthalmology*, *65*(1), 19–24. https://doi.org/10.1016/0002-9394(68)91022-2

Van Essen, D. C., & Maunsell, J. H. R. (1983). Hierarchical organization and functional streams in the visual cortex. *Trends in Neurosciences*. https://doi.org/10.1016/0166-2236(83)90167-4

Van Essen, D. C., Newsome, W. T., & Maunsell, J. H. R. (1984). The visual field representation in striate cortex of the macaque monkey: Asymmetries, anisotropies, and individual variability. *Vision Research*, *24*(5), 429–448. https://doi.org/10.1016/0042-6989(84)90041-5

Vernon, R. J. W., Gouws, A. D., Lawrence, S. J. D., Wade, A. R., & Morland, A. B. (2016). Multivariate Patterns in the Human Object-Processing Pathway Reveal a Shift from

Retinotopic to Shape Curvature Representations in Lateral Occipital Areas, LO-1 and LO-2. *Journal of Neuroscience*, *36*(21), 5763–5774. https://doi.org/10.1523/jneurosci.3603-15.2016

Victor, J. D., Purpura, K., Katz, E., & Mao, B. (1994). Population encoding of spatial frequency, orientation, and color in macaque V1. *Journal of Neurophysiology*, *72*(5), 2151–2166. https://doi.org/10.1152/jn.1994.72.5.2151

Vijayakumar, N., Allen, N. B., Youssef, G., Dennison, M., Yücel, M., Simmons, J. G., & Whittle, S. (2016). Brain development during adolescence: A mixed-longitudinal investigation of cortical thickness, surface area, and volume. *Human Brain Mapping*, *37*(6), 2027–2038. https://doi.org/10.1002/hbm.23154

Voss, P., & Zatorre, R. J. (2012). Occipital cortical thickness predicts performance on pitch and musical tasks in blind individuals. *Cerebral Cortex*, *22*(11), 2455–2465. https://doi.org/10.1093/cercor/bhr311

Voss, P., & Zatorre, R. J. (2015). Early visual deprivation changes cortical anatomical covariance in dorsal-stream structures. *NeuroImage*, *108*, 194–202. https://doi.org/10.1016/j.neuroimage.2014.12.063

Wandell, B. A., Brewer, A. A., & Dougherty, R. F. (2005). Visual field map clusters in human cortex. *Philosophical Transactions of the Royal Society of London. Series B, Biological Sciences*, *360*(1456), 693–707. https://doi.org/10.1098/rstb.2005.1628

Wandell, B. A., Chial, S., & Backus, B. T. (2000). Visualization and measurement of the cortical surface. *Journal of Cognitive Neuroscience*, *12*(5), 739–752. https://doi.org/10.1162/089892900562561

Wandell, B. A., Dumoulin, S. O., & Brewer, A. A. (2007). Visual field maps in human cortex. *Neuron*, *56*(2), 366–383. https://doi.org/10.1016/j.neuron.2007.10.012

Wandell, B. A., & Smirnakis, S. M. (2009, December). Plasticity and stability of visual field maps in adult primary visual cortex. *Nature Reviews Neuroscience*. NIH Public Access. https://doi.org/10.1038/nrn2741

Wandell, B. A., & Winawer, J. (2011). Imaging retinotopic maps in the human brain. *Vision Research*, *51*(7), 718–737. https://doi.org/10.1016/j.visres.2010.08.004

Wandell, B. A., & Winawer, J. (2015). Computational neuroimaging and population receptive fields. *Trends in Cognitive Sciences*, *19*(6), 349–357. https://doi.org/10.1016/j.tics.2015.03.009

Wang, I., Khan, N. W., Branham, K., Wissinger, B., Kohl, S., & Heckenlively, J. R. (2012). Establishing baseline rod electroretinogram values in achromatopsia and cone dystrophy. *Documenta Ophthalmologica*, *125*(3), 229–233. https://doi.org/10.1007/s10633-012-9350-1

Wässle, H., Grünert, U., Röhrenbeck, J., & Boycott, B. B. (1990). Retinal ganglion cell density and cortical magnification factor in the primate. *Vision Research*, *30*(11), 1897–1911. https://doi.org/10.1016/0042-6989(90)90166-I

Welbourne, L. E., Morland, A. B., & Wade, A. R. (2018). Population receptive field (pRF) measurements of chromatic responses in human visual cortex using fMRI. *NeuroImage*, *167*, 84–94. https://doi.org/10.1016/j.neuroimage.2017.11.022

Werniuk, J. (1997). View from the top. *Canadian Mining Journal*, *118*(6), 11–13, 15. https://doi.org/10.1016/S0896-6273(02)01091-7

Werth, R. (2008). Cerebral blindness and plasticity of the visual system in children. A review of visual capacities in patients with occipital lesions, hemispherectomy or hydranencephaly. *Restorative Neurology and Neuroscience*, *26*(4–5), 377–389. Retrieved from http://www.ncbi.nlm.nih.gov/pubmed/18997313

Westheimer, G. (1965). Spatial interaction in the human retina during scotopic vision. *The Journal of Physiology*, *181*(4), 881–894. https://doi.org/10.1113/jphysiol.1965.sp007803

Wierenga, L. M., Langen, M., Oranje, B., & Durston, S. (2014). Unique developmental trajectories of cortical thickness and surface area. *NeuroImage*, *87*, 120–126. https://doi.org/10.1016/j.neuroimage.2013.11.010

Wiesel, T. N., & Hubel, D. H. (1966). Spatial and chromatic interactions in the lateral geniculate body of the rhesus monkey. *Journal of Neurophysiology*, *29*(6), 1115–1156. https://doi.org/10.1152/jn.1966.29.6.1115

Williams, D. R. (1986, January 1). Seeing through the photoreceptor mosaic. *Trends in Neurosciences*. Elsevier Current Trends. https://doi.org/10.1016/0166-2236(86)90058-5

Williams, M. A., Baker, C. I., Op De Beeck, H. P., Mok Shim, W., Dang, S., Triantafyllou, C., & Kanwisher, N. (2008). Feedback of visual object information to foveal retinotopic cortex. *Nature Neuroscience*, *11*(12), 1439–1445. https://doi.org/10.1038/nn.2218

Winawer, J., & Parvizi, J. (2016). Linking Electrical Stimulation of Human Primary Visual Cortex, Size of Affected Cortical Area, Neuronal Responses, and Subjective Experience. *Neuron*, *92*(6), 1213–1219. https://doi.org/10.1016/J.NEURON.2016.11.008

Winkler, A. M., Greve, D. N., Bjuland, K. J., Nichols, T. E., Sabuncu, M. R., Håberg, A. K., … Rimol, L. M. (2018). Joint Analysis of Cortical Area and Thickness as a Replacement for the Analysis of the Volume of the Cerebral Cortex. *Cerebral Cortex*, *28*(2), 738–749. https://doi.org/10.1093/cercor/bhx308

Winkler, A. M., Kochunov, P., Blangero, J., Almasy, L., Zilles, K., Fox, P. T., … Glahn, D. C. (2010). Cortical thickness or grey matter volume? The importance of selecting the phenotype for

imaging genetics studies. *NeuroImage*, *53*(3), 1135–1146. https://doi.org/10.1016/j.neuroimage.2009.12.028

Wong, A. M., & Sharpe, J. A. (1999). Representation of the visual field in the human occipital cortex: a magnetic resonance imaging and perimetric correlation. *Archives of Ophthalmology (Chicago, Ill. : 1960)*, *117*(2), 208–217. Retrieved from http://www.ncbi.nlm.nih.gov/pubmed/10037566

Wright, I. C., McGuire, P. K., Poline, J. B., Travere, J. M., Murray, R. M., Frith, C. D., … Friston, K. J. (1995). A voxel-based method for the statistical analysis of gray and white matter density applied to schizophrenia. *NeuroImage*, *2*(4), 244–252. https://doi.org/10.1006/nimg.1995.1032

Yildirim, F., Carvalho, J., & Cornelissen, F. W. (2018). A second-order orientation-contrast stimulus for population-receptive-field-based retinotopic mapping. *NeuroImage*, *164*, 183–193. https://doi.org/10.1016/j.neuroimage.2017.06.073

Yoshor, D., Bosking, W. H., Ghose, G. M., & Maunsell, J. H. R. (2007). Receptive fields in human visual cortex mapped with surface electrodes. *Cerebral Cortex*, *17*(10), 2293–2302. https://doi.org/10.1093/cercor/bhl138

Yushkevich, P. A., Piven, J., Hazlett, H. C., Smith, R. G., Ho, S., Gee, J. C., & Gerig, G. (2006). User-guided 3D active contour segmentation of anatomical structures: Significantly improved efficiency and reliability. *NeuroImage*, *31*(3), 1116–1128. https://doi.org/10.1016/j.neuroimage.2006.01.015

Zeidman, P., Silson, E. H., Schwarzkopf, D. S., Baker, C. I., & Penny, W. (2018). Bayesian population receptive field modelling. *NeuroImage*, *180*, 173–187. https://doi.org/10.1016/j.neuroimage.2017.09.008

Zeki, S. (1969). Representation of central visual fields in prestriate cortex of monkey. *Brain Research*, *14*(2), 271–291. https://doi.org/10.1016/0006-8993(69)90110-3

Zeki, S., & Shipp, S. (1989). Modular Connections between Areas V2 and V4 of Macaque Monkey Visual Cortex. *European Journal of Neuroscience*, *1*(5), 494–506. https://doi.org/10.1111/j.1460-9568.1989.tb00356.x

Zeki, S., Watson, J. D., Lueck, C. J., Friston, K. J., Kennard, C., & Frackowiak, R. S. (1991). A direct demonstration of functional specialization in human visual cortex. *The Journal of Neuroscience : The Official Journal of the Society for Neuroscience*, *11*(3), 641–649. Retrieved from http://www.jneurosci.org/content/11/3/641.short

Zelinger, L., Cideciyan, A. V., Kohl, S., Schwartz, S. B., Rosenmann, A., Eli, D., … Sharon, D. (2015). Genetics and disease expression in the CNGA3 form of achromatopsia: Steps on the path to gene therapy. *Ophthalmology*, *122*(5), 997–1007. https://doi.org/10.1016/j.ophtha.2014.11.025

Zhang, Y., Brady, M., & Smith, S. M. (2001). Segmentation of brain MR images through a hidden Markov random field model and the expectation-maximization algorithm. *IEEE Transactions on Medical Imaging*, *20*(1), 45–57. https://doi.org/10.1109/42.906424

Zuidema, P., Verschuure, H., Bouman, M. A., & Koenderink, J. J. (1981). Spatial and temporal summation in the human dark-adapted retina. *Journal of the Optical Society of America*, *71*(12), 1472–1480. Retrieved from http://www.ncbi.nlm.nih.gov/pubmed/7320780

Zuiderbaan, W., Harvey, B. M., & Dumoulin, S. O. (2012). Modeling center-surround configurations in population: Receptive fields using fMRI. *Journal of Vision*, *12*(3), 1–15. https://doi.org/10.1167/12.3.10